AN INVESTIGATION OF NEAR WAKE EFFECTS IN AIRFOIL DYNAMIC STALL

A THESIS

Presented to

The Faculty of the Division of Graduate Studies and Research

by

Roy Mac Scruggs

In Partial Fulfillment

of the Requirements for the Degree

Doctor of Philosophy

in the School of Aerospace Engineering

Georgia Institute of Technology

March 1971

AN INVESTIGATION OF NEAR WAKE

EFFECTS IN AIRFOIL DYNAMIC STALL

Approved:

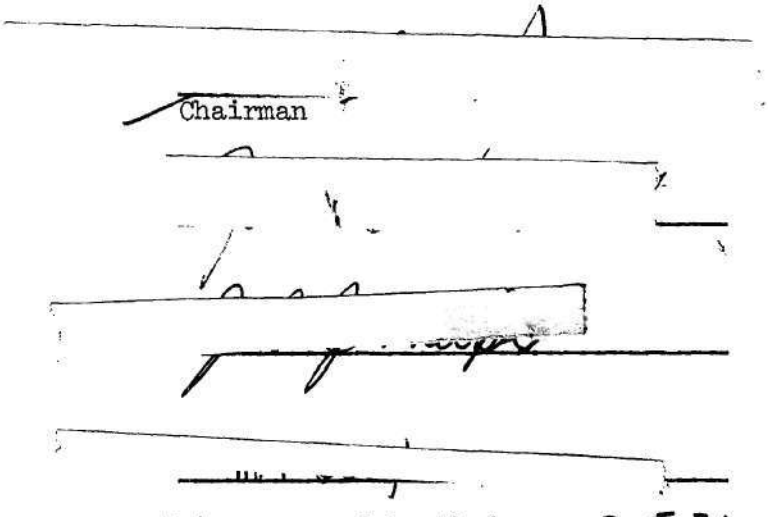

Date approved by Chairman: 8·5·71

In presenting the dissertation as a partial fulfillment of the requirements for an advanced degree from the Georgia Institute of Technology, I agree that the Library of the Institute shall make it available for inspection and circulation in accordance with its regulations governing materials of this type. I agree that permission to copy from, or to publish from, this dissertation may be granted by the professor under whose direction it was written, or, in his absence, by the Dean of the Graduate Division when such copying or publication is solely for scholarly purposes and does not involve potential financial gain. It is understood that any copying from, or publication of, this dissertation which involves potential financial gain will not be allowed without written permission.

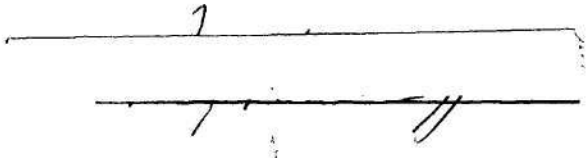

7/25/68

ACKNOWLEDGMENTS

The author is indebted to numerous persons and several organizations for the completion of this research. In particular Dr. E. R. Wood, his adviser, has been of continuing assistance throughout this investigation. His guidance and cooperation span the entire doctoral program and his encouragement was most important in bringing the program to completion. Appreciation is extended to the members of the reading committee for their liberal contribution of time and energy to a careful critique of the manuscript. The advice of Dr. G. A. Pierce has been most helpful during the formulation and solution of the analytical problem, and his critique of the manuscript proved crucial. And Dr. J. J. Cornish, III is recognized for originally directing the author toward the study of vortex flows. His advocacy of the methods of flow visualization led the author to certain fundamental experiments, the results of which form the basis for the research presented here. Special recognition goes to Dr. M. P. Stallybrass for introducing the author to the elegant function theoretic methods used in this research, as well as for the many fruitful discussions held concerning the physical and mathematical implications of the problem. The suggestions of Professor J. H. Hubbartt contributed much to the final form of the manuscript and are greatly appreciated.

Concerning the experimental phase of the research, gratitude is extended to Professor J. J. Harper, in charge of the wind tunnel, for

his advice concerning the tests and for his reading of the manuscript, to Mr. H. R. Hudson for operating the wind tunnel and for his invaluable assistance in overcoming problems encountered with the model and its installation, to Mr. H. E. Williams for many long and sometimes late hours spent in overcoming instrumentation and electronics difficulties and for his assistance in running the tests, to Mr. Charles Lord for his electronics expertise, and to Mr. John Malone, for his assistance in running the tests and conducting analog computer studies.

The financial assistance of the National Aeronautics and Space Administration, Langley Research Center, for the conduct of the tests is gratefully acknowledged. The Lockheed-Georgia Company is due much of the credit for this research, through its support of the author and the generous cooperation of its Training Department. The author especially apprciates the patience and encouragement of Mr. B. H. Little, Jr., Associate Director of Research for Aerospace Sciences, Lockheed Research Laboratory.

TABLE OF CONTENTS

		Page
ACKNOWLEDGMENTS		ii
LIST OF TABLES		iv
LIST OF ILLUSTRATIONS		v
NOMENCLATURE		x
SUMMARY		xv
Chapter		
I.	INTRODUCTION	1
	Background	
	Basis for the Investigation	
II.	ANALYTICAL INVESTIGATION	24
	A Model for Vortex Shedding	
	Analytical Results and Comparison with Measured Data	
III.	EXPERIMENTAL INVESTIGATION	66
	Experimental Arrangement and Data Handling	
	Experimental Results and Discussion Model of Discrete Wake Vortices Comparison of Vortex Model and Experimental Results	
IV.	CONCLUSIONS AND RECOMMENDATIONS	133
	Conclusions	
	Recommendations	

APPENDIX

A. BACKGROUND ON SINGULAR INTEGRAL EQUATIONS WITH A CAUCHY KERNEL 136

B. INSTRUMENTATION CALIBRATION AND DATA CONVERSION . . 153

C. ADDITIONAL TEST SPECTRAL DATA 159

D. ANALOG COMPUTER SIMULATION OF A VORTEX WAKE 175

LITERATURE CITED 180

VITA 183

LIST OF TABLES

Table		Page
1.	Computed Natural Strouhal Number from Wake Spectrum of Stationary Airfoil	92
2.	Effect of Vortex Convective Parameter on Computed Wake Characteristics	127
3.	Transducer Conversion Factors to Obtain Pressure Time History	158
4.	Analog Potentiometer Settings for Wake Pressure Time Histories	178

LIST OF ILLUSTRATIONS

Figure		Page
1.	Typical Lift and Moment Response for an Airfoil in Dynamic Stall	4
2.	Equivalent Cylinder for Stalled Flat Plate	10
3.	Flow Visualization of Dynamic Stall for a Flat Plate	17
4.	Composite Lift Coefficient Versus Angle of Attack.	21
5.	Analytical Model for Vortex Shedding	27
6.	Airfoil Steady -Distribution for Various Degrees of Stall	39
7.	Effect of Vortex Shedding Phase on Lift Hysteresis Loop	46
8.	Experimental Pressure Distribution in Oscillatory Stall	49
9.	Flat Plate Theoretical Stall	51
10.	Time Dependent Chordwise Pressure Distribution, $\alpha_o = 17.5°$, $\bar{\alpha} = 5°$, $U_v/U = .80$, $C_{l_o} = 1.25$, $\Delta C_l = .50$	54
11.	Time Dependent Chordwise Pressure Distribution, $\alpha_o = 17.5°$, $\bar{\alpha} = 5°$, $U_v/U = .50$, $C_{l_o} = 1.25$, $\Delta C_l = .50$	55
12.	Time Dependent Chordwise Pressure Distribution, $\alpha_o = 17.5°$, $\bar{\alpha} = 5°$, $U_v/U = .33$, $C_{l_o} = 1.25$, $\Delta C_l = .50$	56
13.	Effect of Vortex Propagation Velocity on C_m Hysteresis Loop, $\alpha_o = 17.5°$, $\bar{\alpha} = 5°$, $C_{l_o} = 1.25$, $\Delta C_l = .50$	60

Figure | Page

14. Effect of Vortex Shedding Phase on C_m Hysteresis, $U_v/U = .33$, $\alpha_o = 17.5^\circ$, $\bar{\alpha} = 5^\circ$, $C_{l_o} = 1.25$, $\Delta C_l = .50$ 61

15. Effect of Downstream Vortices on Airfoil Pressure Distribution 64

16. Downstream View of Experimental Arrangement in Wind Tunnel 69

17. Exterior View of Experimental Arrangement in Wind Tunnel 71

18. Data Acquisition and Monitoring System for Wind Tunnel Data 73

19. Schematic of Data Acquisition System 74

20. Power Spectra for Two Wake Positions Showing Effect of Streamwise Position 79

21. Sample Wake Pressure Time Histories, $\alpha_o = 17.5^\circ$, $U_\infty = 60$ fps, $f = 0$ cps 81

22. Sample Wake Pressure Time Histories, $\alpha_o = 17.5^\circ$, $U_\infty = 60$ fps, $f = 15.0$ cps 82

23. Sample Wake Pressure Time Histories, $\alpha_o = 17.5^\circ$, $U_\infty = 180$ fps, $f = 0$ cps 83

24. Sample Wake Pressure Time Histories, $\alpha_o = 17.5^\circ$, $U_\infty = 180$ fps, $f = 30.0$ cps 84

25. Sample Power Spectrum of Wake Pressure 87

26. Sample Power Spectrum of Wake Pressure 88

27. Sample Power Spectrum of Wake Pressure 89

28. Sample Power Spectrum of Wake Pressure 90

29. Root Mean Square Pressure Coefficient Versus Forced Strouhal Number, $\alpha_o = 15^\circ$, Transducer Number One ($\eta = 4.4$) 94

Figure | Page

30. Root Mean Square Pressure Coefficient Versus Forced Strouhal Number, $\alpha_c = 17.5^\circ$, Transducer Number One, ($\eta = 4.4$) 95

31. Root Mean Square Pressure Coefficient Versus Forced Strouhal Number, $\alpha_c = 20^\circ$, Transducer Number One, ($\eta = 4.4$) 96

32. Vortex Wake Geometry 99

33. Effect of Convective Parameter on Pressure Time Histories for Vortex Array, b/a = .30, y = 0 . . . 102

34. Pressure Time Histories Due to Vortex Array for Various Transverse Wake Positions $2\pi U_c/\Gamma = 10.$, b/a = .30 103

35. Comparison of Wake Pressure Spectra at $\eta = 2.2$ and $\eta = -2.2$, $\alpha_c = 17.5^\circ$, $U_\infty = 80$ fps, $f = 0$ cps . 106

36. Root Mean Square Pressure Coefficient Versus η, $\alpha_c = 15.^\circ$, $U_\infty = 50$ fps 108

37. Root Mean Square Pressure Coefficient Versus η, $\alpha_c = 15.^\circ$, $U_\infty = 60$ fps 109

38. Root Mean Square Pressure Coefficient Versus η, $\alpha_c = 15.^\circ$, $U_\infty = 80$ fps 110

39. Root Mean Square Pressure Coefficient Versus η, $\alpha_c = 15.^\circ$, $U_\infty = 100$ fps. 111

40. Root Mean Square Pressure Coefficient Versus η, $\alpha_c = 15.^\circ$, $U_\infty = 140$ fps 112

41. Root Mean Square Pressure Coefficient Versus η, $\alpha_c = 15.^\circ$, $U_\infty = 180$ fps 113

42. Root Mean Square Pressure Coefficient Versus η, $\alpha_c = 17.5^\circ$, $U_\infty = 50$ fps 114

43. Root Mean Square Pressure Coefficient Versus η, $\alpha_c = 17.5^\circ$, $U_\infty = 60$ fps 115

44. Root Mean Square Pressure Coefficient Versus η, $\alpha_c = 17.5^\circ$, $U_\infty = 80$ fps 116

Figure | Page

45. Root Mean Square Pressure Coefficient Versus η, $\alpha_c = 17.5^\circ$, $U_\infty = 100$ fps 117

46. Root Mean Square Pressure Coefficient Versus η, $\alpha_c = 17.5^\circ$, $U_\infty = 140$ fps 118

47. Root Mean Square Pressure Coefficient Versus η, $\alpha_c = 17.5^\circ$, $U_\infty = 180$ fps 119

48. Root Mean Square Pressure Coefficient Versus η, $\alpha_c = 20.^\circ$, $U_\infty = 60$ fps 120

49. Root Mean Square Pressure Coefficient Versus η, $\alpha_c = 20.^\circ$, $U_\infty = 80$ fps 121

50. Root Mean Square Pressure Coefficient Versus η, $\alpha_c = 20.^\circ$, $U_\infty = 100$ fps 122

51. Root Mean Square Pressure Coefficient Versus η, $\alpha_c = 20.^\circ$, $U_\infty = 140$ fps 123

52. Possible Wake Vortex Trajectories 131

53. Pressure Transducer Calibration Curves 155

54. Additional Test Power Spectra, $\alpha_c = 15.^\circ$, $U_\infty = 50$ fps 161

55. Additional Test Power Spectra, $\alpha_c = 15.^\circ$, $U_\infty = 60$ fps 162

56. Additional Test Power Spectra, $\alpha_c = 15.^\circ$, $U_\infty = 80$ fps 163

57. Additional Test Power Spectra, $\alpha_c = 15.^\circ$, $U_\infty = 100$ fps 164

58. Additional Test Power Spectra, $\alpha_c = 15.^\circ$, $U_\infty = 140$ fps 165

59. Additional Test Power Spectra, $\alpha_c = 15.^\circ$, $U_\infty = 180$ fps 166

60. Additional Test Power Spectra, $\alpha_c = 17.5^\circ$, $U_\infty = 50$ fps 167

Figure Page

61. Additional Test Power Spectra, $\alpha_0 = 17.5°$, $U_\infty = 60$ fps, 80 fps 168

62. Additional Test Power Spectra, $\alpha_0 = 17.5°$, $U_\infty = 80$ fps, 100 fps 169

63. Additional Test Power Spectra, $\alpha_0 = 17.5°$, $U_\infty = 100$ fps 170

64. Additional Test Power Spectra, $\alpha_0 = 17.5°$, $U_\infty = 140$ fps 171

65. Additional Test Power Spectra, $\alpha_0 = 20.°$, $U_\infty = 60$ fps, 80 fps 172

66. Additional Test Power Spectra, $\alpha_0 = 20.°$ $U_\infty = 100$ fps 173

67. Additional Test Power Spectra, $\alpha_0 = 20.°$, $U_\infty = 140$ fps 174

68. Schematic of Analog Simulation 179

NOMENCLATURE

A	an arbitrary real constant
A_i	a constant used to define the power contained in the i^{th} delta function spike of a power spectral density function
C_d	two-dimensional drag coefficient
C_ℓ	two-dimensional lift coefficient
$C_{\ell c}$	two-dimensional lift coefficient for the condition of steady stall
C_m	two-dimensional moment coefficient
C_n	two-dimensional normal force coefficient
ΔC_p	fluctuating pressure coefficient
ΔC_{p_a}	incremental pressure coefficient on a flat plate or airfoil
H	a step function
I	the number of vortices shed from the leading edge of a flat plate
F	a function defining body shape or a complex function
J	the number of vortices shed from the trailing edge of a flat plate

K_1, K_2, K_3, K_4	analog scaling constants
N	the total number of solution time steps in one cycle of motion of a flat plate, or the number of vortices shed from a separation point per second
R	an airfoil Reynolds number based on chordlength or the number of equal length segments into which a flat plate is divided
R_e	an equivalent cylinder Reynolds number for an airfoil or flat plate based on the projected height transverse to the direction of flow
S_i	sensitivity of the i^{th} pressure transducer
S_f	a Strouhal number for the forced oscillation of an airfoil
S_n	a Strouhal number for natural shedding of vortices behind a bluff body, without motion
U	a reference velocity
U_v	velocity of a vortex in the wake
U_∞	freestream velocity
a	streamwise distance between consecutive vortices on one side of a wake
b	transverse distance between two rows of vortices, or the semi-chordlength of an airfoil or flat plate
c	the chordlength of an airfoil or flat plate

f	frequency of oscillation in cycles per second, or denotes a function
i	a counting index for the number of vortices shed from the leading edge of a flat plate, or the imaginary number $\sqrt{-1}$
j	a counting index for the number of vortices shed from the trailing edge of a flat plate
l	indicates the time step at which a vortex is released from the trailing edge of a flat plate
m	indicates the time step at which a vortex is released from the leading edge of a flat plate
n	an index indicating the current number of solution time steps
p	pressure
n	an index for the number of a chordwise flat plate segment
t	time
u	steamwise component of fluctuating velocity
v	component of fluctuating velocity transverse to the stream
w	complex potential
x	coordinate in the downstream direction or along the chord of a flat plate
y	coordinate transverse to the stream

x^*	normalized coordinate along the chord of a flat plate
x_i^*	normalized chordwise position of i^{th} wake vortex
x_j^*	normalized chordwise position of j^{th} wake vortex
x_n^*	normalized discrete chordwise position on a flat plate
$\bar{x}$	normalized chordwise position for reference of pitching moment on a flat plate
y^*	normalized coordinate perpendicular to the chord of a flat plate
y_i^*	normalized position, transverse to the chord, of the i^{th} wake vortex
y_j^*	normalized position, transverse to the chord, of the j^{th} wake vortex
z	a complex variable
α	angle of attack
α_o	mean angle of attack
$\bar{\alpha}$	amplitude of angular oscillation
$?$	normalized transverse wake coordinate

γ_a	bound circulation distribution
Γ	circulation associated with a discrete wake vortex
Γ_o	bound circulation associated with a mean stall condition
ξ	a dummy variable defined along the x-axis
ω	frequency in radians per second
ν	coefficient of kinematic viscosity
Φ	a function of a complex variable
Φ_p	power spectral density of a fluctuating pressure
Φ_{p_o}	power spectral density of fluctuating pressure when the airfoil is held fixed
φ_{I+1}	shedding phase of the $(I+1)^{st}$ vortex relative to airfoil position
φ_{J+1}	shedding phase of the $(J+1)^{st}$ vortex relative to airfoil position
ρ	density of air

SUMMARY

A combined analytical and experimental investigation is performed to evaluate near-wake effects on airfoil loading in dynamic stall and to study the wake structure resulting from oscillatory motion of a stalled airfoil. A central objective of the work is to establish the importance of wake Strouhal resonance as it relates to the time dependent loading of the airfoil and the establishment of wake coherency.

An analytical model is developed using a flat plate approximation and based on the assumption of circulation preserving flow, after due allowance for loss of bound circulation in steady or mean stall. The model demonstrates, through abrupt release of discrete vortices from leading and trailing edges, the type of behavior observed experimentally for the time dependent loading of a dynamically stalled airfoil. It further indicates that decreasing vortex propagation velocity, with all other parameters fixed, tend to be destabilizing to the airfoil pitch motion. The phase of vortex shedding relative to the oscillatory motion is shown to be a controlling parameter in determining hysteresis response. The effect of downstream vortices is shown to produce an apparent trailing edge pressure recovery.

The experimental program is directed toward measurement of time dependent wake structure for various stall conditions and frequencies of airfoil motion. Unsteady pressure measurements are made simultaneously at five aligned positions traversing the wake. A minimal amount of

data is obtained at one chordlength downstream; most of the data is taken at three chordlengths downstream. The airfoil, a NACA 0012 section, is pitched about the midchord with a fixed oscillatory amplitude of $\pm 1.5^{\circ}$, for several mean angles above stall. The Reynolds number range of the tests is from $.312 \times 10^6$ to 1.125×10^6.

Results indicate that natural vortex shedding is present for most test conditions, although not well defined for the Reynolds number range of the tests. Strouhal numbers for natural shedding ranged from .10 to .14, based on an equivalent cylinder diameter. Oscillatory motion is found to increase root mean square pressures in the wake by as much as 80%, with the intensification occurring in a narrow frequency band around the frequency of airfoil motion, and at the first harmonic of that frequency. The intensification occurs for a wide range of frequencies; one condition correlates well with an analytical wake representation assuming Strouhal resonance.

CHAPTER I

INTRODUCTION

Background

The phenomenon of airfoil dynamic stall and the problems associated with it have been recognized to some extent since the earliest days of powered flight. Stall flutter is one of the attendant problems, although rare until relatively recent occurrences in turbo-machinery and then in helicopters. Because energy is added to the structural system during stall flutter, it must be regarded as a critical design factor wherever it may potentially occur. Fung [1] presents a good historical review of early work on stall flutter. A more common result of dynamic stall, or even static stall, is severe wing buffeting, producing in many instances structural loads far in excess of that estimated by using aerodynamic data for the steady maximum lift condition. Wing stall may also result in stabilizer buffet, in which the stabilizer interacts with the wake produced by a partially or fully stalled wing. Even for configurations of aircraft for which the horizontal stabilizer is well above the plane of the wing, there have been occurrences of structural loads on the stabilizer well in excess of those expected [2].

The earliest systematic study of stall flutter in this country began with the experimental work of Halfman et al. [3] in which wind tunnel tests of two-dimensional airfoils oscillating at different frequencies, mean angles of attack, and amplitudes, were conducted.

The development of high performance helicopters led to intensified experimental efforts in essentially full-scale, two-dimensional test conditions, at oscillatory frequencies and wind tunnel speeds about equal to those encountered in actual flight. Notable among these studies are those reported by Carta and Ham [4] and Liiva, Davenport et al [5]. References [3] and [5] were directed generally toward experimental definition of the lift and moment hysteresis characteristics of airfoils in oscillatory motion near the stall angle. Particularly wide ranges of angles, frequencies, and Mach numbers were obtained, and both pitch and translation tests were run. It is recognized that in general the stall flutter phenomenon occurs in pure or almost pure torsion [3]. For this reason most testing has been devoted to pure, forced pitching about some axis. Axes used have been variously taken at 25%, 37%, and 50% chord positions. Figure 1, taken from the most recent series of tests by Liiva et al. [5], shows a plot of lift coefficient and moment coefficient versus angle of attack for two different mean angles and oscillatory frequencies. The instantaneous values of the coefficients for different angles throughout the cycle clearly take on large excursions away from the static value. The area enclosed by these loops is a measure of work done by the airfoil on the freestream or of work done on the airfoil by the freestream. The latter of these is unstable; it is equivalent to negative damping in a mechanical system. For the moment curve, the work is simply the line integral of moment around the loop.

The hysteresis is stabilizing if the loop direction is counter-clockwise and destabilizing if it is clockwise. The general conclusion

reached in the experimental studies mentioned thus far has been that, when an airfoil is sweeping up through the static stall angle, the stall effect is delayed in time to a higher angle of attack due to an induced favorable pressure gradient on the leeward side, or upper surface, of the airfoil. This causes a delay in the forward movement of the separation point, so that lift coefficient, C_ℓ , continues to increase for some time along a linear extension of the C_ℓ versus α curve as illustrated in Figure 1. Thus an "overshoot" in lift occurs due to pitch rate. This effect has also been compared by Ericsson [6] to the quasi-static effect that would be produced by a continual increase in section camber in the pitch-up condition. Since camber will in general lead to higher statis stall angles, the connection is clear. Thus many investigators refer to the "pitch rate induced camber."

These considerations prompted Ericsson and Reding [7] to develop a semi-empirical method for predicting lift and moment overshoot in the dynamically stalled condition. Using the idea of pitch rate induced camber, coupled with a modification of the Karman-Sears [1] theory to account for lag effects, they were able to duplicate experimental results for lift and moment for pitch up and penetration of the static stall zone. However, they noted that the pitch-down behavior exhibited moment hysteresis effects that the analysis could not account for.

An earlier attempt to extend the Karman-Sears theory into the stall regime was made by M. B. T. George [8]. His approach involved a relaxation of the Kutta condition within the confines of potential flow theory, so that a trailing edge singularity was allowed. With the movement of the stagnation point away from the trailing edge, there would be

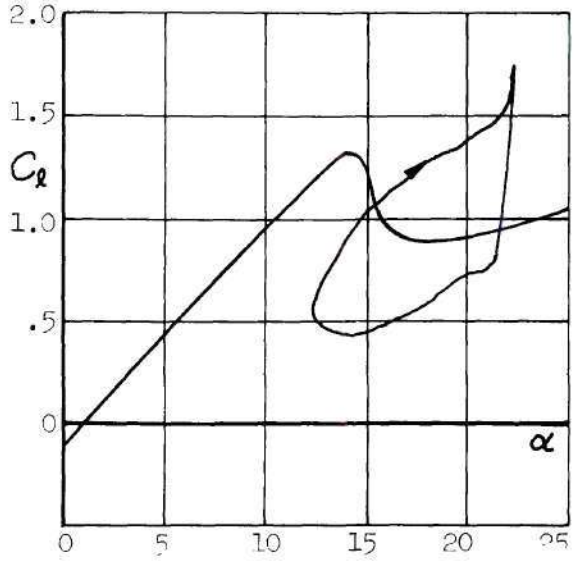

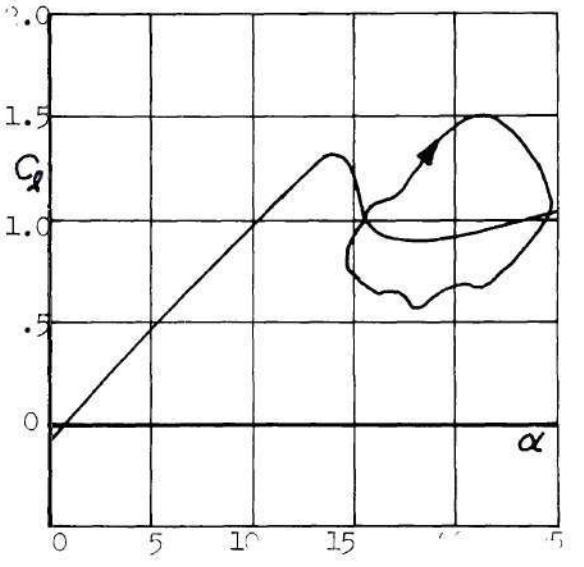

α_o = 17.5°
f = 16.37 cps
M = .2
$\bar{\alpha}$ = 4.89°

α_o = 19.78°
f = 15.11 cps
M = .2
$\bar{\alpha}$ = 4.89°

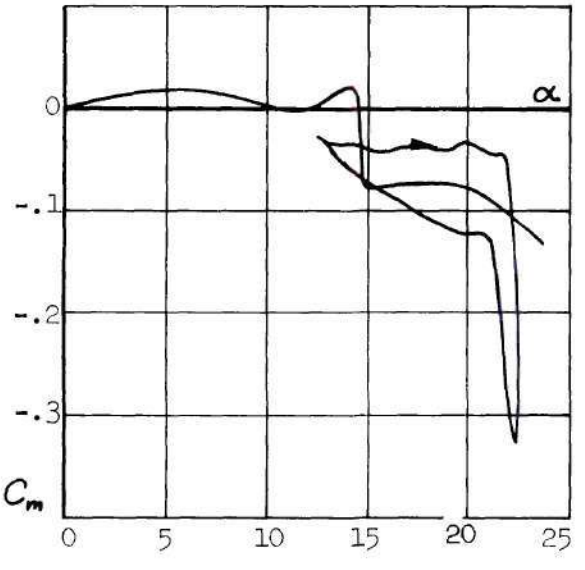

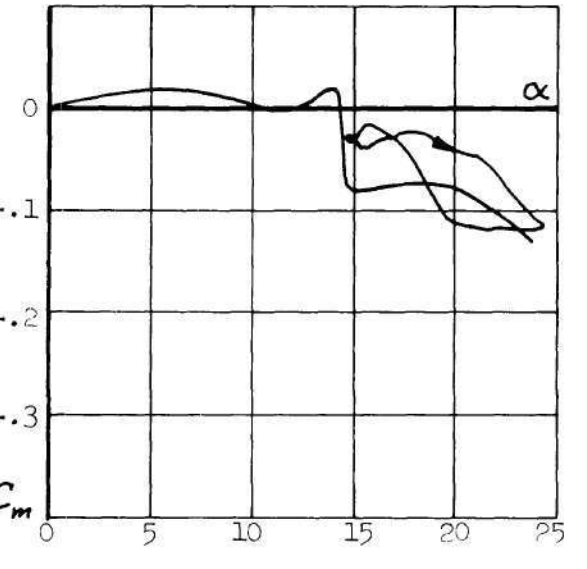

Vertol 23010-1.58

Figure 1. Typical Lift and Moment Response for an Airfoil in Dynamic Stall

a corresponding reduction in airfoil circulation. Thus the loss of lift in stall would be accounted for by a forward movement in the stagnation point.

Ham [9] recently formulated a numerical model to simulate stall in a sudden pitch-up condition. Based on experimental results obtained from the impingement of a blast wave on an airfoil at high angle of attack, Ham concluded that a discrete vortex must be shed from the airfoil leading edge following sudden pitch to a high angle of attack. This would imply that the airfoil builds to a condition of "super circulation," because of the pitch-rate effect, then suddenly releases the excess circulation as a strong, well-defined vortex developing near the leading edge. Ham was able to demonstrate such behavior with a computer program in which incremental vortices were released consecutively in small time increments from leading and trailing edge stagnation points. The collection of small vortices was shown to coalesce in a spiral pattern, similar to the development of a vorticity sheet. A major difficulty with this simulation is the time required for computation, which increases rapidly as the number of incremental vortices in the wake increases. In addition, there is the well-known problem of violent instability that occurs in a grouping of vortices after a certain time, or when the vortices are spaced too closely. The phenomenon has been attributed by Ujihara [10] to natural shear layer instability and transition to turbulence. Such an explanation may imply that the process of laminar to turbulent transition is kinematical. Various schemes have been used to prevent the incremental vortices from approaching too closely, thus avoiding numerical instability. Ham [9]

used a collapse criterion, thus when any two vortices approached each other within a certain distance, they were combined to form a new vortex. However, erratic motion and breakup may still occur. This renders a continuing solution in time numerically impossible [10]. The important result of Ham's work in relation to the present research is that he demonstrates the roll-up of a strong, discrete vortex from the airfoil leading edge, based on a model utilizing the concept of circulation and its preservation.

In the final analysis a complete understanding of the mechanism by which discrete vortices are shed from bluff bodies, in general, and stalled airfoils, in particular, must depend upon accounting for boundary layer behavior and interaction of the surrounding unsteady flow with the boundary layer. In this regard, F. K. Moore [12] has shown that unsteady boundary layer effects alone cannot account for stall hysteresis. He performed unsteady boundary layer calculations for a thin elliptic section with leading edge separation. The freestream was assumed to oscillate with small amplitude about the maximum lift condition, so that quasi-steady conservation of circulation would not have to be accounted for. Since no interaction between wake and boundary layer was assumed, Moore was able to solve numerically for the fluctuating pressure in the boundary layer and to demonstrate a lift hysteresis loop. Two important conclusions are drawn from his results: (1) the size of the hysteresis loop is of the order of the applied boundary perturbation (perturbations were made in the wind direction in the analysis), (2) the hysteresis loop is traversed in a counterclockwise direction, so that the damping remains positive.

While there are instances in which such behavior is measured experimentally, it is generally found that the hysteresis loops exhibit large excursions away from static values, and in many cases the hysteresis damping is negative. Figure 1 depicts such a situation. The exact behavior of the lift and moment curves depends critically on several parameters, the most important being speed, frequency, and angle of attack; thus it may be concluded that boundary-layer behavior taken alone is not sufficient to treat the problem.

The complex interaction of the boundary layer, separation point, and wake has not yielded to analysis at this time. But the wake structure that results from this interaction, under certain conditions, has been observed for many years. For bluff bodies, particularly cylinders, varying degrees of periodicity have been observed in the wake velocity. For low Reynolds numbers ($R < 1000$), the classical von Karman Vortex Street may be clearly observed using various flow visualization techniques. Many phenomenological studies of the vortex wakes of cylinders have been conducted over the past century. Of the early works, notable are those of Reference [13] and others summarized in Reference [14], and the stability investigation of von Karman [15]. The early investigators established that, in addition to Reynolds number, two other parameters were fundamental in characterizing vortex wakes; (1) the natural Strouhal number, defined as $S = Nd/U_\infty$, where N is the number of vortices per unit time from one side of the cylinder, d the cylinder diameter, and U_∞ the freestream speed; and (2) the stable spacing ratio, b/a , whose value von Karman found to be

.281. That is, the ratio of the lateral distance between two rows of vortices to the longitudinal spacing in one row, when the rows are staggered by one half the longitudinal distance, must take this value in order that the array move downstream in a frozen pattern. A further theoretical result of the stability theory is that the frozen pattern should move downstream with the velocity of approximately $.77\,U_\infty$. However, measurements of this velocity at positions well downstream of the body indicate an average value of about $.80\,U_\infty$ [14]. Many investigations have been devoted to determining the value of Strouhal number as a function of Reynolds number for cylinders and also other bluff bodies. Early studies were confined to low Reynolds number ($R < 1000$); later studies extended to higher Reynolds numbers [16, 17]. It was found that discrete wake periodicity began to disappear for Reynolds numbers above about 1×10^5. However, Roshko [18] recently discovered in a series of high Reynolds number tests using cylinders that strong periodicity is recovered in the range $R \geq 3.5 \times 10^6$. This range has been called the transcritical range, and Roshko found the Strouhal number to be approximately .27, as compared to .20-.21 in the critical range. The upper limit of the transcritical range is not presently known. It is clear that boundary layer behavior plays a major role in the formation of coherent vortex wakes. Whether the boundary layer is laminar or turbulent at separation, the location of the separation point, and the proximity of the region of boundary layer transition, all probably enter into the problem. The significance of Roshko's experiments was to demonstrate that at Reynolds numbers where extreme

turbulence in the separation region unquestionably exists, there appears a relatively large-scale coherence imposed on the fine-scale turbulent flow, that is, a turbulent vortex wake.

A few early investigators recognized that formation of wake vortices might not depend so much on the body causing the wake as on the wake itself. In fact, the idea of a "universal wake Strouhal number" has lately been advanced [17]. But it should also be noted that there are important distinctions to be drawn between bluff bodies with symmetric as opposed to asymmetric separation points.

Fage and Johansen [13, 20] and Tyler [21] conducted experiments on bluff bodies of different shapes to determine wake periodicity and to relate this periodicity to the degree of bluffness. In the case of a circular cylinder the bluffness was obvious, but for flat plates and airfoils the relation to resulting wake structure for a cylinder was not clear. The important assumption resulting from these investigations was that an asymmetric bluff body could be thought of as equivalent to a cylinder by projecting the body into a cylinder in the manner shown in Figure 2. Thus the natural Strouhal number, defined for a cylinder, becomes in the case of a flat plate or airfoil

$$S_n = \frac{N C \sin\alpha}{U_\infty} \tag{1}$$

where α is angle of attack and C is chordlength. The equivalent natural Strouhal number for asymmetric bluff bodies, S_n, will hereinafter be called natural Strouhal number when referring to flat plates

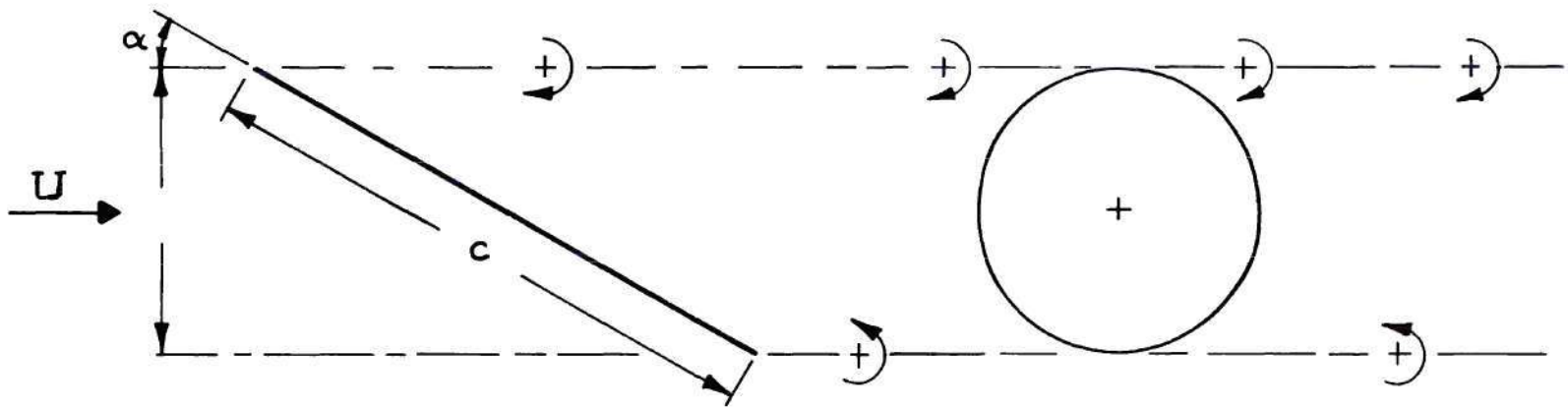

Figure 2. Equivalent Cylinder for Stalled Flat Plate

and airfoils. Krzywoblocki [22] gives an excellent survey of the work on airfoils and flat plates up to 1945. The natural Strouhal number for airfoils and plates has been measured variously between .12 and about .21, remaining relatively constant at a value of .15 for angles above 30°.

The Reynolds number in these experiments remained in the critical regime approximately 10^2 to 10^5. It is also noted that the methods employed for determining frequency content in these early experiments were rather crude. Spectral resolution to determine frequency content came into use after these experiments were conducted. Thus, variations in experimental technique and data interpretation may account for some of the scatter.

Recent experimental work has been directed toward evaluating unsteady aerodynamic effects on cylinders oscillating at frequencies near the natural Strouhal frequency. An important study has been completed by Jones [23], in which a cylinder with a diameter of three feet was tested in a wind tunnel for Mach numbers up to .60 and for Reynolds number ranging from $.36 \times 10^6$ to 18.9×10^6. The cylinder was tested in a stationary condition and then forced in a transverse oscillation at several prescribed amplitudes and frequencies. The results obtained for natural Strouhal number in the transcritical regime ($R \geq 3.5 \times 10^6$) agree well with those of Roshko for a fixed cylinder [18]. It was found for Reynolds numbers from 8.4×10^6 to 18×10^6, a range not investigated before, that Strouhal number held constant at .30. Transverse oscillation of the cylinder intensified the fluctuating lift force significantly as the frequency of vortex shedding was

approached. Also, the damping force became increasingly destabilizing as the Strouhal frequency was approached, then abruptly changed to a stable damping condition for frequencies above the Strouhal frequency. Power spectra obtained for the fluctuating lift coefficient showed that the root-mean-square lift coefficient was increased by 80 to 100% between stationary measurements and measurements taken with the cylinder oscillating at the Strouhal frequency. The percent increase in lift appeared to increase linearly with oscillatory amplitude, as this was increased to a half amplitude of six percent of cylinder diameter. Several important conclusions were apparent from this work:

(1) It confirmed Roshko's finding of the recovery of nearly periodic vortex shedding at Reynolds numbers above 3.5×10^6;

(2) It extended this range up to 18×10^6, showing that Strouhal number remains at about .30;

(3) It demonstrated negative damping due to cylinder oscillation for frequencies up to the Strouhal frequency;

(4) It demonstrated large amplification of unsteady lift for oscillation in the neighborhood of the Strouhal frequency.

The last finding implied that the near-wake structure, while recovering periodicity, also will exhibit greater intensity. That is, the alternately shed vorticies will contain greater circulation.

Although several investigators have measured chordwise pressures, lift, and moment on stalled oscillating airfoils, little experimental effort has been made to determine the wake flow structure induced by

these oscillations. A recently completed experimental investigation [24] of near-wake structure in airfoil dynamic stall has shown that large, sustained velocity fluctuations may exist several chordlengths downstream of the airfoil. The tests were carried out to measure transient wake velocity perturbations following a rapid pitch-up of the airfoil through the stall angle, then held at the maximum angle attained. Hot wire measurements showed large initial transients in both horizontal and vertical velocity, for a wide range of pitch rates, maximum angle of attack, and Reynolds numbers. It was also found that the large fluctuations were sustained for an undetermined amount of time following the airfoil motion. The record length of velocity time-history was not sufficient to determine the rate of decay of amplitude, or a complete determination of frequency content. However the time histories did show strong periodicity, and on the basis of this limited data, Strouhal number calculations were made. The values were determined to be in the neighborhood of .35 for Reynolds numbers slightly above one million. This value of Strouhal number was obtained using the chord instead of the projected chord, which would have yielded a value of 0.15. In conclusion, these experiments demonstrate that motion of the body producing the wake may bring about strong periodic fluctuations in wake velocity, even though the body motion is not periodic. In addition to the mechanics of vortex production by a bluff body or stalled airfoil, and the dynamic interaction of these vortices with the body, there is the impingement of wakes so produced on other surfaces or bodies. For example, horizontal stabilizer buffet has been a problem since the earliest days of aircraft development. Recently for a tee-

tail aircraft, severe stabilizer structural loads were obtained in deep stall [2]. This showed that even with the stabilizer located well above the normal wake location, there can still be significant interaction in the dynamically stalled condition. This implies that the vertical component of the velocity can be amplified under the proper conditions.

Several investigators have developed analytical models for predicting the response of a stabilizer to the passage of a wake. In Reference [24] a calculation of this type was carried out for a particular aircraft. This showed that predicted loads were of the same order as those measured in flight test. Similarly, an analysis was developed in Reference [25] for predicting the loading of a stabilizer due to the passage of a discrete vortex. In addition, tests were run in which a lifting surface was placed downstream of a stalled airfoil and the transient lift was measured on the downstream surface for various vertical positions relative to the stalled airfoil. Large lift transients on the simulated stabilizer were noted for a range of initial pitch rates of the airfoil through the static stall, and up to 25° final of attack.

Liepmann [26] has developed a statistical method for calculating the aerodynamic loading on an airfoil embedded in a wake, either continuously or intermittently. But this analysis assumes the wake to be random turbulence which is clearly not the case in dynamic stall. His discussion of intermittency, however, is interesting and appears to have application even for a relatively periodic wake structure.

It is clear from the preceding review that many questions remain unanswered about unsteady wakes, the mechanism of their production, and their interaction with objects in the flow. The present study is devoted to a consideration of the effect of vortices produced by an airfoil on the unsteady loading of the airfoil and further, to examine the near-wake structure resulting from airfoil oscillation above static stall.

Basis for the Investigation

In view of various experimental results obtained for airfoil dynamic stall, and considering the several analytical approaches which have been taken, it is concluded that an examination of the near-wake structure might lead to better understanding of the aerodynamic phenomena involved. The method developed by Ericsson [6,7] appears to be adequate for predicting the C_ℓ and C_m overshoot in a sudden pitch-up through static stall. But there are conditions which occur with leading edge stall, such as when the separation point moves forward to the leading edge, that cannot be accounted for by Ericsson's method. He suggests that the "anomalous C_m-loops" may be due to the sudden dumping of vorticity from the airfoil's leading edge. If this is the case, then a theory based on lag in forward movement of the separation point, such as Ericsson's, should not account for local chordwise effects of near-wake vorticity. Analytical work to date for oscillating airfoils has not been formulated for sustained leading edge separation, although considerable experimental data have been accumulated for such conditions. For example, experimental findings of Reference [24]

clearly indicate that motion of the wake-producing body can profoundly affect the time-dependent structure of the near wake. Also, the results obtained for a cylinder in Reference [23] strongly suggest that the near-wake structure is sensitive to body motion, particularly since force and damping were found to be critically dependent on Strouhal number. The wake structure associated with an airfoil oscillating in stall may therefore be important in establishing the aerodynamic response of the airfoil in either a transient condition of buffet or in the fully stalled buffet/flutter condition. Also, the problem of stabilizer buffet is highly dependent on the behavior of the near wake. Thus, a knowledge of the conditions under which wake amplification could be anticipated would serve to define conditions for stabilizer buffet due to wing stall.

Preliminary studies of wake resonance by the author relied on flow visualization in order to define the mechanics involved in developing a discrete wake. A smoke flow tunnel with an 18-inch-square test section was used to photograph the conditions shown in Figure 3. A three-inch chord flat plate was placed in the tunnel at a speed of about one foot per second. The upper photograph in Figure 3 shows the plate held statically at an angle of attack of 20°. While some periodicity is evident, particularly in the leading edge vortices, there is no well-defined vortex street as would be expected at such a Reynolds number for a cylinder ($R_e \approx 470$, an equivalent Reynolds number based on $c \sin \alpha$). The plate was driven with a small motor to provide an oscillatory angle of attack of ±3° amplitude about the mean angle. Frequency of oscillation was slowly varied until the condition shown in the lower photograph

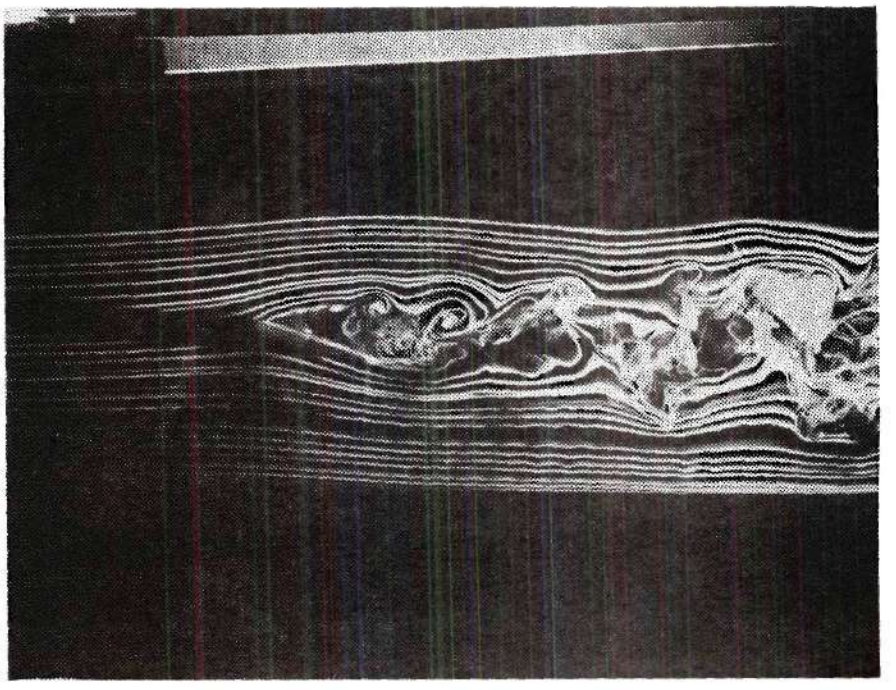

(a) STATIC $\alpha = 20^{\circ}$

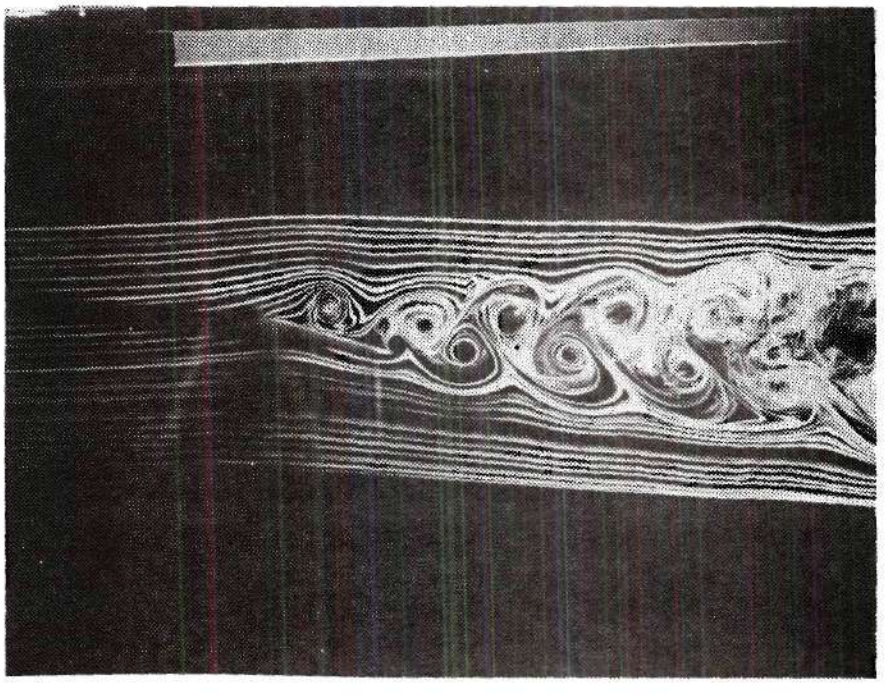

(b) DYNAMIC $f = 2.0$ c.p.s.

Figure 3. Flow Visualization of Dynamic Stall for a Flat Plate

of Figure 3 resulted at about 2.0 cps. The vortex structure clearly resembles that behind a cylinder. The spacing ratio of vortices is close to the stable ratio of about .30 as measured by previous investigators [21]. Based on an equivalent cylinder, the calculation of Strouhal number gives .15, which is close to the value measured by other investigators using hot wire measurements in the near-wake of static flat plates at comparable angles of attack [20, 21, 22]. An important observation from the smoke flow studies was that oscillations of the plate created discrete vortices for almost all frequencies, particularly from the leading edge. However, these vortices did not always develop a stable pattern in the near wake. The condition shown in Figure 3 was the most stable of the patterns observed. It is interesting to note that this pattern would persist for a wide excursion in frequency away from the optimum, once the pattern had been established.

The preceding considerations led to consideration of an an analytical model for the effect of a discrete vortex passing in the vicinity of the chord of a flat plate. In particular the effect of this vortex on the pressure distribution, lift, and moment, acting on the plate is of interest. For a flat plate in full leading edge stall, the forward separation point is fixed at the leading edge, thus avoiding the problem of determining separation point motion. In approximating a symmetrical airfoil with a flat plate for high angles of attack, the limiting condition of very large angles was examined and mean flow behavior assumed. For this purpose, a Helmholtz flow model was developed as follows [15].

The Helmholtz model for cavitating flow assumes a stagnant region on the leeward side of an obstacle and considers the mixed boundary value problem wherein the normal velocity is prescribed along the wetted surface of the body and the pressure is specified along the free streamline bounding the stagnant region, or wake. The solution of this problem for a flat plate at arbitrary angle of attack is developed in Reference [15] by the method of conformal mapping, and predicts the following normal force coefficient,

$$C_n = \frac{2\pi \sin\alpha}{4 + \pi \sin\alpha} \tag{2}$$

where it is assumed that wake pressure is equal to the static value in the undisturbed freestream. The lift and drag coefficients follow as

$$C_l = \frac{2\pi \sin\alpha \cos\alpha}{4 + \pi \sin\alpha} \tag{3}$$

$$C_d = \frac{2\pi \sin^2\alpha}{4 + \pi \sin\alpha} \tag{4}$$

Since these results were obtained originally for the condition of cavitation in a liquid, it would not be expected that direct application could be made to aerodynamic wakes. In fact, the drag coefficient is predicted to be 0.88 at 90° angle of attack, whereas experimental

measurements of drag coefficient for flat plates normal to the flow exceed this value by at least a factor of two. For Reynolds mumbers between 10^4 and 10^6, Reference [27] gives an average value for C_d of 1.98. It is well known that the mean pressure in the near wake of a stalled flat plate is much less than that in the undisturbed flow, due to viscous losses, thus the large discrepancy between the predicted and measured values of drag coefficient. Cornish and Scruggs [28] developed an approximation for flat plate lift by assuming the measured value of 1.98 for C_d , as given by Hoerner for the flat plate at 90°. Then, assuming the leeward pressure (mean wake pressure) associated with this drag to be constant along the chord, a pressure coefficient of -1.25 was obtained for the Helmholtz model. Applying this correction to to Equation (3) yielded the following lift coefficient,

$$C_l = \frac{2.25\,\pi \sin 2\alpha}{4 + \pi \sin \alpha} \tag{5}$$

Figure 4 shows this equation plotted in comparison with measured lift as given in Reference [27] for the Reynolds number between 10^4 and 10^6. The remarkable agreement between experimental data and the modified Helmholtz theory implies that the assumption of constant wake pressure must hold for angles of attack down to the stall transition range. Figure 4 also presents for comparison the curve of C_l vs. α for potential flow, as depicted by the inset sketch. It is also evident that the stall transition for the plate is completed at an angle of attack of about 16°. The transition from attached flow to Helmholtz flow extends

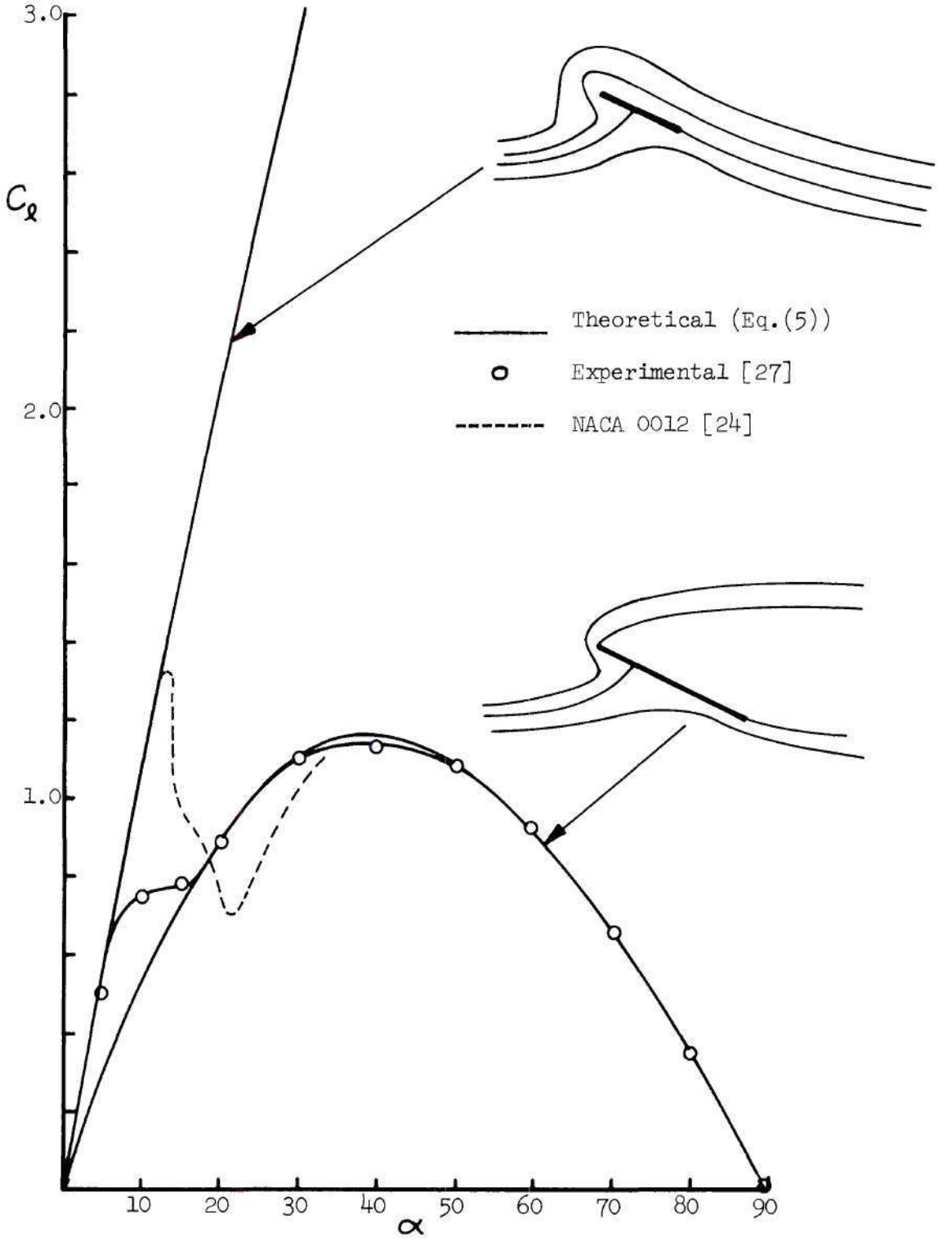

Figure 4. Composite Lift Coefficient Versus Angle of Attack

from about 7° up to 16° angle of attack, and this corresponds to a transition from trailing edge separation to leading edge separation. Fage and Johansen [20] present measurements of flat plate pressure distribution for angles of attack from 6° to 90°, indicating that above 15° the wake-side pressure is nearly constant along the chord, except very near the edges. These measurements were made at a Reynolds number of about 1.5×10^5.

The results described for a flat plate lead to the question of whether airfoils may be similarly described. This would provide a clear definition of leading edge stall. Allowing for effects of nose radius and Reynolds number, it would then be expected that symmetrical, reasonably thin airfoils would, following leading edge stall, exhibit the Helmholtz type behavior of a flat plate.

Shown superimposed on the flat plate curves of Figure 4 is the experimental lift curve for a NACA 0012 airfoil, extended into the fully stalled region [24]. Observe the same trends of C_ℓ vs. α for higher angles, but somewhat below the flat plate curve. This may be due to the wide difference in Reynolds number for the two curves.

To conclude, the experimental behavior of the wake for a flat plate at low Reynolds number showed strong wake coherency under dynamic conditions at full stall. Also, it was found that the mean or steady behavior of aerodynamic forces on an airfoil or plate could be described by means of a non-circulatory theory. However, the question remains regarding the loading response under oscillatory conditions.

The hysteresis loops shown in Figure 1, under fully stalled conditions, suggest circulatory behavior (vorticity dumping) due to

airfoil oscillation. Further, the smoke flow studies suggest that as the airfoil exhibits strong vorticity dumping, significant changes in the time-dependent structure of the wake can occur. The relation between the time dependent phenomenon of discrete vorticity dumping and the mean flow conditions about a stalled airfoil is complicated by the nonlinear nature of the complete flow field. The Helmholtz flow analysis discussed here assumes steady flow conditions which are not possible in the real flow, thus the model must be understood as a steady flow approximation of mean flow conditions.

To follow up these intitial studies, an investigation is presented here that is directed toward a better understanding of the production of hysteresis in full stall. Included in this investigation will be an experimental determination of the resulting wake structure. Theoretical consideration will be directed toward a mathematical description of the interaction of discrete, near-wake vortices and their influence on the chordwise pressure distribution on an airfoil, and resulting lift and moment. Experimental findings on wake structure will be related to airfoil behavior utilizing the principle of conservation of circulation. Thus, the central idea to be explored in this study is the extent to which circulatory potential flow may be used in describing the aerodynamic loading of fully stalled, oscillating airfoils, and its relation to the wake structure.

CHAPTER II

ANALYTICAL INVESTIGATION

In view of the similarity in static behavior of a thin symmetrical airfoil and a flat plate for angles of attack above stall, an assumption of similarity is made for the dynamically stalled condition. The flat plate model for leading edge stall fixes the upper surface separation point at the leading edge, in order that dynamic effects of separation point movement need not be considered. The forward movement of the separation point occurs during pitch-up through static stall. This has been treated by Ericsson, as discussed earlier.

While it is clear from the previous section that mean conditions prevailing in steady stall do not constitute potential flow, but instead a mixture of potential flow and wake flow, we wish to be able to account for these effects by establishing an "equivalent" potential flow model. This is a model that retains the concept of constancy of total circulation. The model will be implemented by retaining the classical thin airfoil representation of distributed bound circulation and assuming quasi-steady flow conditions. Then the Kutta-Joukowski theorem can be applied to determine the airfoil lift from the bound circulation. If at a given instant in time the airfoil circulation distribution is $\gamma_a(x)$, the corresponding pressure distribution can be computed from the Bernoulli equation as follows. Writing the equation between upper and lower surfaces,

$$P_u + \tfrac{1}{2}\rho U_u^2 = P_\ell + \tfrac{1}{2}\rho U_\ell^2 \tag{6}$$

and

$$U_u = U + u \tag{7}$$

$$U_\ell = U - u$$

where u is the induced part of the velocity near the airfoil surface and U is a freestream reference velocity. Expanding Equation (6) and taking the difference in pressure, the pressure coefficient is found to be

$$\Delta C_P = C_{P_\ell} - C_{P_u} = \frac{P_\ell - P_u}{\frac{1}{2}\rho U^2} \tag{8}$$

therefore,

$$\Delta C_p = \frac{2\rho U u}{\frac{1}{2}\rho U^2} \tag{9}$$

$$= \frac{2\gamma_a(x)}{U}$$

since γ_a is equal to the difference in tangential velocity between the surfaces. For moderate angles of attack the reference velocity can be approximated as $U = U_\infty$. For large angles of attack and improved approximation is $U = U_\infty \cos\alpha_o$, where α_o is the mean angle of attack of the airfoil. The model to be analyzed in the following section is based on conserving total circulation between the airfoil and a number of discrete vortices shed from the airfoil during a period of oscillation about a mean angle of attack. It is also desirable that the effects of steady stall be included; this will be accomplished by a movement of the rear stagnation point away from the trailing edge of the airfoil. The mechanism for accomplishing these objectives will become apparent with the mathematical solution. It is noted that the following developments implicitly assume that the Kutta-Joukowski theorem applies in determining airfoil lift, including the effects of wake vortices. However, it is not applied to the individual wake vortices, their path of motion being fixed a priori. The governing integral equation for the equivalent potential flow model will now be developed.

A Model for Vortex Shedding

Consider a flat plate at mean angle of attack α_o, where α_o may be large, relative to a freestream of velocity U. Let the coordinate x be directed along the plate as shown in Figure 5, with the origin being at midchord and the plate extending from $x = -b$ to $x = b$. The plate is assumed to perform small angular oscillations about the midchord so that the instantaneous angle of attack is

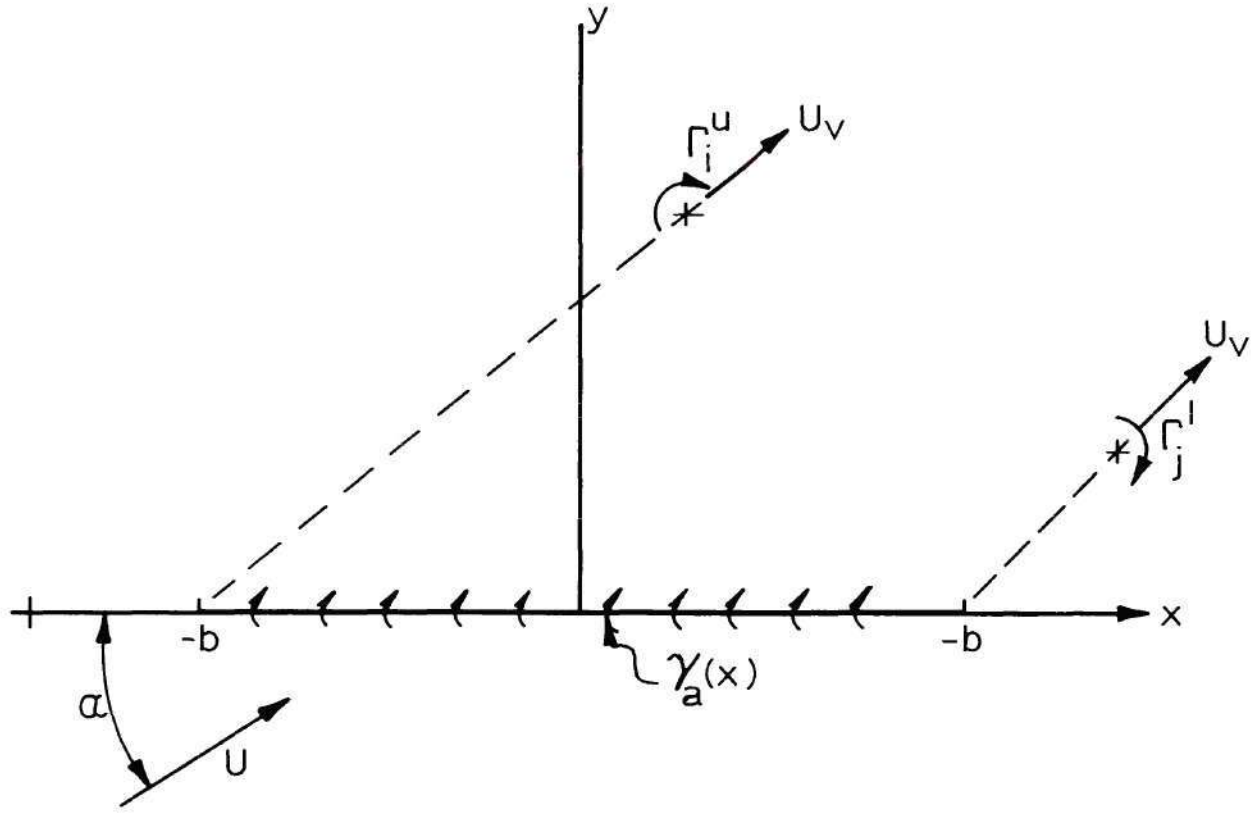

Figure 5. Analytical Model for Vortex Shedding

$$\alpha(t) = \alpha_o + \alpha'(t) \tag{10}$$

where α' is small compared to α_o. The condition that the fluid adjacent to a body in motion remain in contact with the body can be expressed as [1],

$$\frac{DF}{Dt} = 0 \tag{11}$$

where $F = F(x, y, t) = 0$ defines the boundary of the body. F may be written as

$$F = y - y_a(x, t) \tag{12}$$

where y_a is the coordinate locating points along the plate. The substantial derivative in Equation (11) may be expanded as

$$\frac{\partial F}{\partial t} + u\frac{\partial F}{\partial x} + v\frac{\partial F}{\partial y} = 0 \tag{13}$$

where u is the velocity in the x-direction and v is the velocity in the y-direction. Equations (12) and (13) give the result

$$v = \frac{\partial y_a}{\partial t} + u\frac{\partial y_a}{\partial x} \tag{14}$$

The plate displacement, $y_a(x,t)$, is given by

$$y_a(x,t) = -x\alpha'(t) \tag{15}$$

The small angle α' is taken in the oscillatory form

$$\alpha'(t) = \bar{\alpha} \sin \omega t \tag{16}$$

and terms in the boundary condition proportional to α' will be neglected. The time rate of change of angle may not be small, therefor the term

$$\frac{\partial y_a}{\partial t} = -x\dot{\alpha}'(t) \tag{17}$$

is retained in Equation (14). Thus the boundary condition is approximately

$$v(x,t) = -x\dot{\alpha}'(t) \tag{18}$$

where $v(x,t)$ is the sum of all flow velocities normal to the plate. The flow velocity, $v(x,t)$, is composed of three parts: (1) the freestream velocity component, (2) the component due to bound circulation distribution, (3) the component due to discrete wake vortices. From Figure 5, it is clear that the freestream component is

$$v_1(x,t) = U \sin \alpha_o \tag{19}$$

Due to an increment of bound circulation the contribution is

$$d v_2(x,t) = -\frac{\gamma_a(\xi,t)\, d\xi}{2\pi(x-\xi)} \tag{20}$$

where $\gamma_a(\xi,t)$ is the circulation distribution. Thus the induced velocity along the chord due to the total cound circulation is

$$v_2(x,t) = \frac{1}{2\pi}\int_{-b}^{+b} \frac{\gamma_a(\xi,t)\, d\xi}{\xi - x} \tag{21}$$

Consider a vortex located at the point (x_i, y_i), outside the line segment $y=0$, $-b \le x \le b$ Denote by Γ_i the strength of the vortex, positive clockwise as shown in Figure 5. The magnitude of the velocity induced along the line $y=0$ is

$$v_i(x,t) = \frac{\Gamma_i}{2\pi\sqrt{(x - x_i(t))^2 + y_i^2(t)}} \tag{22}$$

The component normal to the chord is accordingly,

$$v_{3i}(x,t) = \frac{\Gamma_i\,(x - x_i(t))}{2\pi\left[(x - x_i(t))^2 + y_i^2\right]} \tag{23}$$

To complete the formulation of the model, it is necessary to consider the motion of the wake vortices. In a complete unsteady representation of the wake flow field, it would be necessary to allow a continuous interaction between wake vortices and bound circulation, which would establish both the velocity and trajectory of vortex propagation. An

approximation is adopted in the present analysis which assumes both the trajectory and velocity of propagation of the vortices. The trajectory is taken to be straight line projections from the leading and trailing edges and parallel to the freestream, as shown in Figure 5. This assumption is regarded as reasonable from consideration of the Helmholtz flow model discussed in the previous section. The wake boundaries in that model are approximately parallel and from flow visualization results, as depicted in Figure 3, the wake vortices near the plate appear to move along the mean or steady boundary location. The velocity along the path, denoted by U_v, is assumed constant and equal for all vortices. The position of each wake vortex is thus established as follows: let i and j denote leading and trailing edge vortices respectively and t_i (t_j) denote the time elapsed from release of the i^{th}(j^{th}) vortex, then the vortex coordinates are

$$\left.\begin{aligned} x_i &= -b + U_v t_i \cos\alpha_o \,, \quad x_j = b + U_v t_j \cos\alpha_o \\ y_j &= U_v t_j \sin\alpha_o \,, \quad y_i = U_v t_i \sin\alpha_o \end{aligned}\right\} \tag{24}$$

For a flow configuration existing at a particular time t, the boundary condition is obtained using Equations (19), (21), and (23) in equation (18) as follows

$$\frac{1}{2\pi}\int_{-1}^{1}\frac{\gamma_a(\xi^*)\,d\xi^*}{\xi^*-x^*} = -b\,x^*\dot{\alpha}' - U\sin\alpha_0$$

$$+\frac{1}{2\pi b}\sum_{i=1}^{I}\frac{\Gamma_i\,(x^*-x_i^*)}{\left[(x^*-x_i^*)^2+y_i^{*2}\right]}+\frac{1}{2\pi b}\sum_{j=1}^{J}\frac{\Gamma_j\,(x^*-x_j^*)}{\left[(x^*-x_j^*)^2+y_j^{*2}\right]}$$

where I and J denote the total number of wake vortices on the upper and lower sides respectively and where t has been omitted for convenience. The coordinates have been normalized as follows,

$$x^* = \frac{x}{b} \qquad y^* = \frac{y}{b} \qquad \xi^* = \frac{\xi}{b} \tag{26}$$

The requirement of conservation of circulation gives

$$b\int_{-1}^{1}\gamma_a(\xi^*)\,d\xi^* + \sum_{i=1}^{I}\Gamma_i + \sum_{j=1}^{J}\Gamma_j = \Gamma_0 \tag{27}$$

where Γ_0 is a given constant. The determination of the value of Γ_0 will be discussed later.

It will be assumed that one vortex is shed from the trailing edge for each one shed from the leading edge. Then

$$\Gamma = \Gamma_i = -\Gamma_j \quad , \quad i = 1,\cdots,I \;;\; j = 1,\cdots,J \tag{28}$$

Now the relation in Equation (25) leads to the following integral equation for

$$\frac{1}{2\pi}\int_{-1}^{1}\frac{\gamma_a(\xi^*)\,d\xi^*}{\xi^*-x^*} = -b x^*\dot{\alpha}' - U\sin\alpha_0$$

$$+\frac{\Gamma}{2\pi b}\left\{\sum_{i=1}^{I}\frac{(x^*-x_i^*)}{[(x^*-x_i^*)^2+y_i^{*2}]}-\sum_{j=1}^{J}\frac{(x^*-x_j^*)}{[(x^*-x_j^*)^2+y_j^{*2}]}\right\}$$

subject to the condition

$$b\int_{-1}^{1}\gamma_a(\xi^*)\,d\xi^* = \Gamma_0 \tag{30}$$

when the number of shed vortices on each side is equal, and

$$b\int_{-1}^{1}\gamma_a(\xi^*)\,d\xi^* \pm \Gamma = \Gamma_0 \tag{31}$$

when there is an unbalance of one vortex in either the leading edge or trailing edge row. The positive sign applies in Equation (31) whenever the number of vortices in the leading edge row is one greater than the number in the trailing edge row; the negative sign applies when this unbalance is in the trailing edge row.

Before proceeding to a solution of the problem, it is necessary

to consider further the conditions represented by the model. First it is desirable that the Kutta condition be relaxed. For an equivalent potential flow model as set forth here, we then require that there is singular behavior at the trailing edge. Since the front stagnation point is not at the leading edge, singular behavior is already implied there, as in classical thin airfoil theory. Thus in the general case it is necessary to allow singularities at both edges of the plate.

Equation (29) is an integral equation for the vorticity distribution $\gamma_a(\xi)$, and its solution is required for the condition that integrable singularities be admitted at both ends of the interval on which $\gamma_a(\xi)$ is defined. A method due to Söhngen [19] has been used to solve integral equations of the type occurring here. But the method is a special one, requiring bounded behavior at one end of the interval. Carleman [36] developed a unified method of treating integral equations of the Cauchy type, using function-theoretic techniques. This method admits solutions with either bounded or singular behavior at both end points of the interval. The technique has been further developed and applied by Muskhelishvili and others [29]. The solution stated in the following is developed in Appendix A, along with a brief presentation of relevant background material.

The solution to Equation (29) possessing integrable singularities at both ends of the interval $-1 \leq \lambda^* \leq +1$ may be written as follows,

$$\gamma_a(\xi^*) = \frac{-(2x^{*2}-1)b\dot{\alpha}}{\sqrt{1-x^{*2}}} + \frac{A}{\sqrt{1-x^{*2}}} - 2U\sin\alpha_o\frac{x^*}{\sqrt{1-x^{*2}}} \qquad (32)$$

$$-\frac{2\Gamma}{\pi b\sqrt{1-x^{*2}}}\sum_{i=1}^{I}\left\{\frac{\left[(x_i^{*2}-y_i^{*2}-1)^2+4x_i^{*2}y_i^{*2}\right]^{1/4}\left[(x^*-x_i^*)\cos\frac{\theta_i}{2}-y_i^*\sin\frac{\theta_i}{2}\right]}{\left[(x^*-x_i^*)^2+y_i^{*2}\right]}\right\}$$

$$+\frac{2\Gamma}{\pi b\sqrt{1-x^{*2}}}\sum_{j=1}^{J}\left\{\frac{\left[(x_j^{*2}-y_j^{*2}-1)^2+4x_j^{*2}y_j^{*2}\right]^{1/4}\left[(x^*-x_j^*)\cos\frac{\theta_j}{2}-y_j^*\sin\frac{\theta_j}{2}\right]}{\left[(x^*-x_j^*)^2+y_j^{*2}\right]}\right\}$$

where

$$\theta_i = \tan^{-1}\frac{2x_i^*y_i^*}{x_i^{*2}-y_i^{*2}-1} \qquad (33)$$

and

$$\theta_j = \tan^{-1}\frac{2x_j^*y_j^*}{x_j^{*2}-y_j^{*2}-1} \qquad (34)$$

The arbitrary constant, A, is determined from conservation of circulation as stated in Equations (30) and (31). To establish the value of A, the expression in Equation (32) must be integrated. The method used to accomplish this is given in Appendix A. The result is stated in the following.

Equation (30), for the condition of an equal number of vortices shed from leading and trailing edge, i.e., $I = J$, gives for the constant

$$A = \frac{\Gamma_0}{\pi b} \quad , \quad I = J \tag{35}$$

If there is an unbalance of one vortex, the result is

$$A = \frac{1}{\pi b}\left[\Gamma_0 - \Gamma\right] \quad , \quad I = J + 1 \tag{36}$$

$$A = \frac{1}{\pi b}\left[\Gamma_0 + \Gamma\right] \quad , \quad J = I + 1 \tag{37}$$

The steady state part of the model ($I = J = 0$) is,

$$\gamma_{s.s.} = \frac{1}{\sqrt{1 - x^{*2}}}\left(\frac{\Gamma_0}{\pi b} - 2U \sin\alpha_0 x^*\right) \tag{38}$$

Since this theory was developed for a potential flow model, the Kutta-Joukowski theorem gives,

$$L_0 = \rho U \Gamma_0 \tag{39}$$

where L_0 is the lift existing at the stalled angle of attack α_0, and Γ_0 is the corresponding circulation. Written in terms of lift coefficient, Equation (39) gives

$$C_{\ell_0} \tfrac{1}{2} \rho U^2 (2b) = \rho U \Gamma_0 \tag{40}$$

or

$$\Gamma_0 = C_{\ell_0} U b \tag{41}$$

thus

$$\frac{\Gamma_0}{\pi b} = C_{\ell_0} \frac{U}{\pi} \tag{42}$$

Then the steady flow γ-distribution is

$$\gamma_{s.s.} = \frac{U}{\pi \sqrt{1-x^2}} \left(C_{\ell_0} - 2\pi \sin\alpha_0 \, x^2 \right) \tag{43}$$

In the sense of potential flow, the value C_{ℓ_0} corresponds to a condition in which the Kutta condition is not satisfied. When the Kutta condition is satisfied, it is a well-known result [15] that the lift coefficient is

$$C_\ell = 2\pi \sin\alpha \tag{44}$$

for all $\alpha \leq 90°$. For any lift coefficient less than that of Equation (44) the rear stagnation point will not be at the trailing edge, but must be somewhat forward of the trailing edge, the forward movement being limited by the point corresponding to zero lift. This implies

singular behavior at the trailing edge.

The unifying result represented by Equation (43) is that for any C_{ℓ_o} less than that required to satisfy the Kutta condition, there exists a singularity at the trailing edge. If C_{ℓ_o} is taken to be the value consistent with the Kutta condition, i.e.,

$$C_{\ell_1} = 2\pi \sin \alpha_o \tag{45}$$

then it is clear that Equation (43) exhibits no discontinuity at the trailing edge, and represents fully attached, i.e., non-stalled, flow. Figure 6 depicts various γ-distributions obtainable with the theory for for steady conditions.

The value of C_{ℓ_o} for any angle of attack is taken as the experimental value from the C_ℓ versus α curve for the angle of attack in question. Thus, the difference in C_ℓ between the curve for potential flow and the measured data indicates the extent of forward movement of the rear stagnation point and the strength of the trailing edge singularity. This is depicted in Figure 6(a).

The idea of relaxing the Kutta condition to approximate stall was first set forth in Reference (8), in order to modify the classical unsteady aerodynamics of von Karman and Sears to account for the effects observed in stall flutter. A difficulty was encountered in attempting to fix the forward movement of the trailing edge stagnation point. A time lag parameter was applied in such a way as to fix the airfoil circulation. But the angle-of-attack range over which the

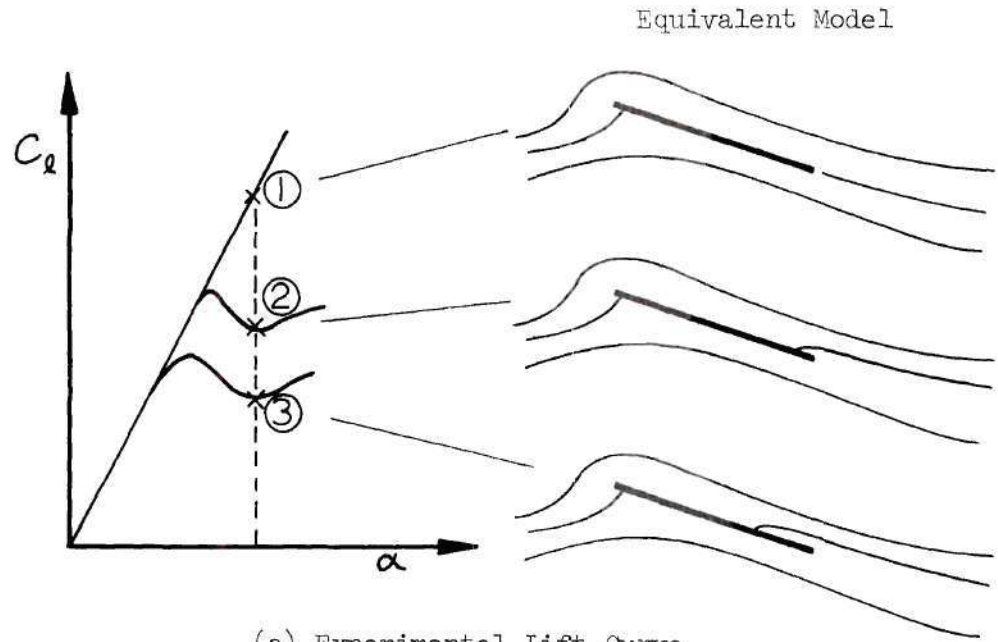

(a) Experimental Lift Curve

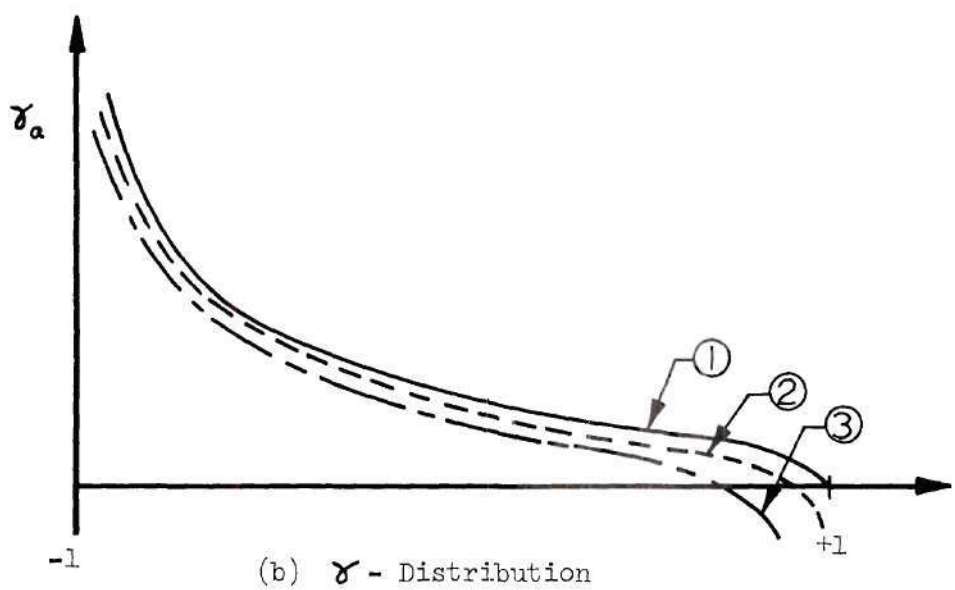

(b) γ - Distribution

Figure 6. Airfoil Steady γ-distribution for Various Degrees of Stall

time lag parameter could be used was found to be very limited. The approach taken in the present study is to permit the experimental data to fix circulation. This result is not limited by angle of attack. Further, the result reduces to that of the non-stalled condition for any angle of attack as a natural consequence of the mathematical solution.

The solution represented by Equation (32) was obtained from a mathematical formulation in which all quantities were regarded as fixed in the plane. That is, a configuration of the system of vortices was examined for a fixed instant. Physically the system is understood to be changing continuously in time. A time dependent representation, in the quasi-steady sense, can be obtained from the solution by considering a sequence of configurations corresponding to those existing after increasing time increments following an initial configuration. In order to accommodate the shedding of discrete vortices from the plate, the assumption is made that the time required for roll-up and release of a finite vortex is small compared with respect to the period of oscillation of the plate. The limiting condition of instantaneous release of a vortex is employed to simplify the numerical computations.

In regard to the above, the solution is discretized as follows. Consider one cycle of motion of the airfoil, during which one vortex is released from the leading and trailing edges. The computing time increment is $2\pi/N\omega$ where N is the number of time steps per cycle and ω is the frequency of oscillation. Let n denote the time index, so that, starting from a zero reference, time is measured by

$$t(n) = n \frac{2\pi}{N\omega} \quad , \quad n = 1, \cdots, N \tag{46}$$

Let m denote that value of n at which a vortex is released from the leading edge, and ℓ denote that value of n at which a vortex is released from the trailing edge. To represent the effect of previously shed vortices in the near wake, a time of release is computed as follows,

$$\Delta t_i(n) = \left[(I - i + 1) \frac{2\pi}{\omega} + (n - m) \frac{2\pi}{N\omega} \right], \; i = 1, \cdots, I \tag{47}$$

where I denotes the number of vortices shed from the leading edge, and

$$\Delta t_j(n) = \left[(J - j + 1) \frac{2\pi}{\omega} + (n - \ell) \frac{2\pi}{N\omega} \right], \; j = 1, \cdots, J \tag{48}$$

J denoting the number of vortices shed from the trailing edge. For the current cycle the release times for the leading edge and trailing edge vortices are respectively

$$\Delta t_{I+1}(n) = (n - m) H(n - m) \frac{2\pi}{N\omega} \tag{49}$$

$$\Delta t_{J+1}(n) = (n - \ell) H(n - \ell) \frac{2\pi}{N\omega} \tag{50}$$

where

$$H(n) = 1 \ , \ n > 0$$
$$= 0 \ , \ n \leq 0 \tag{51}$$

The positions of the wake vortices are then,

$$\left.\begin{aligned} x_i^*(n) &= -1 + \left(\frac{U_v}{U}\right) \frac{\omega \Delta t_i(n)}{k} \cos\alpha_0 \\ y_i^*(n) &= \left(\frac{U_v}{U}\right) \frac{\omega \Delta t_i(n)}{k} \sin\alpha_0 \end{aligned}\right\} \ i = 1, \cdots, I+1 \tag{52}$$

$$\left.\begin{aligned} x_j^*(n) &= 1 + \left(\frac{U_v}{U}\right) \frac{\omega \Delta t_j(n)}{k} \cos\alpha_0 \\ y_j^*(n) &= \left(\frac{U_v}{U}\right) \frac{\omega \Delta t_j(n)}{k} \sin\alpha_0 \end{aligned}\right\} \ j = 1, \cdots, J+1 \tag{53}$$

for $n = 1, \ldots, N$, and $k = b\omega/U$. The angle of attack is

$$\alpha = \alpha_0 + \bar{\alpha} \sin\left(2\pi \frac{n}{N}\right) \tag{54}$$

For convenience in numerical computation, the chordwise position x^* is evaluated at discrete points between $x^* = -1$ and $x^* = +1$, excluding the end points. Call these values x_r^*, then

$$x_r^* = -1 + r \, \Delta x^* \ , \quad r = 1, \cdots, R-1 \tag{55}$$

and

$$\Delta x^* = \frac{2}{R} \tag{56}$$

where R denotes the number of intervals of width Δx^* between $x^* = -1$ and $x^* = +1$. Utilizing the result in Equation (32), the γ-distribution may be converted to airfoil pressure coefficient as follows,

$$\Delta C_{Pa}(x_n^*) = \frac{2}{\pi\sqrt{1-x_n^{*2}}}\Bigg\{ -\pi(2x_n^{*2}-1)k\bar{\alpha}\cos\left(2\pi\frac{n}{N}\right) \tag{57}$$

$$+ \frac{\pi}{U}A(n) - 2\pi\sin\alpha_0 x_n^* + 2\Delta C_\ell \Bigg[$$

$$-\sum_{i=1}^{I}\frac{\left[(x_i^{*2}-y_i^{*2}-1)^2+4x_i^{*2}y_i^{*2}\right]^{1/4}\left[(x_n^*-x_i^*)\cos\frac{\theta_i}{2}-y_i^*\sin\frac{\theta_i}{2}\right]}{\left[(x_n^*-x_i^*)^2+y_i^{*2}\right]}$$

$$+\sum_{j=1}^{J}\frac{\left[(x_j^{*2}-y_j^{*2}-1)^2+4x_j^{*2}y_j^{*2}\right]^{1/4}\left[(x_n^*-x_j^*)\cos\frac{\theta_j}{2}-y_j^*\sin\frac{\theta_j}{2}\right]}{\left[(x_n^*-x_j^*)^2+y_j^{*2}\right]}$$

$$-H(n-m)\frac{\left[(x_{I+1}^{*2}-y_{I+1}^{*2}-1)^2+4x_{I+1}^{*2}y_{I+1}^{*2}\right]^{1/4}\left[(x_n^*-x_{I+1}^*)\cos\frac{\theta_{I+1}}{2}-y_{I+1}^*\sin\frac{\theta_{I+1}}{2}\right]}{\left[(x_n^*-x_{I+1}^*)^2+y_{I+1}^{*2}\right]}$$

$$+H(n-\ell)\frac{\left[(x_{J+1}^{*2}-y_{J+1}^{*2}-1)^2+4x_{J+1}^{*2}y_{J+1}^{*2}\right]^{1/4}\left[(x_n^*-x_{J+1}^*)\cos\frac{\theta_{J+1}}{2}-y_{J+1}^*\sin\frac{\theta_{J+1}}{2}\right]}{\left[(x_n^*-x_{J+1}^*)^2+y_{J+1}^{*2}\right]}\Bigg]\Bigg\}$$

where

$$\Delta C_\ell = \frac{\Gamma}{bU} \tag{58}$$

The constant $A(n)$ (reference to the starting condition where the value of circulation is assumed to be Γ_0) follows directly from Equations (35), (36), and (37), and may be expressed in terms of the step function H as,

$$A(n) = \frac{1}{\pi b}\left[\Gamma_0 + \Gamma H(n-\ell) - \Gamma H(n-m)\right] \tag{59}$$

Therefore the term $\frac{\pi}{U} A(n)$ in Equation (57) is given by,

$$\frac{\pi}{U} A(n) = C_{\ell_0} + \Delta C_\ell \left[H(n-\ell) - H(n-m)\right] \tag{60}$$

and

$$C_{\ell_0} = \frac{\Gamma_0}{bU} \tag{61}$$

It was noted earlier that the lift in a quasi-steady, circulation preserving flow is proportional to the value of A. Thus, Equation (60) indicates a step change in lift at two instants of time during a cycle of motion of the airfoil.

Since there are only steps changes in bound circulation, it follows from Equation (60) that

$$C_\ell = C_{\ell_0} \tag{62}$$

where no vortices are shed, and

$$C_\ell = C_{\ell_o} \pm \Delta C_\ell \tag{63}$$

where a vortex is shed.

The increment of circulation Γ is added for a vortex released from the trailing edge, and subtracted for a vortex released from the leading edge. Figure 7(b) depicts the behavior of lift coefficient with harmonic changes in angle of attack about a mean angle in the fully stalled regime. It is clear that the circulation preserving, vortex shedding exhibits a hysteresis loop. Beginning the cycle from the mean angle α_o, the airfoil proceeds to pitch up, maintaining constant lift. For the condition depicted in the figure, a vortex is released from the leading edge and the airfoil undergoes a sudden reduction in lift. The motion continues at constant reduced lift, pitching back down to minimum angle of attack, where a vortex is released from the trailing edge. This sequence of events generates a clockwise hysteresis loop and corresponds to a condition of negative damping. The amount of energy absorbed or dissipated represents the damping in the system and is proportional to the area enclosed by the loop. The sign of the damping depends on the direction of motion along the path. But these quantities are determined by just two parameters in the theory: the magnitude of circulation in the shed vortex, and the time of release of the vortices, i.e., the phase of shedding relative to airfoil motion. Thus, the damping in lift is entirely determined by these parameters.

To demonstrate how this is so, consider the alternatives sketched in Figure 7. In Figure 7(a), the pitch-up motion progresses from the angle α_o, and a vortex of strength Γ is shed from the leading edge

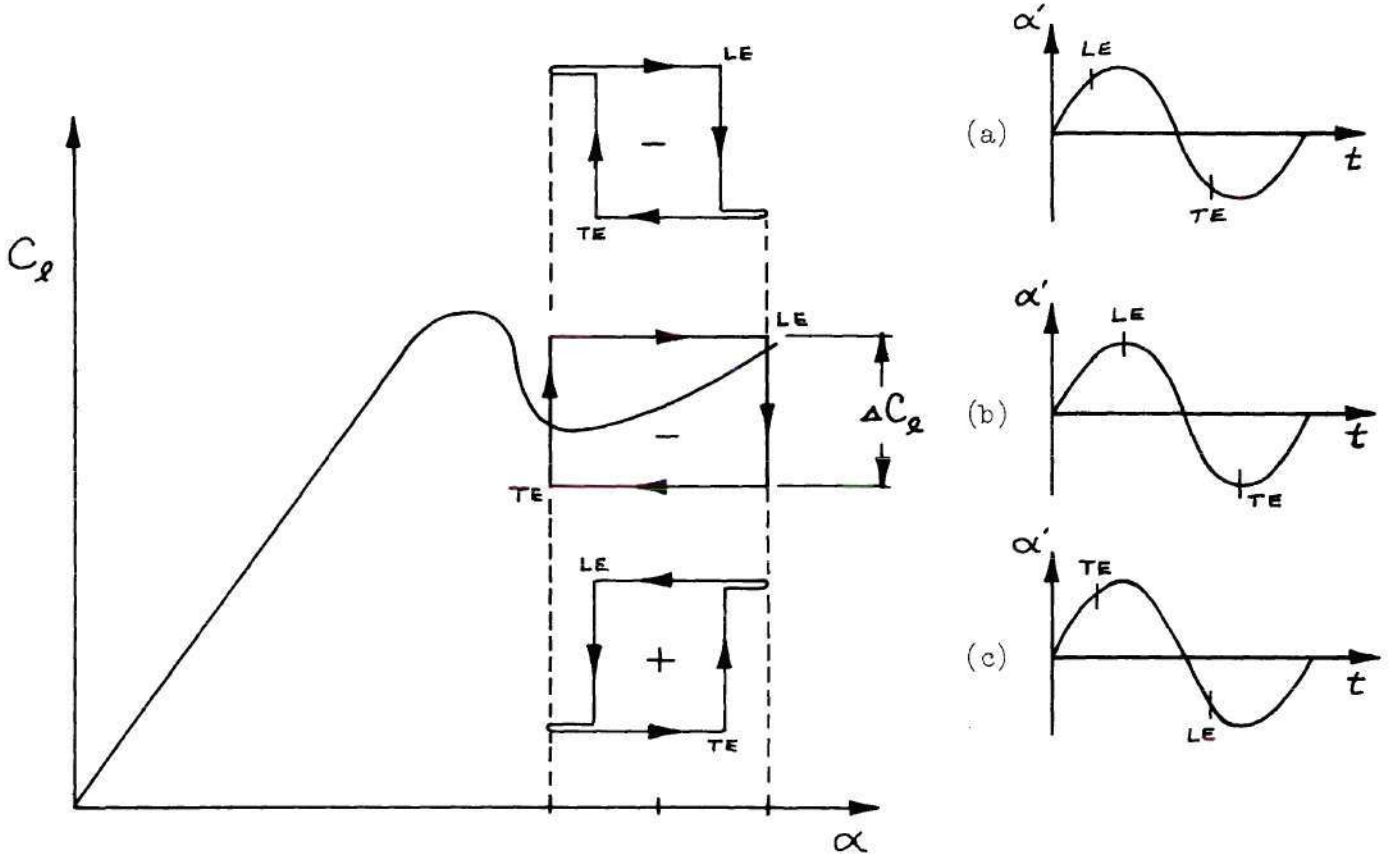

Figure 7. Effect of Vortex Shedding Phase on Lift Hysteresis Loop

before reaching the maximum angle $\alpha_o + \bar{\alpha}$. The motion progresses following the step change in lift, through the maximum angle and continues to pitch down through α_o, the trailing edge vortex is shed before reaching the minimum angle $\alpha_o - \bar{\alpha}$, and the lift is restored to the starting value before the cycle is completed. Part (b) of the figure depicts the situation when the vortices are shed at the limits of angular excursion. This clearly represents the limiting condition on the width of the hysteresis loop, and the depth is proportional to the magnitude of circulation released in the vortices. Part (c) of the figure indicates the conditions necessary for the generation of positive damping. If a trailing edge vortex is shed while $\alpha > \alpha_o$, then the hysteresis loop is traveled in the counterclockwise sense.

While it is clear that the process of circulation dumping cannot take place instantaneously, the representation just presented does describe the essential mechanism required of a circulation preserving system in order that a hysteresis loop be generated. The pitching moment associated with stall dynamics does not follow in simple closed form as did the lift coefficient. In order to evaluate the effect of vortex shedding on the hysteresis loop associated with pitching moment, it is necessary to consider the time history of the interaction of a shed vortex with the pressure distribution on the airfoil. Utilizing the result given in Equation (57), the moment coefficient is obtained by integrating over the chord for each time step. For numerical computation, the moment coefficient is obtained by summation as follows,

$$C_m = \frac{1}{2b} \sum_{n=1}^{R-1} -(X_n^* - \bar{X}^*) \Delta C_{Pa}(X_n^*) \Delta X^* \qquad (64)$$

where $\bar{X}^*$ denotes the point about which the moment is taken.

The time dependent behavior of the computed pressure, lift, and moment coefficient will be further discussed in the next section.

Analytical Results and Comparison with Measured Data

The expression given in Equation (57) has been programmed for a digital computer, and the resulting pressure and moment coefficients computed for a large number of time points in the cycle of motion. In this section, the effects will be evaluated of varying the magnitude of shed circulation, Γ , or the corresponding ΔC_l, the relative velocity of propagation, U_v , and the release time or shedding phase, on the airfoil pressure distribution and hysteresis response. The effect of the proximity of wake vortices is also examined. The pressure, lift, and moment data obtained by Liiva and Davenport [5] are convenient for qualitative comparison with the analytical results obtained here. In particular it is noted from the time histories of chordwise pressure as given in Reference [5] that there is a sudden loss of leading edge suction during part of the period of oscillation of the airfoil. In most cases where this behavior is observed, it takes place in a period of about one-thenth of a cycle. Figure 8, taken from Reference [5], depicts the general behavior for a sequence of times following the onset of leading edge suction loss. Using the analytical model developed in the last section, the phenomenon of leading edge suction loss can be clearly

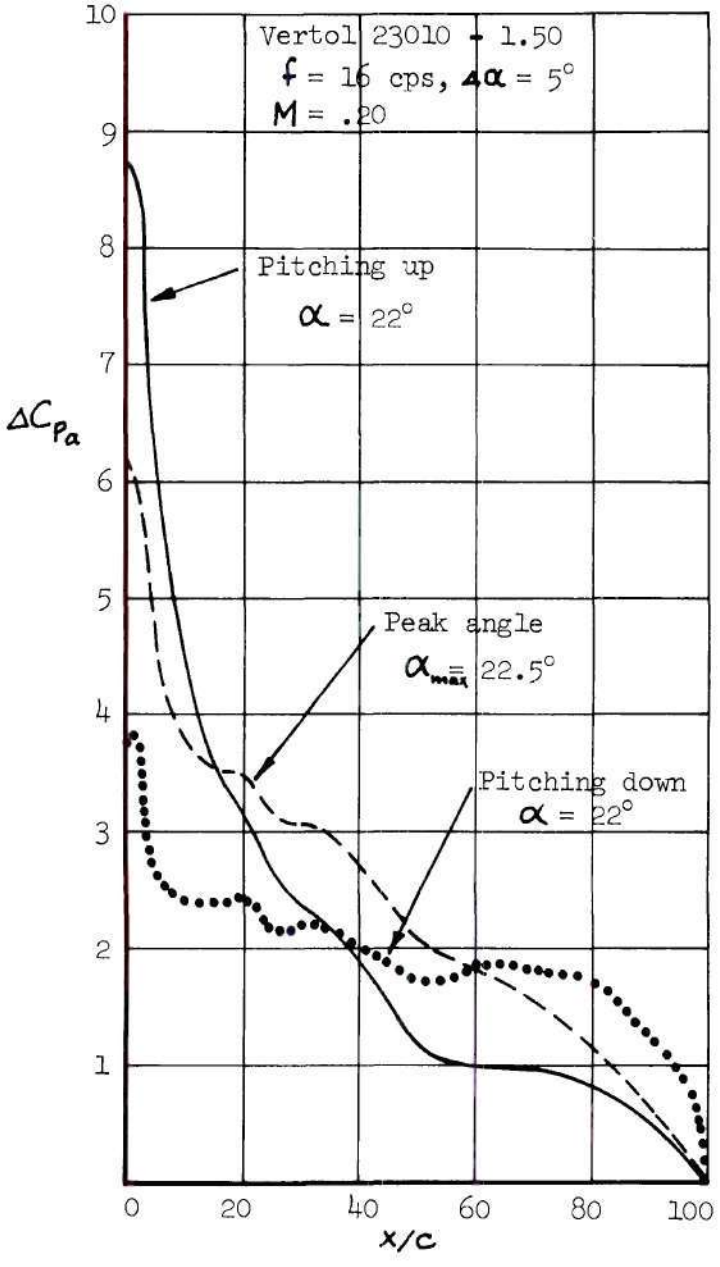

Figure 8. Experimental Pressure Distribution in Oscillatory Stall

demonstrated to occur with the sudden shedding of a discrete vortex from the leading edge. For example, using the flat plate data given in Figure 4 to determine C_{ℓ_0}, as discussed previously, and assuming the condition U = 100 ft/sec., $\alpha_0 = 17.5°$, $\bar{\alpha} = 1.5°$, and f = 30 cps, the timewise variation of chordwise pressure shown in Figure 9 results. For this case the values, $\Delta C_\ell = .10$, $U_v/U = .60$, were taken as reasonable from a general consideration of test data given in previously cited investigations. For this case, two vortices are placed downstream from the leading and trailing edge separation points as described in the previous section. The leading edge vortex was released at maximum angle of attack and the trailing edge vortex was released at minimum angle of attack. Shown in Figure 9(a) is the pressure coefficient distribution for a sequence of times during the cycle of motion, the solid line denoting the distribution in the pitch-up motion just prior to release of the leading edge vortex. The loss of pressure recovery at the trailing edge is evident for this case, indicating a highly stalled condition. The second line indicates the pressure distribution shortly after release of the leading edge vortex, and shows that the vortex induces a large loss in pressure coefficient forward of its position at that instant. The dashed line indicates the pressure distribution at a later time when the vortex has moved farther aft. It can be seen that the greatest effect of the vortex on the pressure distribution occurs when the vortex is near the leading edge. This large decrease in leading edge suction compares with the behavior depicted in Figure 8. Figure 9(b) is a sketch of the lift curve for the flat plate, showing the relative smallness of the lift hysteresis loop

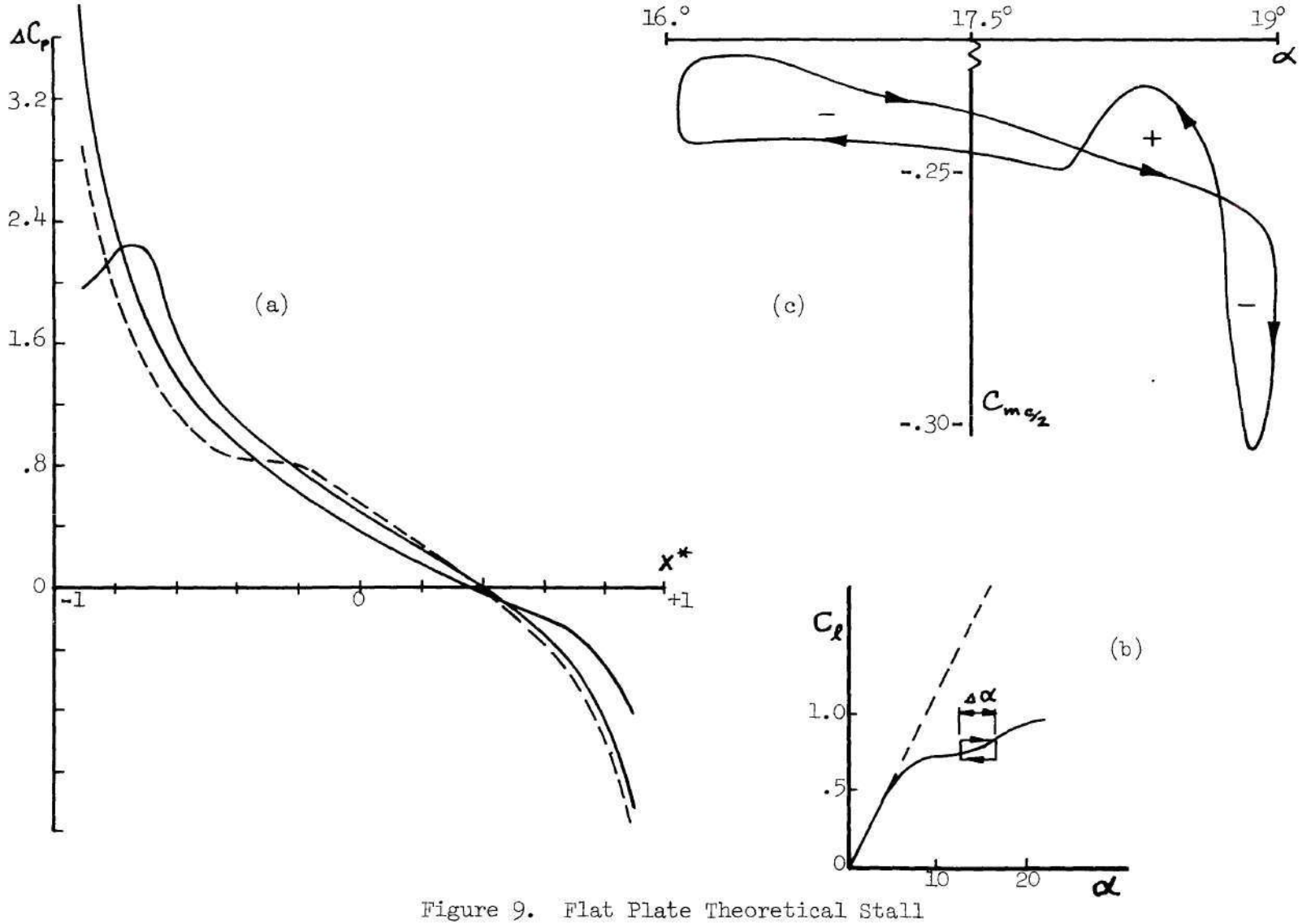

Figure 9. Flat Plate Theoretical Stall

for the hypothetical conditions in question. Both the width ($\pm$ 1.5°) and the depth ($\Delta C_{m_{\alpha}} = .10$) are small compared to the corresponding test values given in Reference [5]. Figure 9(c) shows the pitching moment coefficient, referenced to midchord, as a function of instantaneous angle of attack. The complex development of moment hysteresis for a fixed frequency of oscillation and vortex strength Γ, can be attributed to the combination of reference axis and vortex propagation velocity, assuming a fixed vortex shedding phase relative to angular position. The effect of shedding phase will be considered later, as will the further effects of vortex velocity. Considering the development of pitching moment in Figure 9(c), the value remains roughly constant during the pitch-up motion, then drops sharply following the leading edge vortex release at maximum angle of attack. This occurs due to the sudden loss in leading edge suction which induces a pitch-down moment. As the vortex progresses downstream, the leading edge suction recovers and the pitch-up effect predominates, the vortex being near the moment reference axis. This causes the moment to increase above the up-stroke value, then as the vortex progresses past the midchord the moment again reduces, finally recovering at minimum angle of attack when the trailing edge vortex is shed. This, in turn, causes an overall rise in chordwise pressure and a stronger leading edge singularity.

The above description of development of moment hysteresis emphasizes the importance of axis location for the condition of pure pitch. The remaining pitching moment calculations are referred to the quarter-chord of the plate, for this is the most commonly used reference point for aerodynamic data.

Conditions more closely approximating the test conditions indicated in Figure 1(a), as taken from Reference [5], are used to generate the solutions for pressure distribution in Figures 10 through 12. Estimated values of $C_{\ell} = 1.25$ and $\Delta C_{\ell} = .50$ were taken from Figure 1(a). The condition, $\alpha_0 = 17.5°$, $\bar{\alpha} = 5°$, $U_\infty = 220$ ft/sec., and $f = 16$ cps, was taken to approximate the test condition. The reduced frequency for this case is $k = .455$. The computer solution was generated for 20 times steps in one cycle of motion for 19 equally spaced locations between the positions $X^* = -1$, $X^* = +1$. Figure 10 shows the chordwise pressure distribution for a sequence of time steps in one cycle of motion. The values of n/N indicate the time, as a fraction of the oscillation period, for each pressure distribution, as defined in the previous section. The leading edge vortex is released at maximum angle of attack, corresponding to $n/N = .25$, and the trailing edge vortex is released at $n/N = .75$. The initial wake configuration contained two vortices convected from both the leading and trailing edges. For the condition shown in Figure 10, the vortex convective velocity parameter, U_v/U was taken as .80. The $n/N = .25$ curve denotes the pressure coefficient just prior to leading edge vortex shedding. The $n/N = .30$ curve shows the loss of leading edge suction and the rise in pressure immediately downstream of the vortex position. The $n/N = .50$ curve indicates that the vortex has already passed the trailing edge position and the overall downward shift in the curve due to loss of bound circulation is apparent. The $n/N = .85$ and $n/N = 1.0$ curves reveal an unusual effect, not generally observed in experimental data. After shedding of the trailing edge vortex, its effect is revealed in the neighborhood of the trailing edge

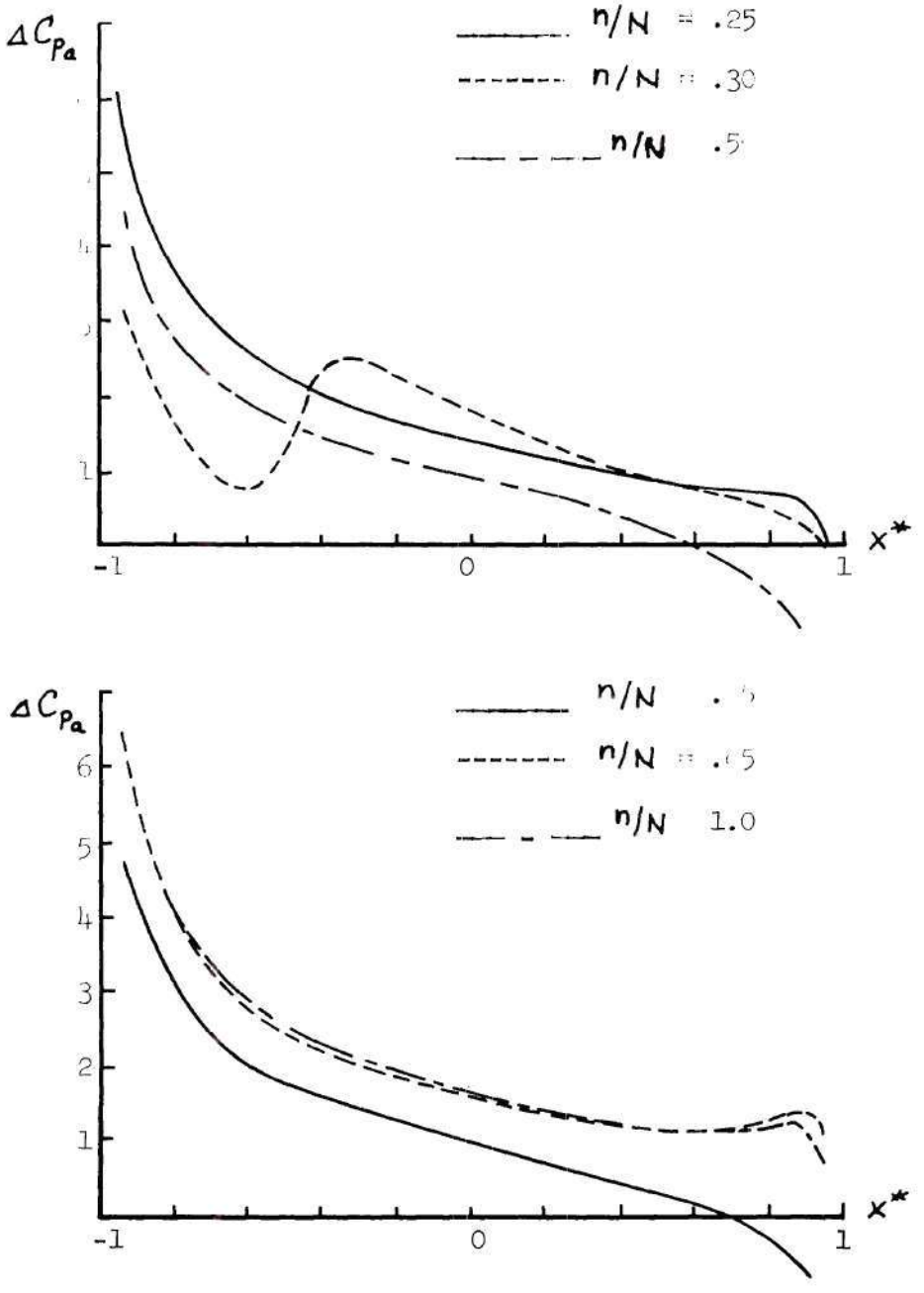

Figure 10. ime Dependent Chordwise Pressure Distribution α_o = 17.5 , $\bar{\alpha}$ = 5°, U_v/U = .80, C_{ℓ_o} = 1.25, ΔC_ℓ = .50

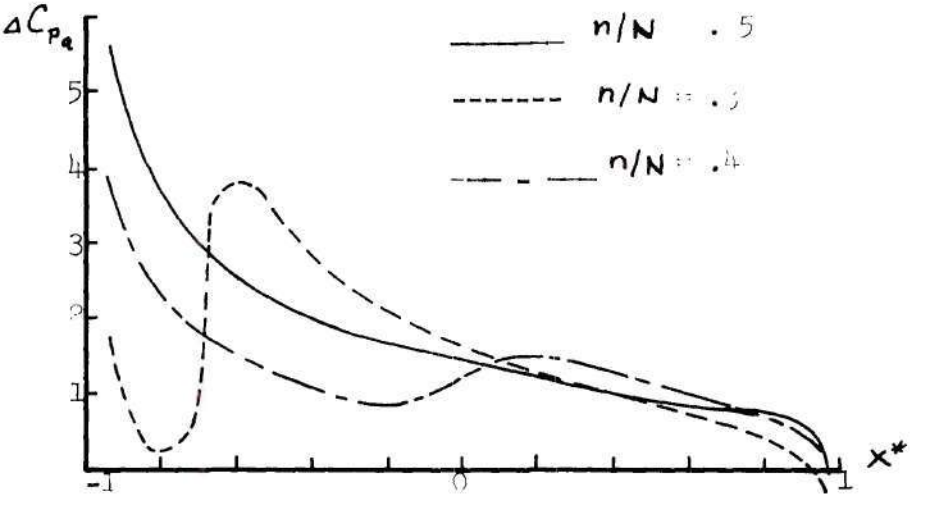

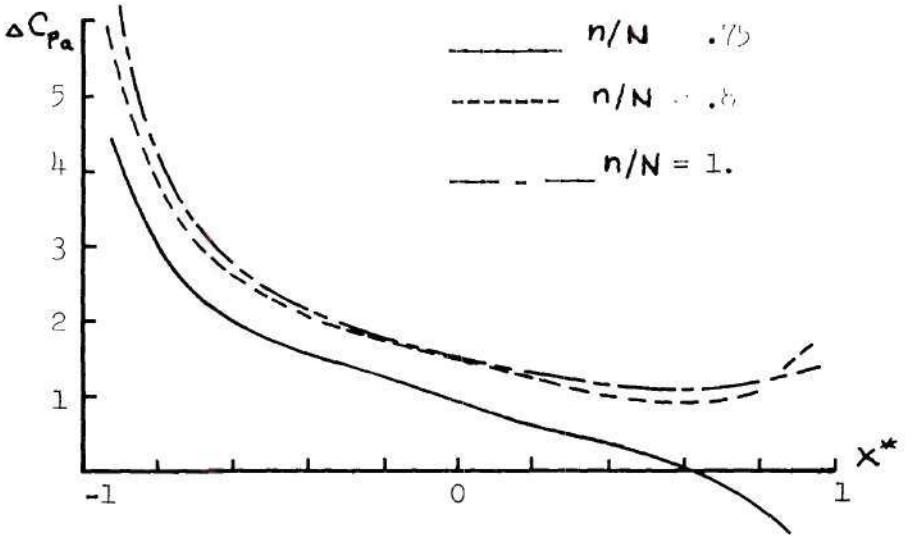

Figure 11. Time Dependent Chordwise Pressure Distribution

α_o = 17.5°, $\bar{\alpha}$ = 5°, U_v/U = .5, C_{ℓ_o} = 1.25

ΔC_ℓ = .50

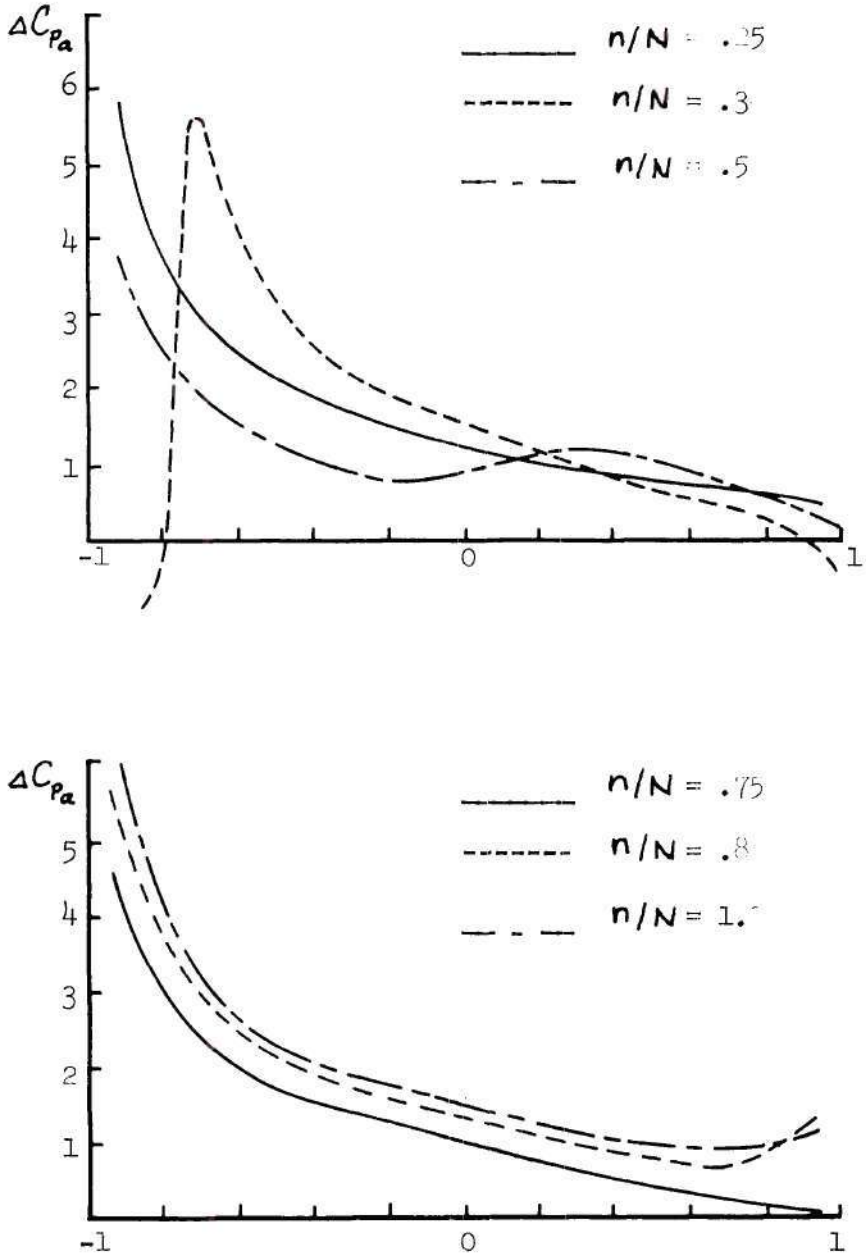

Figure 12. Time Dependent Chordwise Pressure Distribution

$\alpha_o = 17.5°$, $\bar{\alpha} = 5°$, $U_1/U = .33$, $C_{\ell_o} = 1.25$, $\Delta C_\ell = .50$

as a sudden increase in pressure coefficient, tending to recover the Kutta condition. This behavior suggests that the strength of the shed vortex may be unrealistically high or the assumption of discrete shedding in the immediate vicinity of the trailing edge is not a good approximation to the real circulation release process. The latter suggestion appears to be more reasonable, since the amount of circulation released in the neighborhood of the trailing edge should approximate, in absolute value, that released from the leading edge. While it is clear that the leading edge vorticity release occurs as a well-defined vortex, this may not be the case for the trailing edge, where the sheet of vorticity might travel well downstream before establishing complete roll-up. The trailing edge vorticity release would thus take place in a more continuous manner than the leading edge release. Further consideration will be given to the mechanism of wake development in the experimental section.

Figure 11 depicts the pressure distribution for the same conditions as in Figure 10 with the vortex convective velocity parameter reduced to $U_v/U = .50$, or one-half the freestream velocity. The distributions appear to be generally the same in shape and magnitude as for the higher convective velocity condition, with the exception of the behavior near the leading edge. The fact that the drop in leading edge pressure is greater for the lower convective velocity is apparently due to the vortex being closer to the leading edge in this case, since the time increment is the same for both cases ($n/N = .30$), thus creating a greater local modification of the pressure distribution. Figure 12 shows the effect of reducing the convective parameter to $U_v/U = .33$.

The leading edge effect is very marked, there being a change in sign of the pressure coefficient near the leading edge. Again, the approximation of the real flow is apparent since the actual location of the roll-up of a discrete vortex is slightly downstream of the leading edge as can be seen in Figure 3. Whereas the present analysis assumes release to occur at the leading edge. The pitching moment coefficient versus angle-of-attack graphs for the three convective velocity conditions just discussed are given in Figure 13. Part (a) of the figure, for $U_v/U = .80$, shows a large positive damping loop and a small negative damping loop, which occurs in the up-stroke motion. Comparing parts (b) and (c) for $U_v/U = .50$ and $U_v/U = .33$ respectively, the obvious trend is toward decreased positive damping with decreasing convective velocity. It should be recalled that the damping in lift is negative for all these cases since the leading edge vortex was released at maximum angle of attack and the trailing edge vortex released at minimum angle of attack. Comparing the results of Figure 1(a) for about the same experimental test conditions with the analytical results for pitching moment, it can be seen that the two are quite different in shape. One obvious difference between the two is that the experimental moments given in Figure 1 are referenced to the 37.5% chord location whereas the analytical results are referenced to the 25% chord location. The importance of moment reference point has been noted previously. In view of the trend toward increased negative damping, i.e., reduction in size of the positive damping loop, with decrease in vortex convective velocity, it is implied that the experimental convective velocity is less than one-third of freestream

velocity, the case depicted in Figure 13(c). It will be recalled that in the background discussion of experimental results on the velocity of propagation of a stable array of vortices in the wake of cylinder, the approximate value $U_v = .8\,U_\infty$ was found. The large discrepancy between this value and the value implied above may depend on the difference in near-wake characteristics of a stalled airfoil and a cylinder. Further discussion of this point will follow the experimental results.

Another factor of importance is the phase of leading and trailing edge vortex shedding relative to airfoil position. In terms of phase angle relative to the airfoil angular oscillations, the results of Equation (60) may be interpreted as phase angles φ_{I+1} and φ_{J+1}, defined as follows

$$\varphi_{I+1} = 360\,\frac{m}{N} \tag{65}$$

$$\varphi_{J+1} = 360\,\frac{\ell}{N} \tag{66}$$

which defines the phase in degrees from the beginning of a cycle until the release of leading and trailing edge vortices respectively. The effect of shedding phase on pitching moment is demonstrated in Figure 14. The same condition depicted in Figure 12 for pressure distribution and Figure 13(c) for pitching moment coefficient is shown except that the shedding phase has been varied. The solid line, for $m/N = .15, \ell/N = .60$, represents a forward shift in phase so that

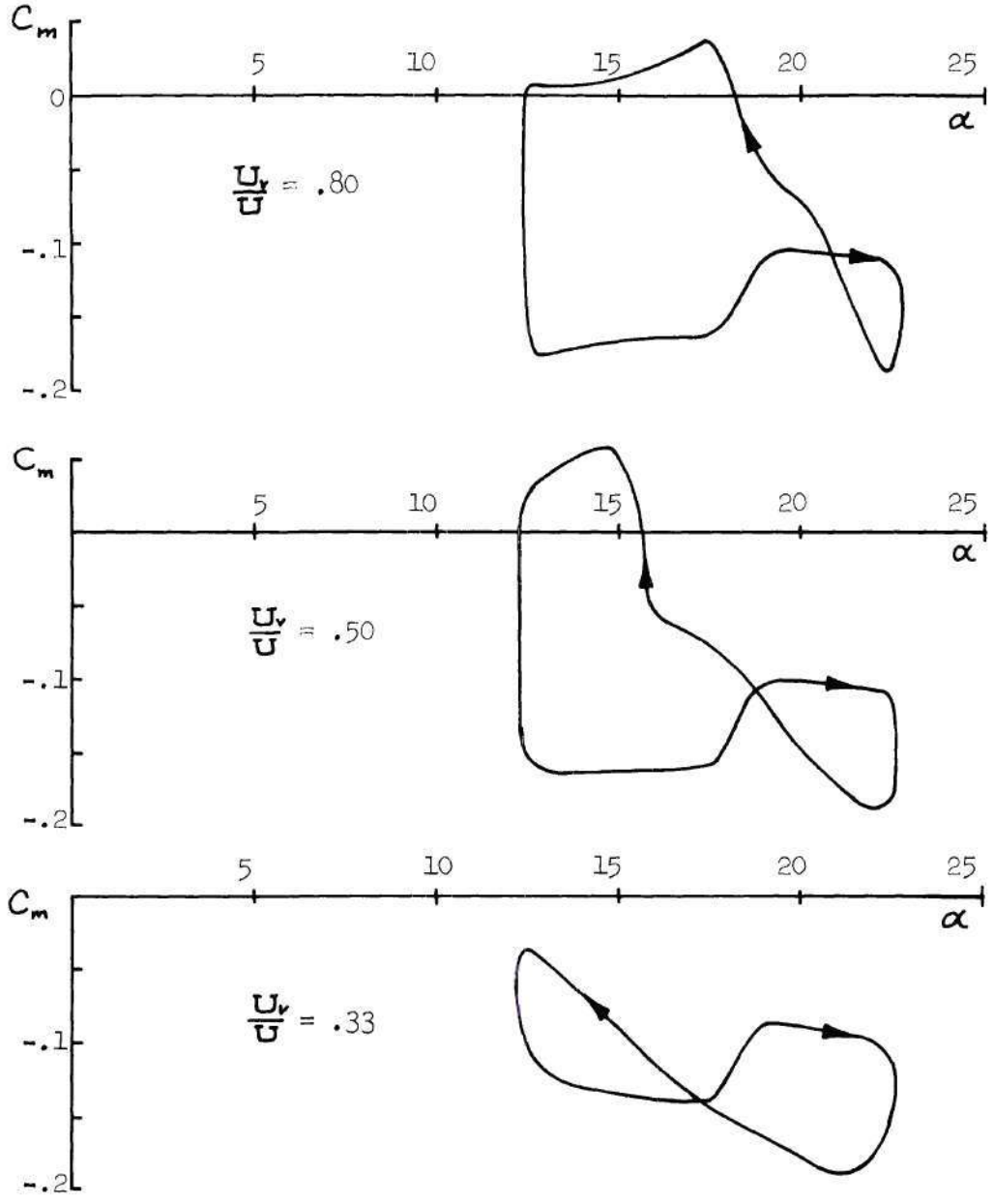

Figure 13. Effect of Vortex Propagation Velocity on C_m Hysteresis Loop, $\alpha_o = 17.5°$, $\bar{\alpha} = 5°$, $C_{\ell_o} = 1.25$, $\Delta C_\ell = .50$

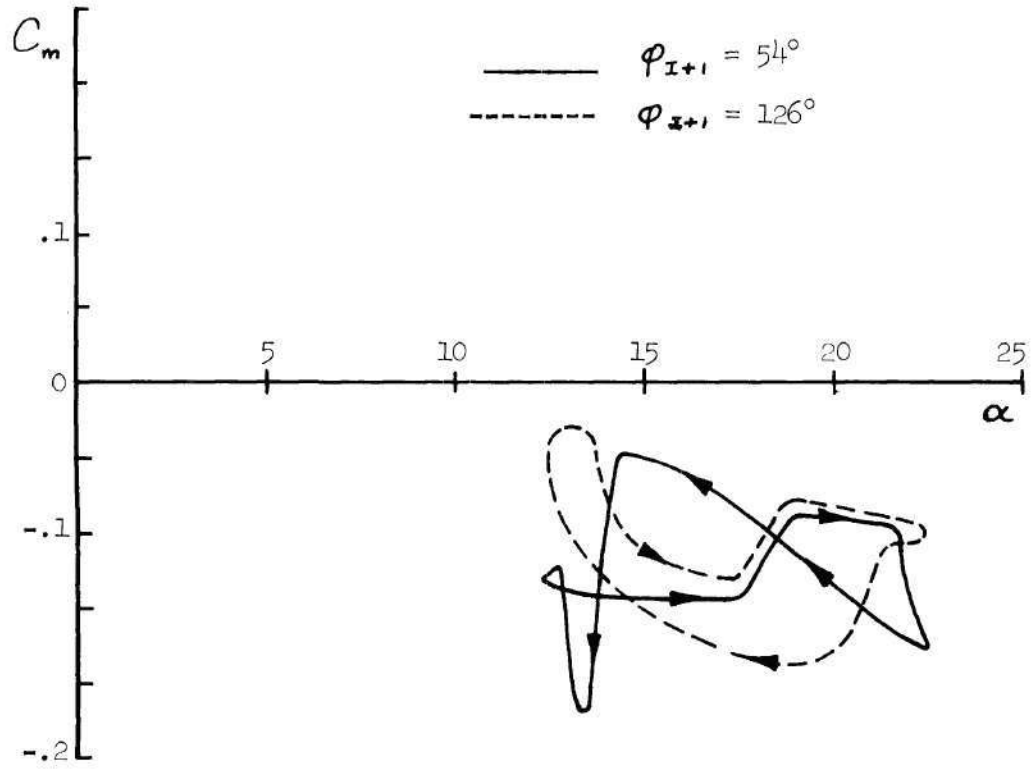

Figure 14. Effect of Vortex Shedding Phase on C_m Hysteresis, $U_v/U = .33$, $\alpha_o = 17.5°$, $\bar{\alpha} = 5°$, $C_{l_o} = 1.25$, $\Delta C_l = .50$

leading edge shedding occurs during pitch-up at an angle of attack of 21.5°, that is, one degree below the maximum angle, and $\varphi_{I+1} = 54°$, which is two degrees above the minimum angle of attack. In this case the the phase shift between shedding of leading and trailing edge vortices is 162°, whereas 180° shift has been used for all previous cases. For such conditions it is necessary that the lift hysteresis loop be unsymmetrical with respect to the mean angle of attack, that is, the loop would be similar to condition (a) depicted in Figure 7 except that the center of the loop would be shifted to the right due to the recovery of lift at an earlier angle, that is, at a higher angle, in the downstroke. The dashed line, for $m/N = .35$, $\ell/N = .85$, represents a delay in vortex shedding, so that the leading edge vortex is not released until maximum angle of attack is reached and the downstroke has begun, the release occurring at 21.5°, and $\varphi_{I+1} = 126°$. The trailing edge vortex is delayed in this case by the same amount as the leading edge vortex, being released after attaining minimum angle of attack, at 13.5°, and $\varphi_{I+1} = 306°$. It can be seen that the effect of delay is to cause the loop to become entirely clockwise, that is, destabilizing. It is clear from comparison of the two conditions of shedding phase that moment stall response is critically dependent on this parameter.

It was noted in discussing the steady stall pressure distribution that relaxing the Kutta condition required a forward movement of the trailing edge stagnation point, leading to a progressively stronger trailing edge singularity as depicted in Figure 6. However, experimental data as shown in Figure 8, and additionally in Reference [5], do

not reveal this type of trailing edge behavior. As shown in Figures 10, 11, and 12, the time dependent behavior of the trailing edge pressure is such that significient fluctuations occur in the asymptotic region near the edge. This suggests that in the mean, vorticity shed from the two airfoil separation points has a modifying effect on the "steady" pressure distribution. Figure 15 shows the pressure distributions resulting from placing initially two vortices downstream of the airfoil and then four vortices. The condition shown is $U_v/U = .33$, $\alpha_o = 17.5°$, $\bar{\alpha} = 5°$, $k = .455$ ($f = 16$ cps), $C_{l_o} = 1.25$, $\Delta C_l = .50$, and $n/N = .25$. This is, pitch-up motion is taking place just prior to release of the leading edge vortex. The solid line is the condition $I = 2$, $J = 2$, that is, there are two downstream vortices along the leading and trailing edge wake trajectories. This condition is the same as that shown as the $n/N = .25$ curve in Figure 12. The closed line is the condition $I = 1$, $J = 1$, that is, one vortex is placed downstream along each trajectory. For the latter condition the upper vortex is located 1.25 chordlengths downstream from the trailing edge and the lower one is 1.05 chordlengths downstream from the trailing edge. For the former condition there are vortices along the upper trajectory at 1.25 chordlengths and 3.55 chordlengths and at 1.05 and 3.35 chordlengths along the lower trajectory. Although this constitutes a highly idealized representation of the near wake, the details of which will be discussed in a later section, it serves to demonstrate the effect of downstream vortices on airfoil pressure distribution. It appears that accounting for the wake, as represented here, causes a slight increase in negative pressure near the trailing edge, without

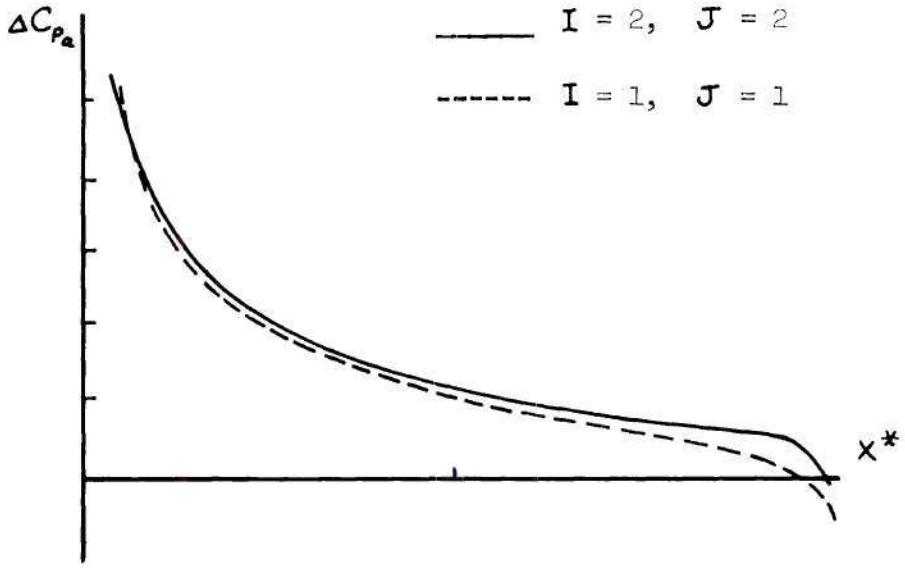

Figure 15. Effect of Downstream Vortices on Airfoil Pressure Distribution

changing the total lift. This result conforms more closely with measured mean stall pressure distributions. Thus the implication is that a true "steady-state" theory, as given by Equation (43), is inappropriate and the effects of wake vorticity must be accounted for in computing the mean pressure. This conclusion should be anticipated since stall flow is inherently unsteady.

The computations just presented point out the importance of several parameters in determining unsteady stall behavior. The magnitude of shed circulation, the velocity of propagation of the vortex along the airfoil chord, and the phase of vortex shedding relative to the airfoil motion, are all important in establishing whether energy is added to the motion or dissipated, and to what extent. The analytical solution has been shown to approximate observed experimental behavior in terms of the "anomalous C_m-loops" referred to in earlier investigations [7] using only the concept of conservation of circulation.

CHAPTER III

EXPERIMENTAL INVESTIGATION

The primary purpose of the experimental investigation was to evaluate the effects of airfoil oscillatory motion on the time dependent structure of the fully stalled near-wake. While there have been several extensive experimental studies of the behavior of airfoil aerodynamic loading in oscillatory stall, little attention has been devoted to the response of the airfoil wake under prescribed oscillatory conditions. Consideration of airfoil wake structure is important from the standpoint of further understanding the mechanism of stall dynamics and in determining the time dependent behavior as it affects the important problem of stabilizer buffet. Studies of the effect of transverse oscillation of a cylinder in a uniform flow indicate the existence of a Strouhal resonance, as discussed earlier. It was also noted that statically stalled airfoils and flat plates exhibit a characteristic vortex shedding frequency, which can be related to an equivalent Strouhal number. Thus, it is anticipated that an airfoil would exhibit a similar intensification of loading as was observed for the cylinder. However, it is apparent from considerations of the previous section that an airfoil may shed discrete vortices at frequencies other than that corresponding to Strouhal resonance. Since the analytical results indicated that the anamalous airfoil loading behavior could be explained on the basis of discrete vortex shedding, it becomes desirable to test

for the presence of such vortices under controlled conditions. Two questions are suggested:

(1) Under what conditions of velocity, mean angle of attack, and frequency of oscillation will the near wake exhibit discreteness?

(2) What is the structure and energy level of the wake corresponding to the conditions of discreteness?

The tests conducted as part of this research were designed to measure unsteady wake pressures for selected mean angles of attack, wind tunnel speed, and frequency for a fixed, small magnitude of oscillatory angle. These parameters were varied within the constraints imposed by the experimental arrangement to include combinations approaching the conditions of Strouhal resonance and extending to values approaching those used in other airfoil tests, for purposes of correlation.

Experimental Arrangement and Data Handling

Wind tunnel tests were conducted in the wind tunnel of the School of Aerospace Engineering, Georgia Institute of Technology. The tunnel has a circular test section with a diameter of nine feet. The maximum test section velocity is in excess of 200 feet per second. Tests were run for speeds ranging between 50 feet per second and 180 feet per second. The test airfoil was a NACA 0012 section with a chordlength of one foot; the span was 2.5 feet. The airfoil was fabricated using an aluminum plate with lightening holes, then a balsa wood section was bonded to the frame, thus providing a minimum weight, high-stiffness

dynamic test article. A one-inch diameter shaft was attached to each end of the airfoil at the 50% chord location, and the assembly was mounted in an A-fram test rig through bearings on either side. Large aluminum end plates were mounted in the frame to approximate two-dimensional flow conditions. The problem of approximating two-dimensional flow in wind tunnel testing is always difficult to resolve. In the present case, mechanical design constraints prevented the use of increased airfoil span, which usually contributes to a better approximation of two-dimensional flow. Two factors alleviate the problem for this investigation. First, since the wake measurements are taken in a vertical plane passing through the airfoil mid-span, it is expected that symmetry will cancel some of the three dimensionality. Secondly, an investigation similar to the present one but using a transversely oscillating cylinder [37] resulted in hot wire anemometer surveys in the spanwise direction demonstrating a high degree of coherency (two dimensionality) when the cylinder was placed in oscillation. The conclusion was that vortex shedding under oscillatory conditions forced the coherency. It is expected that this effect would be preserved for the case of a stalled airfoil. Figure 16 shows the complete test rig mounted in the wind tunnel. The view is looking downstream at the test arrangement. The base of the model was secure to the tunnel through two steel beams and additional bolts were extended downward through the tunnel wall to further minimize structural vibration. The drive system was powered by a one-horsepower electric motor with a variable-

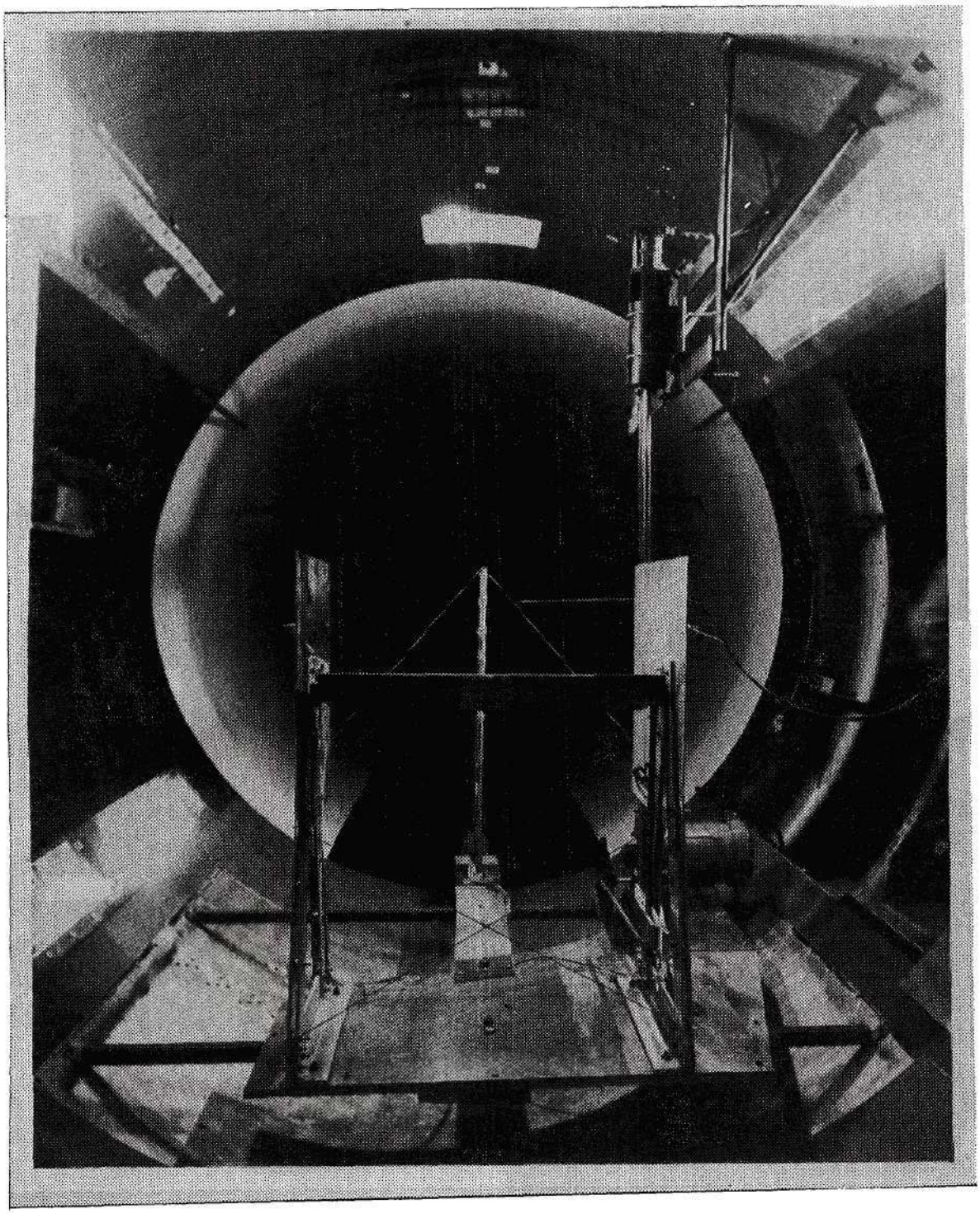

Figure 16. Downstream View of Experimental Arrangement in Wind Tunnel

speed, variable-torque controller. The motor was connected through pulleys to a flywheel, as shown in Figure 17, a pushrod leading from the flywheel to the input moment arm provided a fixed ± 1.5 degree oscillatory angle. The mean angle was adjusted by changing the pushrod length. The maximum frequency attainable with the system was 30 cps. Initial tests run with the model after installation in the wind tunnel revealed severe structural vibration problems. Additional flywheel balancing, correction of moment arm side bending, and installation of a 5/8-inch-thick base plate under the model reduced the problem considerably. However, there remained a structural resonance at about 25 cps which was apparently driven by pitching of the drive motor on the base plate. This was alleviated by installing a rigid rod between motor frame and the forward part of the base plate, as seen in Figure 17. A noticeable, but not severe, vibration amplitude remained at 25 cps, so this frequency was not included in the test conditions.

Instrumentation consisted of five absolute pressure transducers mounted downstream of the airfoil, two pressure transducers measuring the difference between upper and lower surface pressure on the airfoil at 15% and 85% chord locations, and a differential transformer attached to the moment arm and frame to measure airfoil displacement. The airfoil transducers, mounted at mid-span, are of the solid state type, with a .25-inch diameter sensing surface. The absolute pressure transducers were .125 inches in diameter and .031-inches thick. The vertical probe on which these transducers were mounted is seen in Figure 17. These transducers were mounted on the surface of a knife-edge extension of the forward extending probes, so that their sensing surfaces were in a

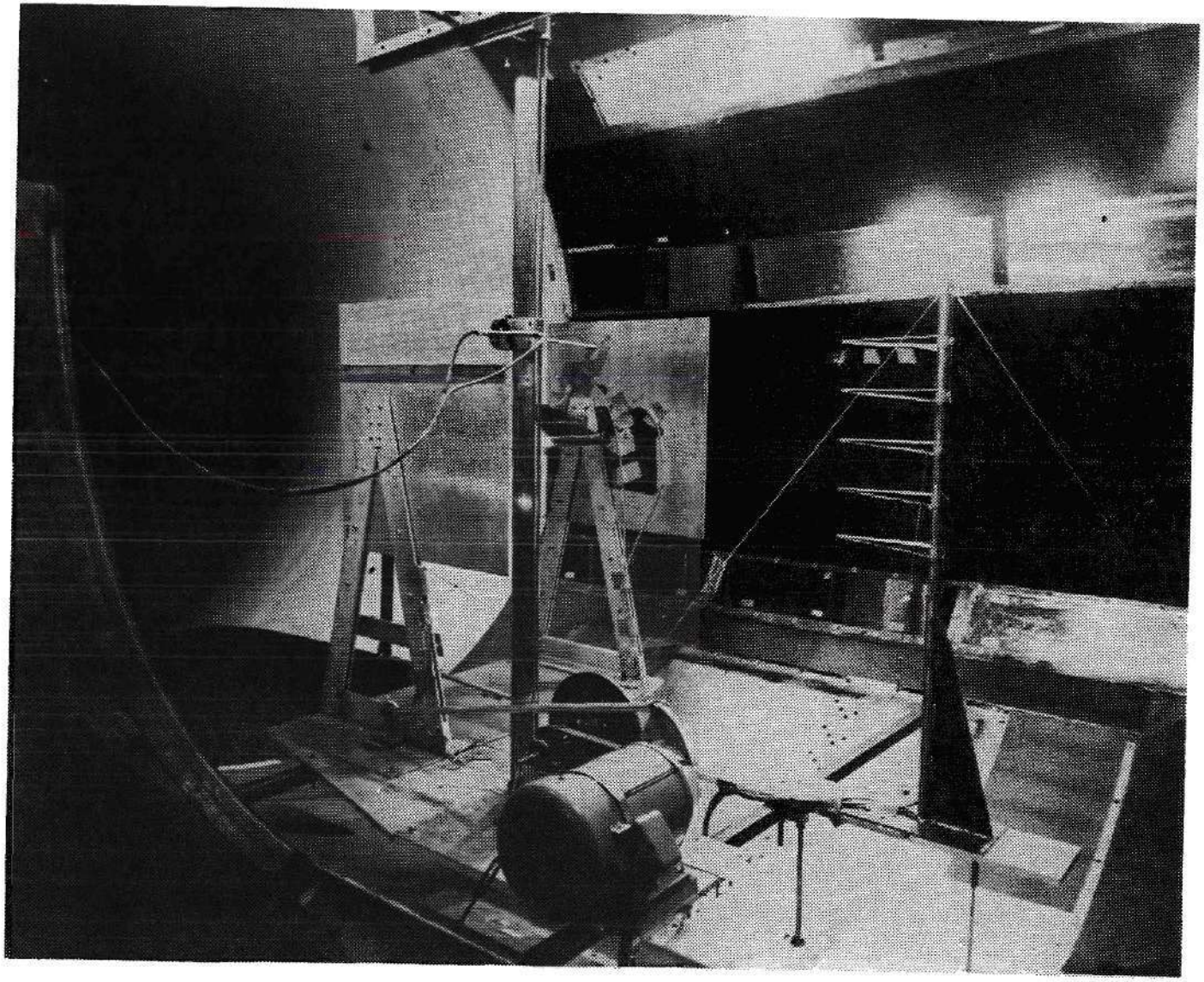

Figure 17. Exterior View of Experimental Arrangement in Wind Tunnel

single vertical plane. One of the transducers was placed in horizontal alignment with the pitch-axis of the airfoil. The other four were symmetrical displaced at four-inch intervals above and below the pitch-axis plane.

The power supply for all pressure transducers was obtained from dry cell batteries. Each transducer was connected to a four-lead, multiple-shielded cable, providing input voltage to the bridge with the output returned to the amplifier system. Each cable was provided with a floating ground referenced to the chassis of the bank of amplifiers, this alleviated the problem of electronic noise. Operational d.c. amplifiers were used to provide the signal gains required for the transducer outputs.

The data acquisition system is shown in the photograph of Figure 18. An Ampex Data Acquisition System, Model 100, was used to record sevel channels of data on FM tape. Real time monitoring was provided through a four-trace oscilloscope housed in the DAS-100. A Sanborn eight-channel recorder was used to obtain visual recordings of time histories. Figure 19 presents a schematic of the data acquisition procedure. Due to the tape recorder capacity of seven FM channels of data, it was necessary to choose seven channels from the eight transducers. Since the tests were intended primarily to investigate wake behavior, the differential transducer at 15% chord was considered of less value than any of the others and was recorded visually only. The absolute transducer outputs were reduced to fluctuation about a zero mean before amplification. This was convenient since the necessity of rebalancing the d.c. amplifiers was avoided when changing tunnel speeds.

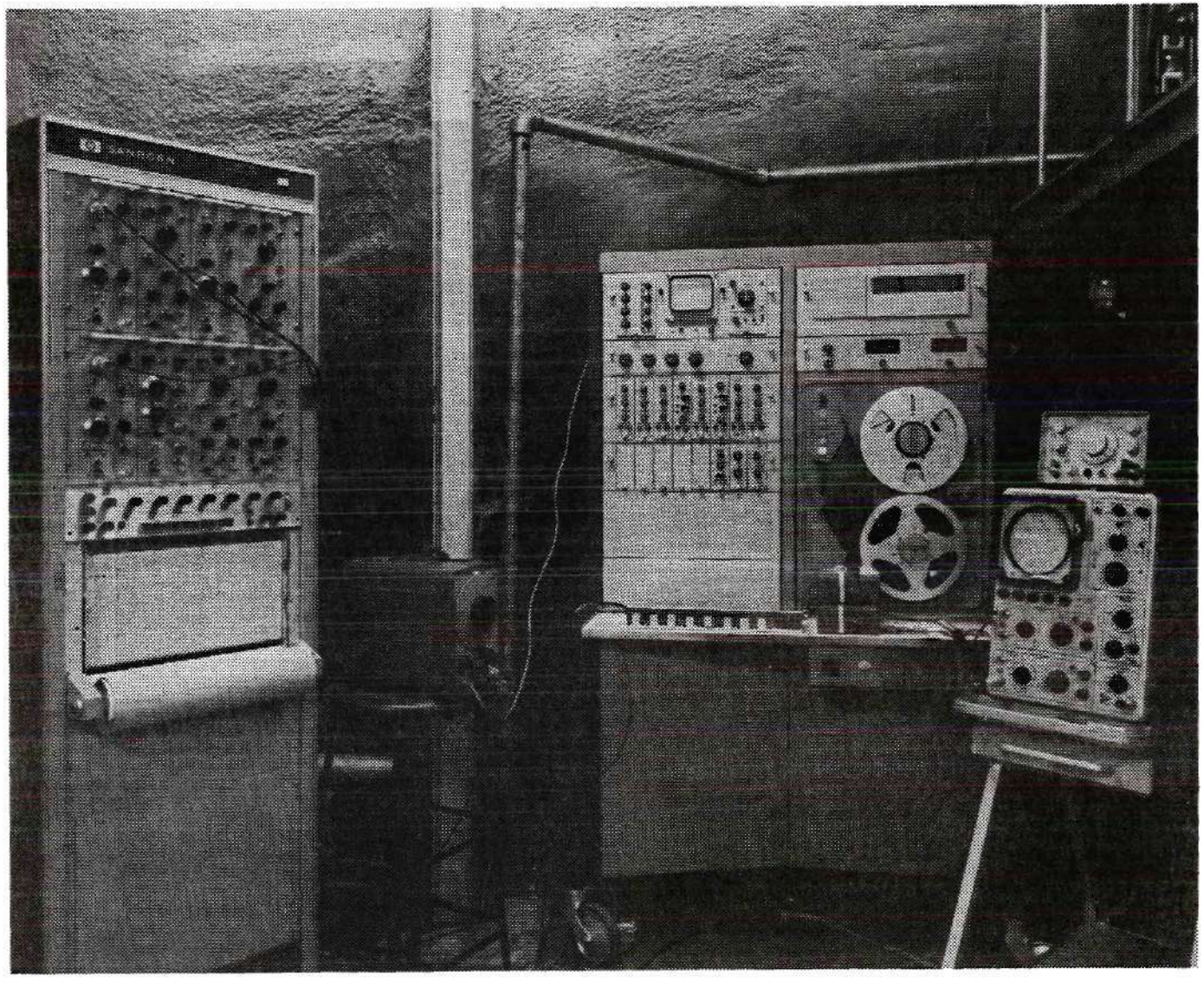

Figure 18. Data Acquisition and Monitoring System for Wind Tunnel Data

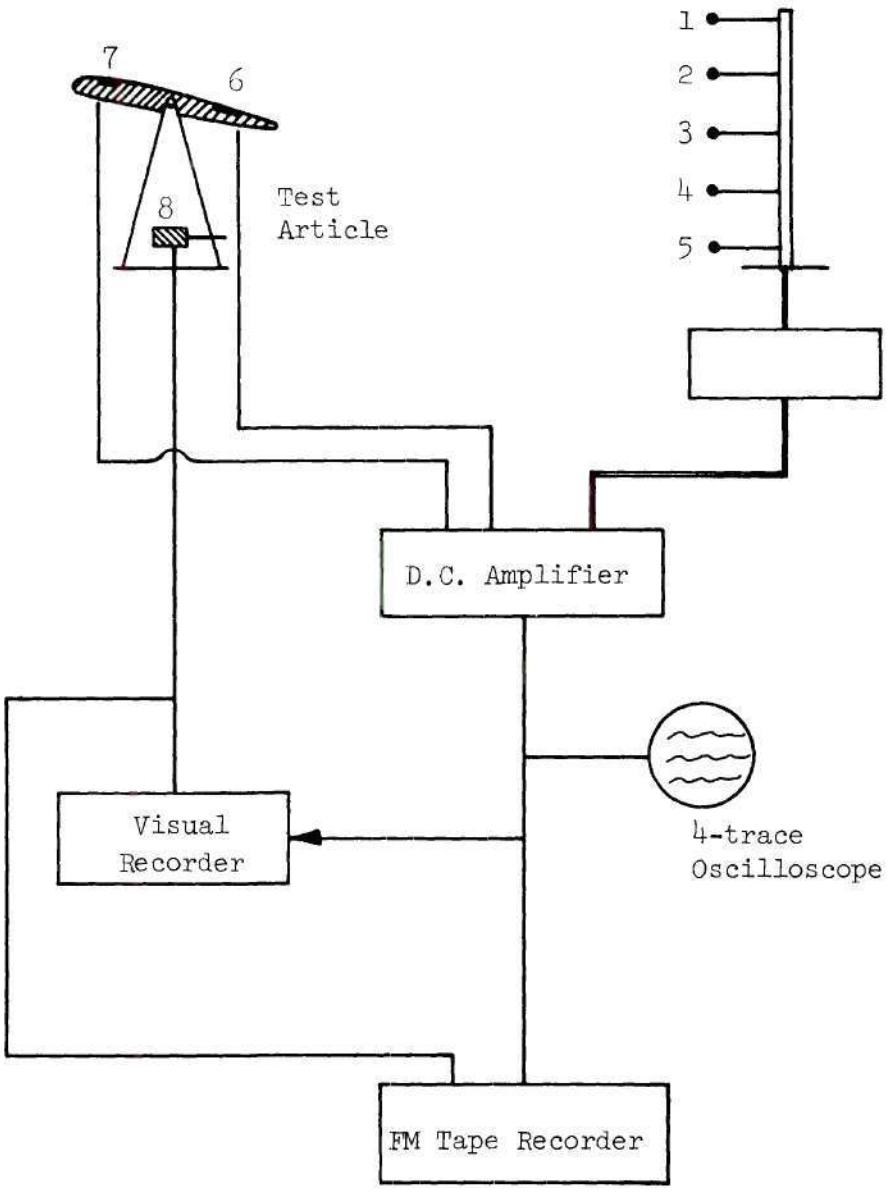

Figure 19. Schematic of Data Acquisition System

Also, the tests were intended only to study unsteady effects, so that mean pressures were not of interest. Details concerning instrument calibration and amplifier characteristics are given in Appendix B.

Following the recording of transducer time histories visually and on tape, the next step in data processing was to digitize the analog signals as given on tape. That is, the continuous recording of voltage versus time was sampled at discrete points in time, thus providing the data in a form which could be processed on a digital computer. For this purpose a CDC 6400 hybrid computer was used. Tape channels corresponding to wake transducers one through five, and the airfoil transducer at 85% chord, were fed into the analog console of the computer. The analog section of the computer was patched with a high-pass, four-pole Butterworth filter with breakpoint (the point at which the filter begins to roll off) at 2.5 cps and a low-pass filter with breakpoint at 90 cps. This electronic filtering system ensured the removal of extraneous d.c. components and high frequency noise.

The signal from the differential transformer was a modulated 400 cps carrier and could not be processed directly. A tracking filter was used to generate a sine wave in phase with the airfoil motion, and this was applied to the digitizing process. Each channel of data was passed through identical filtering, so that no relative phase shifting could occur. This was necessary since cross-spectral computations were to be made. After filtering, the data channels were sampled and digitized at a rate of 200 samples per second. Sample length on all digitized records was 51 seconds. Each record was subdivided into

20 equal length segments, then each segment was Fourier transformed by numerical means. The power spectrum is obtained from the discrete Fourier transform by

$$\Phi_p(\omega) = \frac{1}{2\pi T} P(\omega) P^*(\omega)$$

$$= \frac{1}{2\pi T} |P(\omega)|^2$$

where

$$P(\omega) = \int_{-T}^{+T} \Delta p(t) e^{-i\omega t} dt \tag{68}$$

$P^*(\omega)$ is the complex conjugate of $P(\omega)$, and the interval from $-T$ to $+T$ is the record length. Similarly, the cross-spectrum between two pressures P_1 and P_2 is found from

$$\Phi_{P_1 P_2}(\omega) = \frac{1}{2\pi T} P_1(\omega) P_2^*(\omega) \tag{69}$$

This quantity is in general complex and was used in the present study only to establish the phase relationship between the pressures measured at different spatial locations. The numerical scheme used to obtain the Fourier transforms described above is based on an algorithm developed by Cooley and Tukey [31]. An excellent introduction to this technique, called the "Fast Fourier Transform," and its application, is given by Bergland [32]. The method allows a significant reduction in computer

time required to obtain spectra from time history data.

The power spectra, presented in the following section, were computed for frequencies up to 100 cps. The spectral data obtained from the computer were recorded on tape, then read into an automatic plotter which generated semilog plots of power spectrum versus frequency in radians/sec. The spectra were computed and plotted at intervals of 4 radians/sec. The spectral amplitudes are defined in the usual sense as mean square amplitude divided by radian frequency, so that the contribution of fluctuating pressures with frequencies between ω_1 and ω_2 to the root mean square deviation of pressure from the mean value is given by

$$\sqrt{\overline{\Delta p^2}} = \left[\int_{\omega_1}^{\omega_2} \Phi_p(\omega)\, d\omega \right]^{1/2} \tag{70}$$

The power spectra were numerically integrated over the range from 2.5 cps to 100 cps, and the resulting rms pressures are provided with each computed spectrum.

Experimental Results and Discussion

Time history data were obtained from all pressure transducers (transducer numbers one through seven) and the airfoil position signal. Test conditions included three mean angles of attack, $\alpha_0 = 15.^\circ$, 17.5°, $20.^\circ$. The oscillatory angle was fixed at $\pm 1.5^\circ$. The oscillatory angle was significantly smaller than typical values used in previous airfoil stall tests. Wind tunnel speed was varied from 50 fps to 180 fps.

The lower speed limit was dictated by instrumentation sensitivity (see Appendix B) and the upper limit was due to tunnel surge, which began to appear at about 200 fps. The surge onset was observed only for the static, 20° angle-of-attack condition. A 10% reduction in maximum speed was sufficient to restore steady tunnel flow, with a margin of 20 fps. The frequency of airfoil motion was varied from static to 30 cps. Generally, the frequencies recorded were f = 0, 5.0, 10.0, 15.0, 20.0 and 30.0 cps. However, intermediate frequencies were sometimes recorded when visual monitoring of oscilloscope traces of wake pressure signals indicated that discrete wake response might be present. Two wake probe positions were used in the test series; speed, frequency, and mean angle-of-attack sequence were run first with the probe located one chordlength downstream from the airfoil trailing edge, then repeated with the probe located three chordlengths downstream. For the two probe positions, wind-off tests were conducted to determine the pressure at the probe under zero flow conditions. Visual monitoring of the probe transducer outputs during a frequency sweep from static to 30 cps revealed negligible response; consequently, wind-off corrections were not included in the data reduction.

The wake pressure data presented here are for the three chordlength position only. Evaluation of the pressure measurements at one chordlength downstream and at three chordlengths downstream indicated that characteristics of the time-dependent pressure field are preserved over the two chordlength distance, although higher frequency harmonics of pressure appear more sharply defined nearer the airfoil. To illustrate briefly, Figure 20 presents the power spectrum of fluctuating pressure

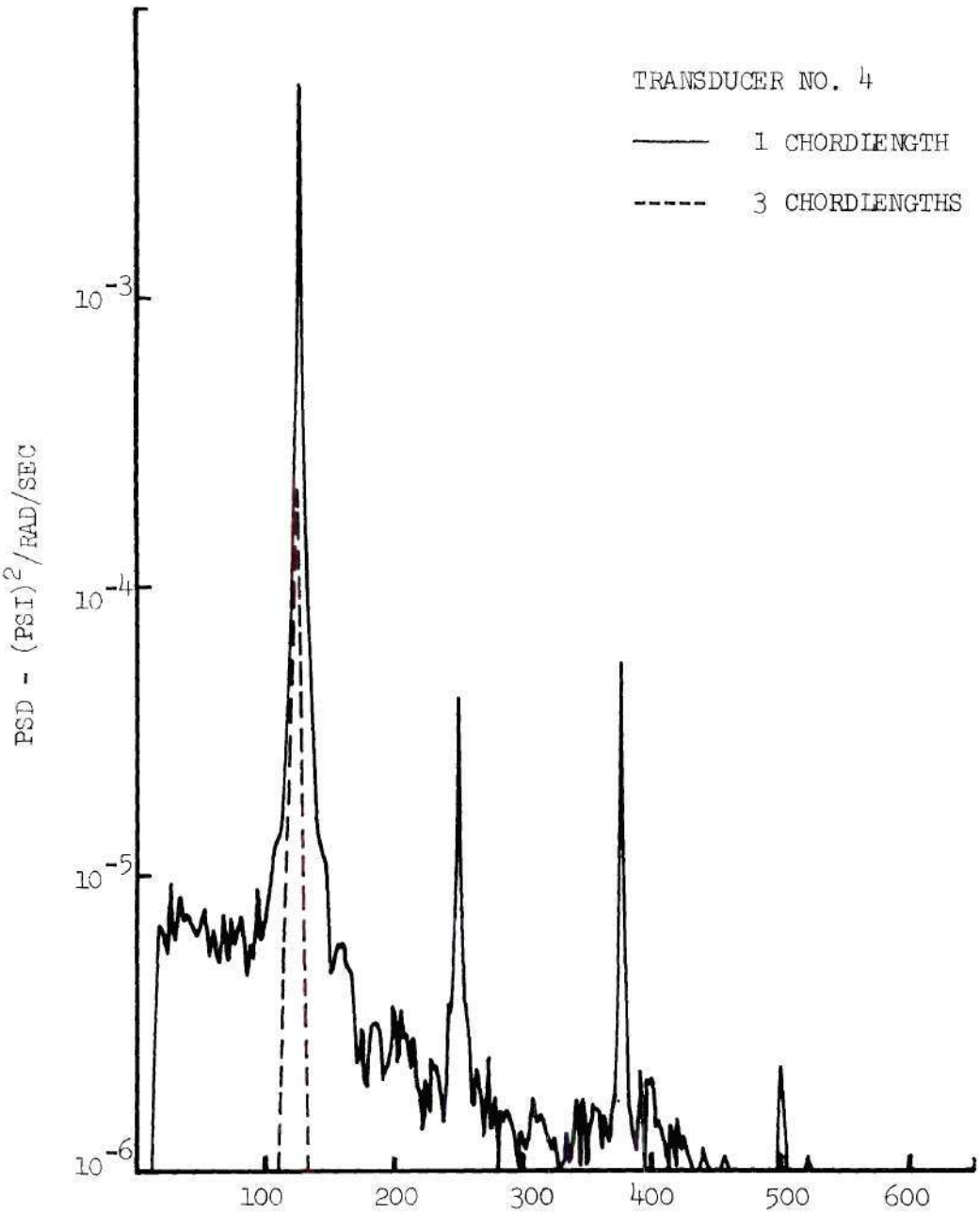

Figure 20. Power Spectra for Two Wake Positions Showing Effect of Streamwise Position

at the number four probe location at one chordlength downstream (the probe numbers are identified in Figure 19). The particular test condition is $\alpha_o = 15°$, $U_\infty = 180$ fps, $f = 20$ cps. Several higher harmonics are clearly present in the spectrum. These harmonics are less sharply defined at the three chordlength position. An interpretation of the harmonics will be given later. Data for the three chordlength position were chosen for detailed analysis, since the wake structure as it relates to stabilizer buffet was considered of importance. Figure 20 shows the spectrum for the same test condition, but at three chordlengths, superimposed as a dashed line. The remainder of the spectrum lies below the scale of the graph.

Figures 21, 22, 23, and 24 present time histories chosen to demonstrate the effect of oscillation of the airfoil on the pressure measured by the various transducers. Because of differing gains used on the Sanborn recorder channels, the several graphs are not at the same scale so that amplitudes shown are not representative of actual values. Plots from top to bottom correspond to the wake transducers numbered one through five respectively. The bottom trace in Figures 22 and 24 is the airfoil position indicator. The nature of the airfoil signal is such that the spike on the lower side of the trace corresponds to the maximum angle-of-attack position. The airfoil motion is sinusoidal, so that the position signal should be regarded only as a marker. Figure 21 shows the condition $\alpha_o = 17.5°$, $U_\infty = 60$ fps, at three chordlengths, and $f = 0$ cps. Figure 22 shows the same condition except $f = 15.0$ cps. It should be noted in this figure that plotter gains have been reduced such that comparisons cannot be made of the amplitudes. However, power

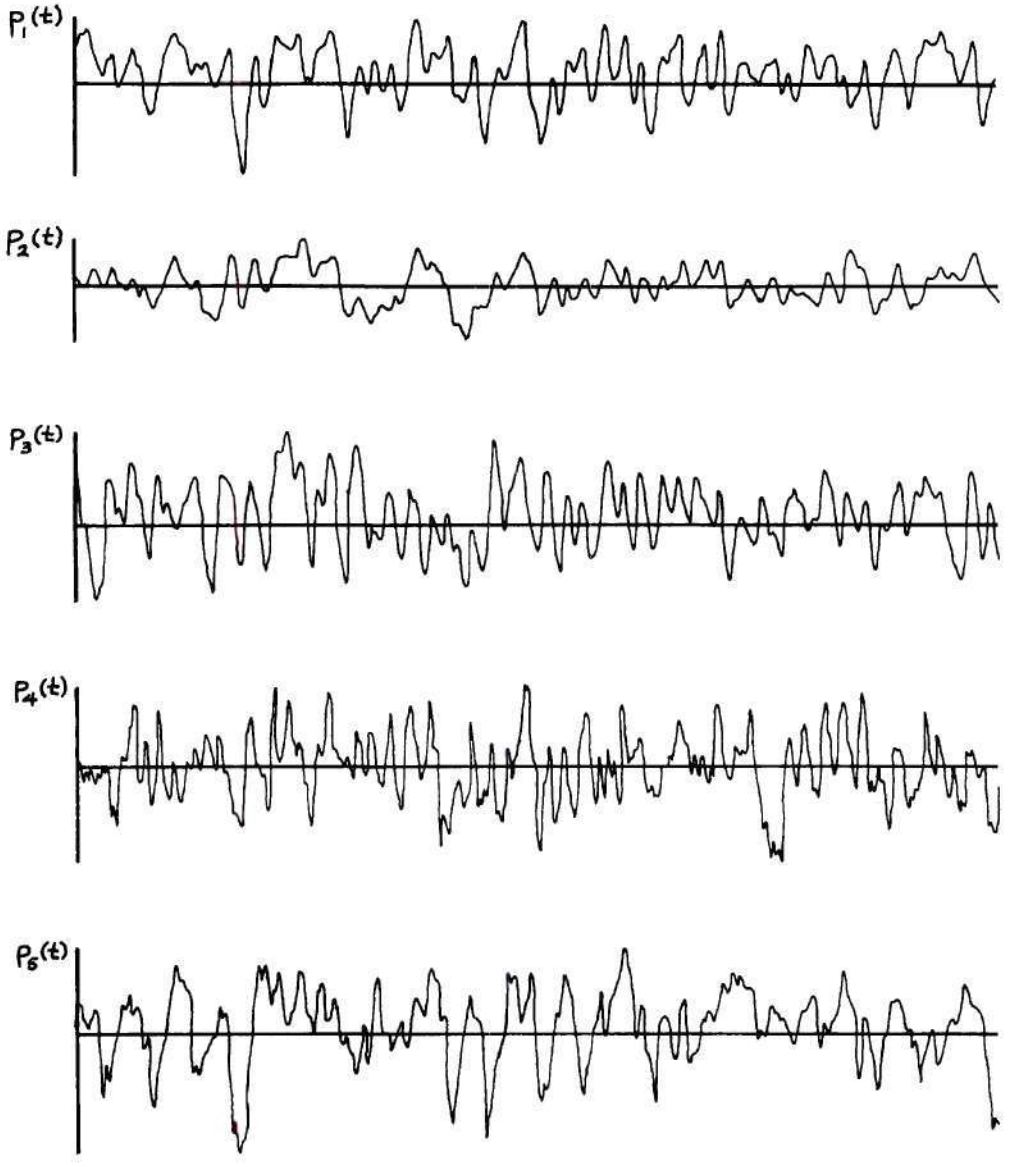

Figure 21. Sample Wake Pressure Time Histories, $\alpha_o = 17.5°$, $U_\infty = 60$ fps, $f = 0$ cps

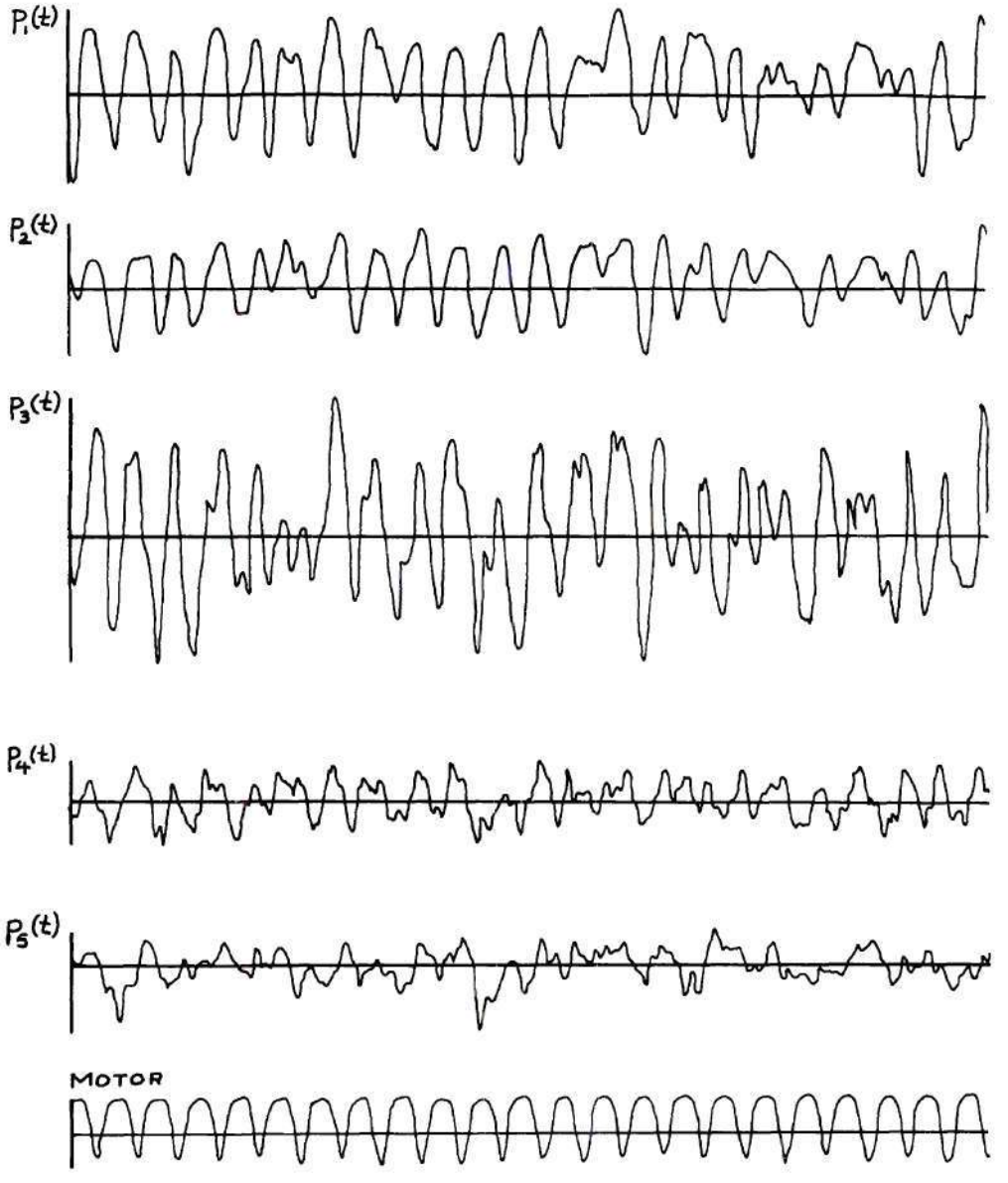

Figure 22. Sample Wake Pressure Time Histories

$\alpha_o = 17.5°$, $U_\infty = 60$ fps, $f = 15.0$ cps

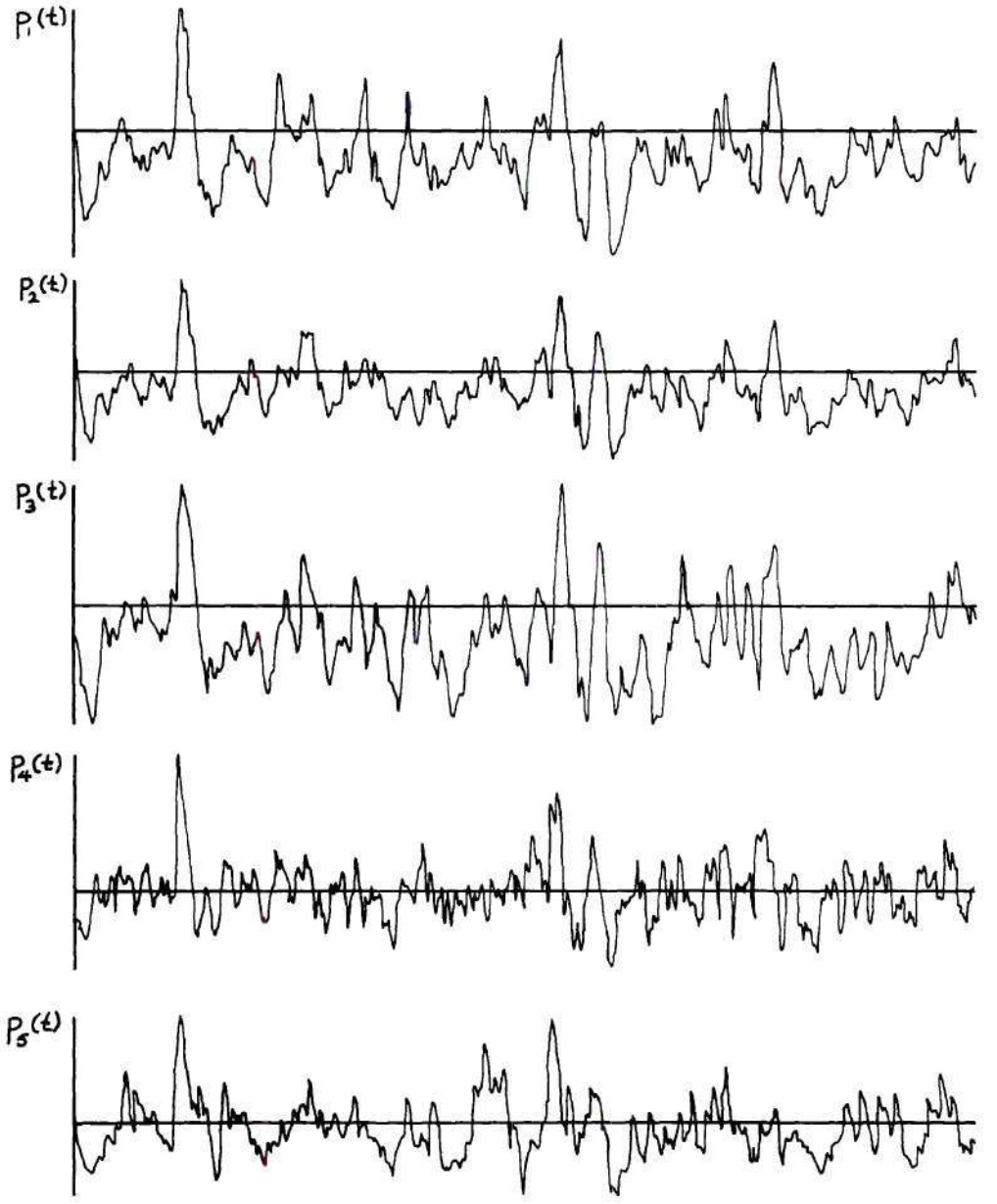

Figure 23. Sample Wake Pressure Time Histories,

$\alpha_o = 17.5°$, $U_\infty = 180$ fps, $f = 0$ cps

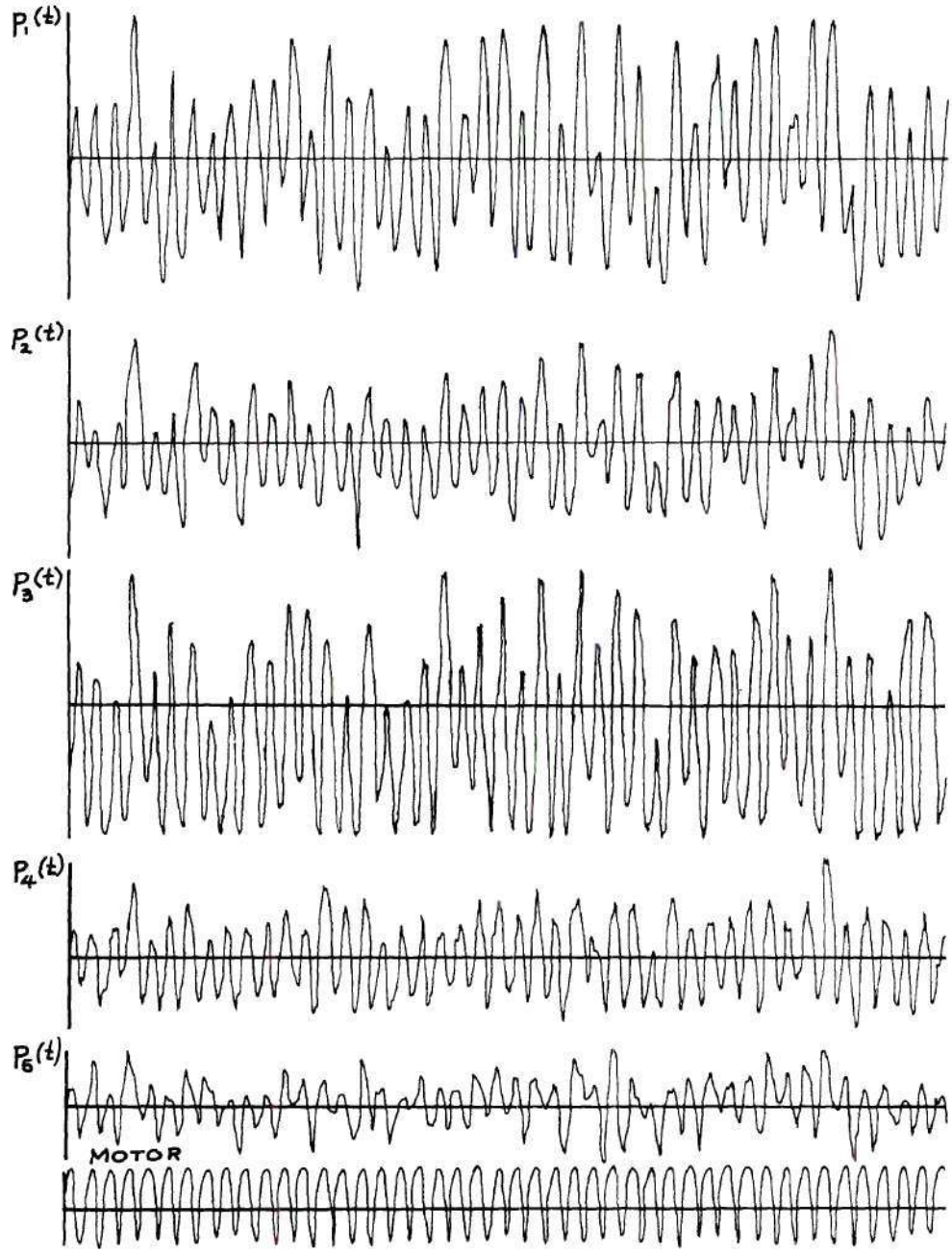

Figure 24. Sample Wake Pressure Time Histories, $\alpha_o = 17.5°$
U_∞ = 180 fps, f = 30.0 cps

spectra and rms pressures that will be given later show the relative amplitude at each frequency. It is evident in comparing Figures 21 and 22 that a significant increase in discreteness of the signal occurs under oscillatory conditions. Figure 23 shows the static behavior with increase in freestream speed. The test condition is the same as above except that U_∞ = 180 fps. Sharp, irregular peaks are evident, especially at positions one, two, and three, indicating strong non-periodic disturbances. The lower side of the wake shows greater high frequency content, indicating a more turbulent condition. Figure 24 shows the highly periodic structure resulting when the condition given in Figure 23 was changed from static to oscillatory, with f = 30.0 cps. The fundamental response is the same as that of the airfoil frequency, with some sub-harmonic response evident. The higher harmonics, while not discernible from the visual traces, can be seen in the spectral distributions to be presented later. Visual examination of all the time histories of wake response indicated that, in general, the effect of increase in airfoil frequency was to increase the discreteness of the wake.

Figures 25 through 28 present the power spectra corresponding to the time histories given in Figure 21 through 24. These spectra have been "smoothed" by plotting a mean line through the raw spectra as obtained from the computer. Appendix C presents computer spectra, without smoothing, for a large number of test conditions. Note that the power spectra exhibit sharp, low amplitude fluctuations imposed on the true spectral distributions. This is a result of the numerical processing and does not represent measured data. This effect is further

discussed in Appendix C. Figures 25 and 27 present power spectra of fluctuating pressures at the number two probe location for the static condition, $\alpha_o = 17.5^\circ$, and freestream velocities $U_\infty = 60$ fps and 180 fps respectively. Figures 26 and 28 are the same conditions except $f = 15$ cps and $f = 30$ cps respectively. Note that all these spectra refer to the number two transducer, which is the time history labeled $P_2(t)$ in Figures 21 through 24. Figures 26 and 28 are presented here only to show the effect of airfoil motion. The question of coincidence between natural and forced Strouhal number will be considered later. The ordinate has the dimensions of pounds per square inch divided by radian frequency, so that the area under the curve represents the mean square pressure, as discussed previously. These plots show a relative peaking followed by a roughly linear drop-off in amplitude. The peak represents the natural vortex shedding frequency for bluff bodies. It was found that the peak is not always well defined, but instead somewhat flattened or smeared. Some broad-bandedness may be expected due to the Reynolds number regime of the tests. However, for most conditions tested the peak was sufficiently well defined to permit calculation of the Strouhal number.

Using the spectra of Figures 25 and 27, and the additional spectra for static conditions given in Appendix C, the Strouhal number is computed from

$$S_n = \frac{N c \sin \alpha_o}{U_\infty} \tag{71}$$

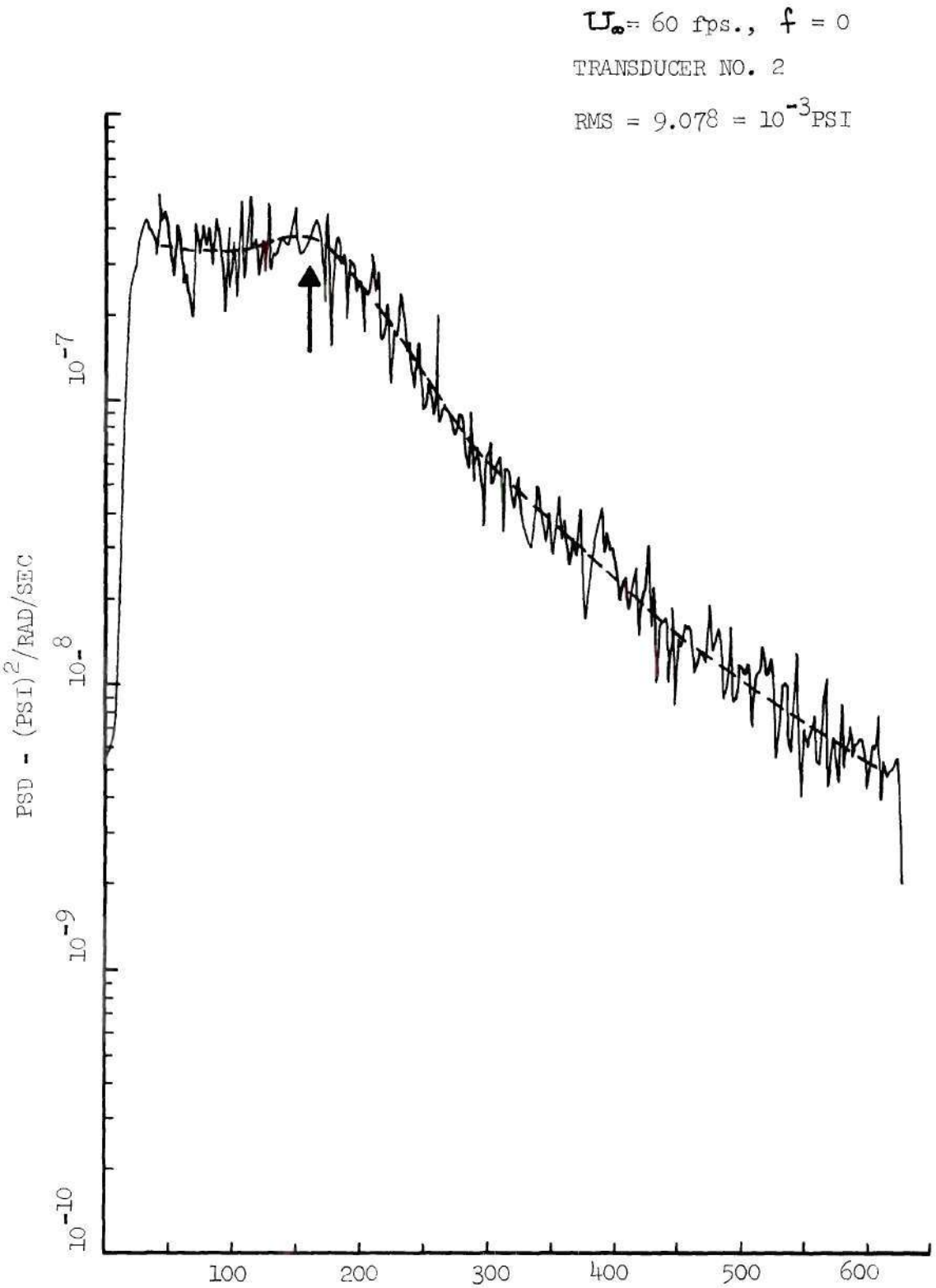

Figure 25. Sample Power Spectrum of Wake Pressure

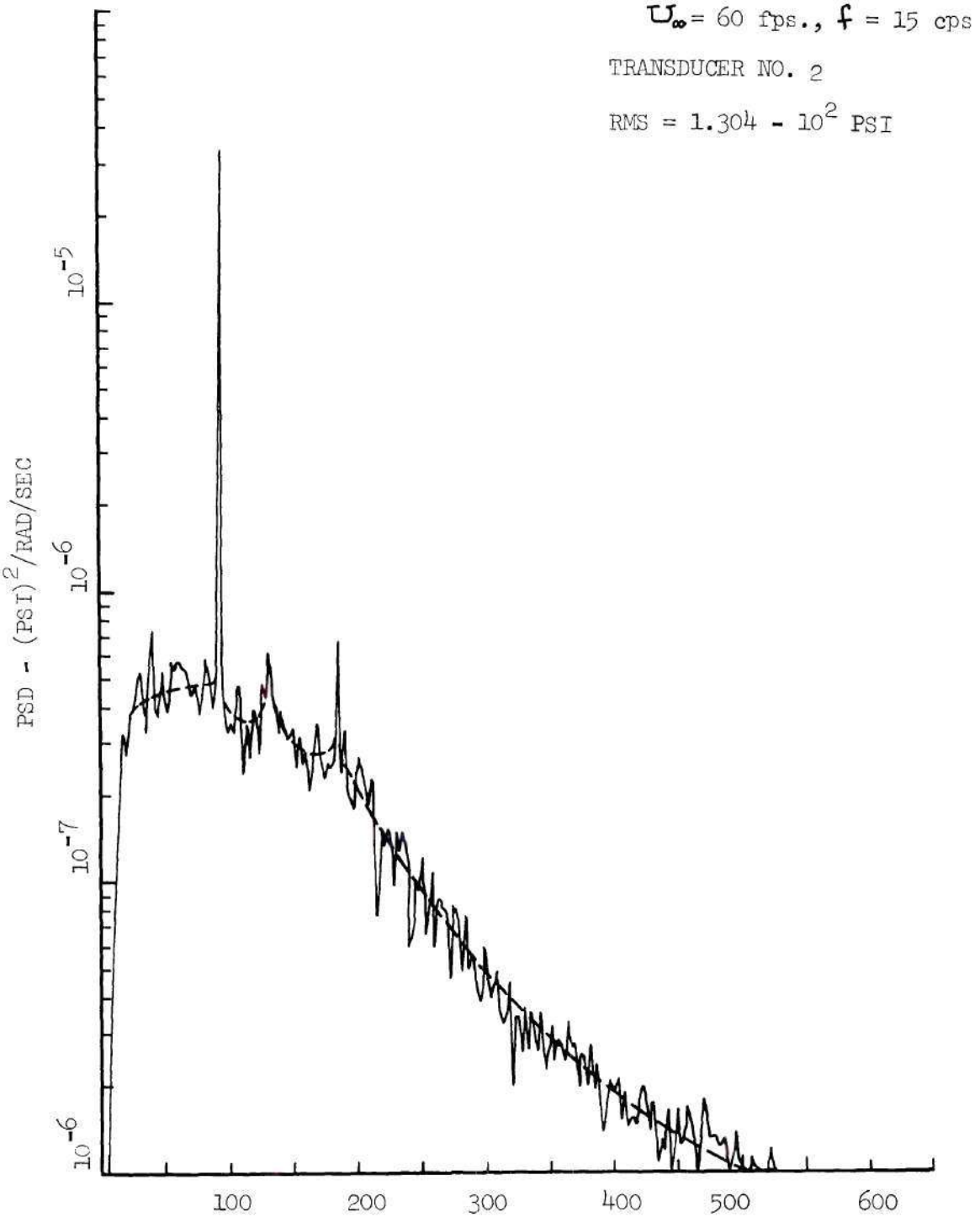

Figure 26. Sample Power Spectrum of Wake Pressure

U_∞ = 100 fps, f = 0

TRANSDUCER NO. 2

RMS = 1.325 = 10^2 PSI

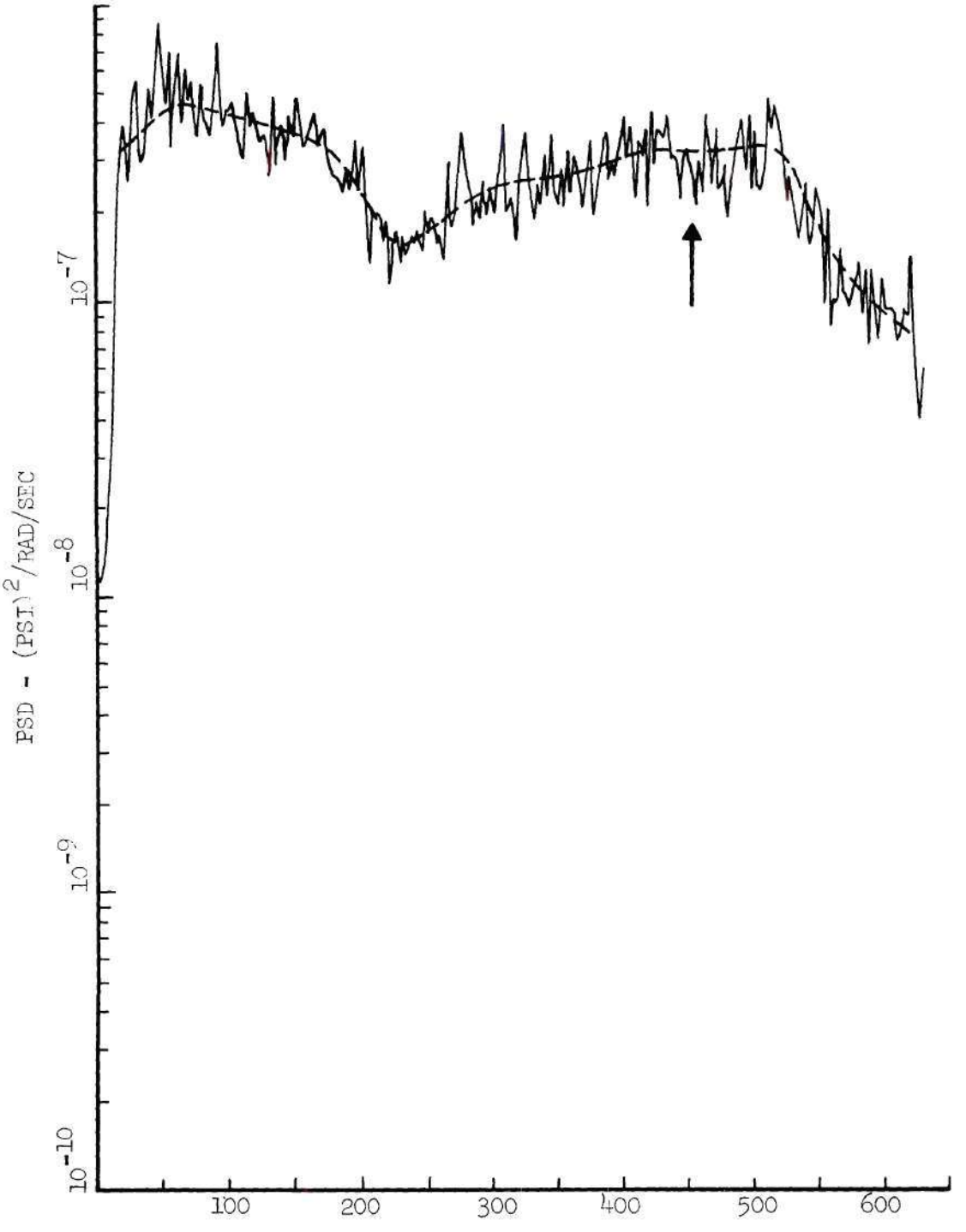

Figure 27. Sample Power Spectrum of Wake Pressure

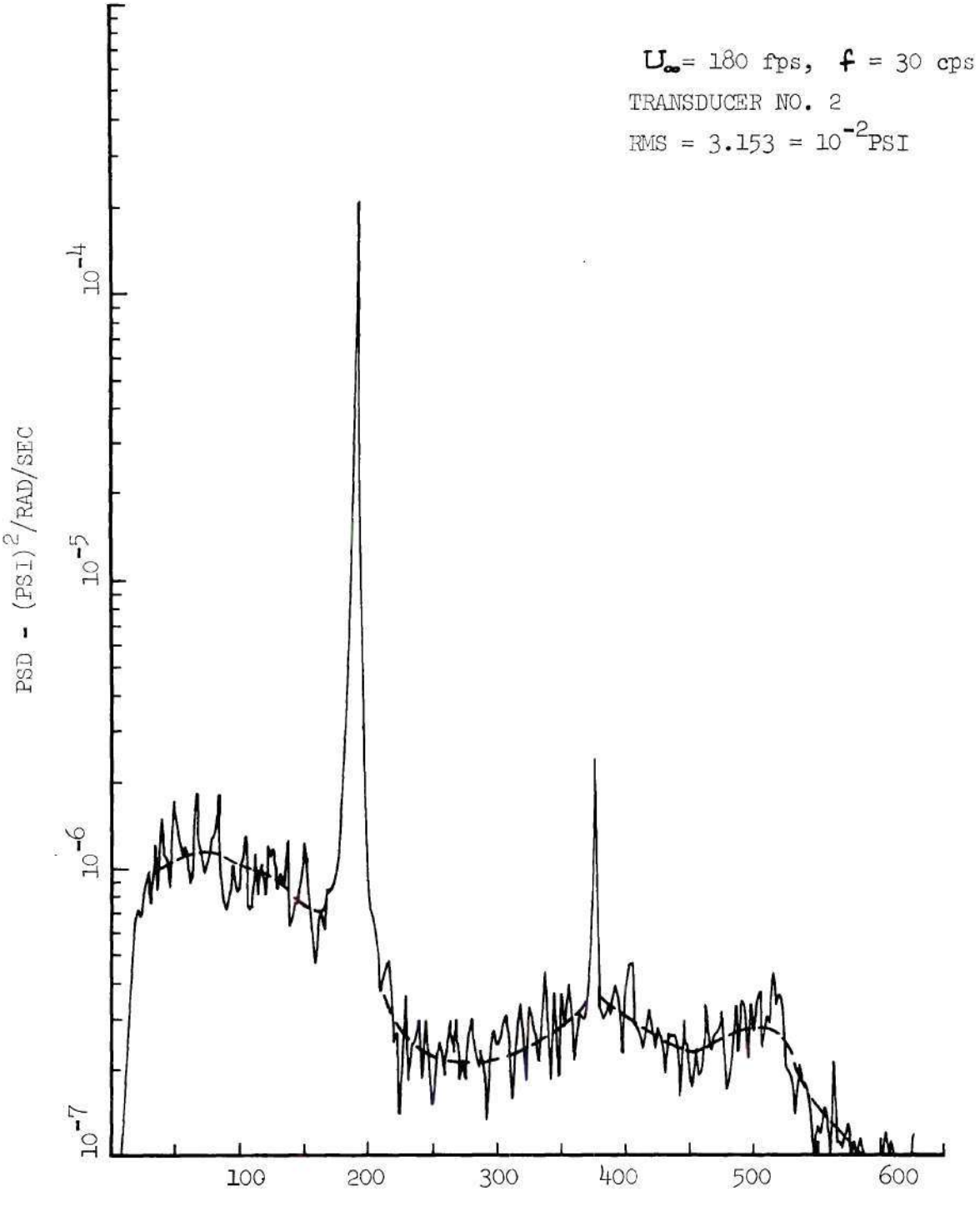

Figure 28. Sample Power Spectrum of Wake Pressure

where the frequency N, in cycles/second, is obtained from the median peak frequency as evidenced in the spectra. The spectra for the number two probe at three chordlengths downstream are used for the calculation. Table 1 presents the results for the three angles of attack and for speeds varying from 50 fps to 180 fps. Conditions for which a peak was not evident have been omitted from the table. Figures 25 and 27 are marked with an arrow to indicate the author's judgment as to the best average location of the Strouhal peak frequency. Such conditions primarily occurred at the 15° angle-of-attack position. Table 1 also presents the test Reynolds number, which was computed without correction for wind tunnel turbulence factor. R is the Reynolds number based on chordlength and R_e is the Reynolds number based on projected chord, i.e.,

$$R = \frac{U_\infty c}{\nu} \tag{72}$$

$$R_e = \frac{U_\infty c \sin \alpha_o}{\nu} \tag{73}$$

Thus R_e is comparable to a cylinder Reynolds number, as discussed previously. The Reynolds number range of the data is from 312,000 to 1,125,000. The computed values of natural Strouhal number range from .10 to .14, and generally increase with angle of attack. The values obtained here are in general agreement with the values obtained by Tyler [21], Kryzwoblocki [22], and others at comparable Reynolds numbers. The value of shedding frequency is difficult to determine exactly due to

Table 1. Computed Natural Strouhal Number from Wake Spectrum of Stationary Airfoil

α_o	U_∞	$\sin\alpha_o$	N	$R \times 10^{-5}$	$R_e \times 10^{-5}$	S_n
15.0	50	.258	19.1	3.12	.81	.10
15.0	60	.258	27.8	3.75	.97	.12
17.5	50	.300	16.0	3.12	.94	.10
17.5	60	.300	23.9	3.75	1.12	.12
17.5	80	.300	35.8	5.0	1.50	.13
17.5	100	.300	44.6	6.25	1.87	.13
17.5	140	.300	56.0	8.75	2.62	.12
17.5	180	.300	71.6	11.25	3.38	.12
20.0	60	.342	22.3	3.75	1.28	.13
20.0	100	.342	41.5	6.25	2.14	.14
20.0	140	.342	54.0	8.75	3.00	.13

Note: Average value of S_n from the above data is .12

the broadband spectral behavior. The procedure used here was to estimate the center frequency of the band visually. Figures 29, 30, and 31 present the variation of root mean square pressure coefficient with forced Strouhal number for $\alpha_o = 15°$, $17.5°$, $20°$, respectively, for the various airfoil frequencies. The root mean square pressures for transducer number one were used to generate these graphs. The objective was to show wake intensification as a function of forced Strouhal number, so that only one of the several transducers need be used for this purpose. This will become apparent from the pressure profiles to be presented. Also indicated on these figures is the average value of the Strouhal number for natural vortex shedding, as taken from Table 1.

Velocity was selected as a parameter on the graphs, for there is a consistent reduction in fluctuating pressure coefficient with increase in velocity. The fluctuating pressure as percent of freestream dynamic pressure was found in general to decrease with increasing dynamic pressure. The data show relative intensification for two Strouhal numbers, some of the curves showing a maximum in the range $S_f = .05$ to .06 and again, where the data range permitted, a maximum in the range .11 to .14. It is difficult to estimate from the available data exactly where the higher Strouhal number peak occurs. For the condition $\alpha_o = 17.5°$, the highest value of forced Strouhal number was obtained, as seen in Figure 30. For the condition $U_\infty = 50$ fps and $f = 30$ cps, a value of $S_f = .18$ resulted. It appears that the $U_\infty = 50$ fps graphs may attain a maximum between $S_f = .11$ and $S_f = .18$. In the same figure the $U_\infty = 60$ fps graph shows intensification at about $S_f = .075$, suggesting a subharmonic wake response to the fundamental Strouhal

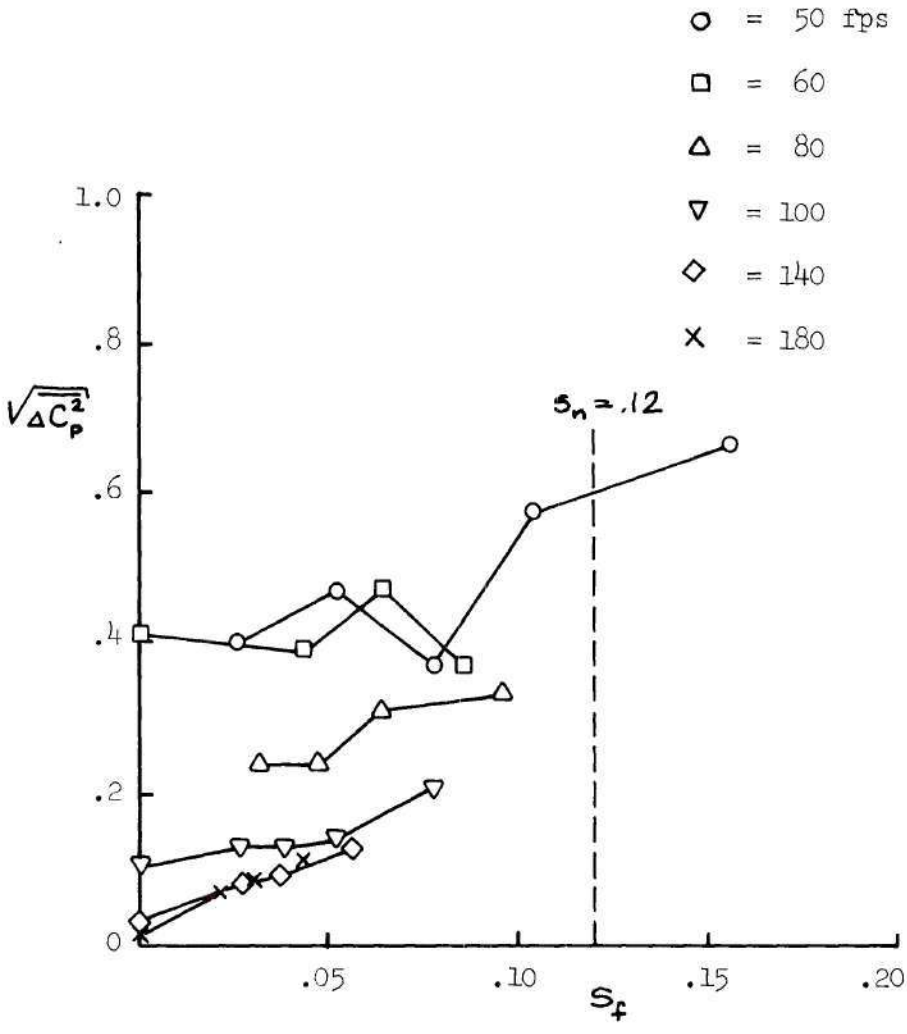

Figure 29. Root Mean Square Pressure Coefficient Versus Forced Strouhal Number, $\alpha_o = 15°$ Transducer Number One, ($\eta = 4.4$)

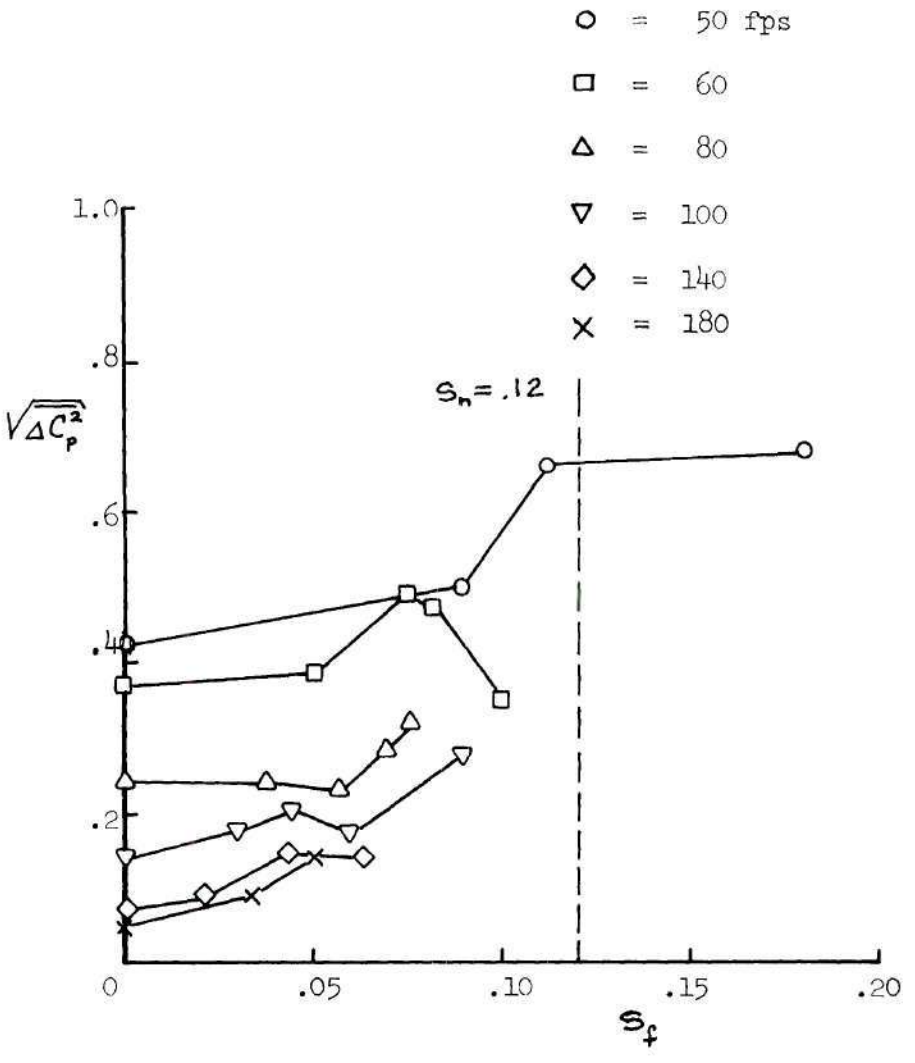

Figure 30. Root Mean Square Pressure Coefficient Versus Forced Strouhal Number, $\alpha_o = 17.5°$, Transducer Number One, ($\eta = 4.4$)

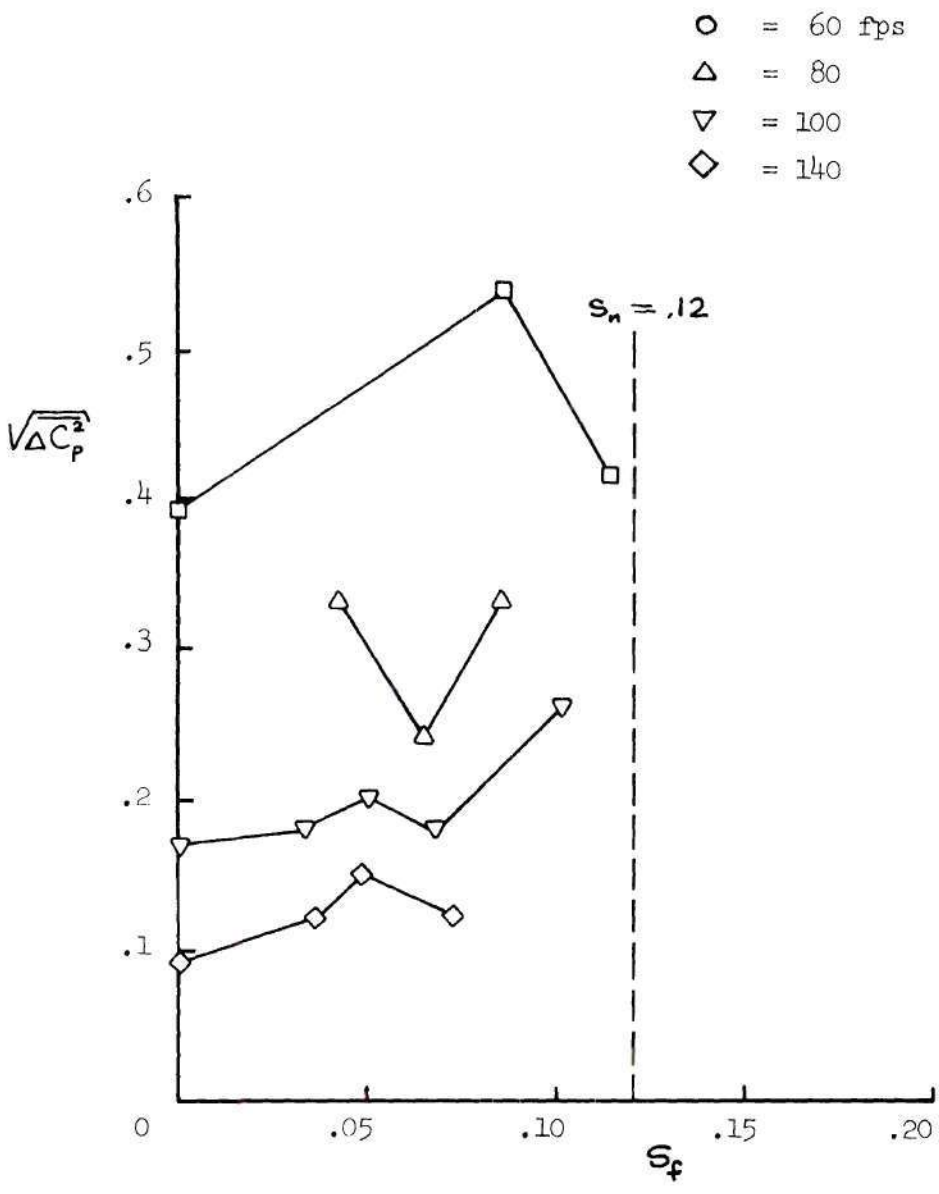

Figure 31. Root Mean Square Pressure Coefficient Versus Forced Strouhal Number, $\alpha_o = 20°$, Transducer Number One, ($\eta = 4.4$)

exciting frequency. From the available data at U_∞ = 50 fps, this could occur at a Strouhal number of about twice the above value or S_f = .15. From the average natural Strouhal number indicated on the figure, this is seen to agree reasonably well with values computed from static spectra. This observation for the one condition where airfoil oscillatory data bracketed the natural shedding range tends to verify that a significant amplification of wake fluctuation occurs under the condition of airfoil/wake resonance. The observed occurrence of the peak at about one-half the natural shedding frequency is unanticipated and apparently is a result of the highly nonlinear mechanism of natural vortex shedding coupled with the oscillatory forcing mechanism of the airfoil. It is evident that the intensification at the lower Strouhal number is not always well defined for the higher speeds. However for the $\alpha_o = 20^\circ$ condition, it can be seen that the peak is well defined at both U_∞ = 100 fps and U_∞ = 140 fps, where it occurs at S_f = .05, though the highest values of S_f attained did not reach the average value S_f = .12.

Aside from Strouhal resonance considerations, an important result to be observed is that airfoil motion of almost any frequency causes a significant increase in wake fluctuating pressure. As is evident from the power spectra, this increase occurs at discrete frequencies. It is noted that some lower frequencies tend to decrease overall wake fluctuation, particularly at the lower speeds. However the higher speeds appear to always increase fluctuating pressure with increasing frequency.

Considering the dynamic condition as represented in Figures 26

and 28, it is clear that airfoil oscillation imposes a highly discrete wake response at the same frequency as that of the airfoil. In some cases one or more higher harmonics are evident in the spectrum. The detection of the presence of the harmonics generally depends on the location of the probe and on the frequency of airfoil oscillation. An examination of the raw power spectra in Appendix C reveals that the harmonic spikes appear above 15 cps and are strongest at 30 cps.

That vortex propagation can produce the observed harmonics may be demonstrated by assuming the presence of either a single or a double row of point vortices and computing the pressure field associated with the propagation of such a pattern past a fixed point in space. Following is the development and solution of such a model.

Model for Discrete Wake Vortices

The complex potential of two rows of equidistant vortices, staggered as shown in Figure 32, is given by [15],

$$w = i\Gamma\left\{\ln \sin\frac{\pi}{a}\left(z - i\frac{b}{2}\right) - \ln \sin\frac{\pi}{a}\left(z - \frac{a}{2} + i\frac{b}{2}\right)\right\} \tag{74}$$

where b is the lateral spacing between rows, a is the longitudinal spacing, Γ is the strength of one vortex, and the coordinate system is fixed relative to the array as shown in the figure. The induced velocity components are obtained from

$$-u + iv = \frac{dw}{dz} \tag{75}$$

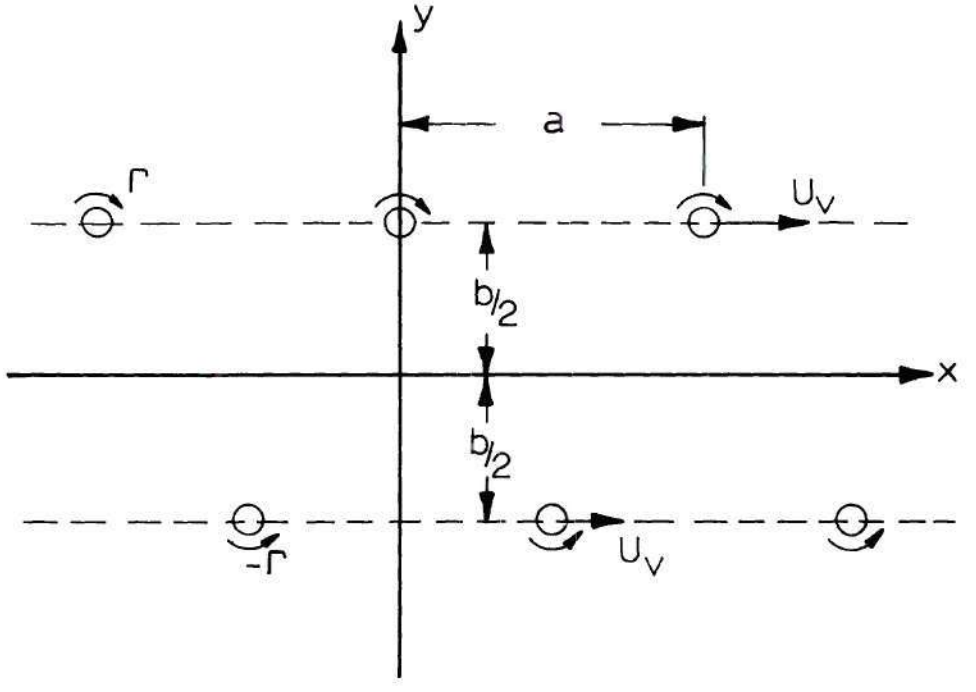

Figure 32. Vortex Wake Geometry

where u is the velocity in the x-direction and v is the velocity in the y-direction. Performing the indicated operation and simplifying, the following results are obtained for u and v in terms of the coordinates x and y,

$$u = \frac{\Gamma}{2a}\left\{\frac{\sinh\frac{\pi}{a}(2y+b)}{\cosh\frac{\pi}{a}(2y+b)+\cos\frac{2\pi x}{a}} - \frac{\sinh\frac{\pi}{a}(2y-b)}{\cosh\frac{\pi}{a}(2y-b)-\cos\frac{2\pi x}{a}}\right\} \tag{76}$$

$$v = \frac{\Gamma}{2a}\left\{\frac{\sin\frac{2\pi x}{a}}{\cosh\frac{\pi}{a}(2y+b)+\cos\frac{2\pi x}{a}} + \frac{\sin\frac{2\pi x}{a}}{\cosh\frac{\pi}{a}(2y-b)-\cos\frac{2\pi x}{a}}\right\} \tag{77}$$

Letting the array of vortices propagate in a fixed pattern downstream with the velocity U_v, the coordinate x is written as

$$x = U_v t \tag{78}$$

where t is taken equal to zero when the configuration is that shown in Figure 32. Then the pressure at a fixed point in space as a function of time is computed from

$$\Delta p(t) = \rho U_v u + \frac{1}{2}\rho(u^2+v^2) \tag{79}$$

where only the fluctuating parts of u and v are used. The above result follows directly from Bernoulli's equation, after noting that the velocity of the mean flow in the neighborhood of the wake is U_v and not U_∞. Thus $\Delta p(t)$ is strictly the time dependent part of the wake pressure.

For vertical positions not lying at $y = \pm b/2$. Equations (76) and (77) may be expanded in a Fourier series and substituted into Equation (79). This will demonstrate the harmonic nature observed in the measured spectra. However, for computational convenience, a more direct approach is used here in order to demonstrate wave form and mean square pressure distribution in the wake. An electronic analog computer was used to compute the fluctuating pressure directly from Equation (79), utilizing Equations (76) and (77). The details of the computation are given in Appendix D. Equation (79) can be written in the following form

$$\frac{\Delta p(t)}{\rho\left(\frac{\Gamma}{2a}\right)^2} = \frac{2aU_v}{\Gamma}\left(\frac{u}{\Gamma/2a}\right)^2 + \frac{1}{2}\left[\left(\frac{u}{\Gamma/2a}\right)^2 + \left(\frac{v}{\Gamma/2a}\right)^2\right] \qquad (80)$$

where the quantities $u/\Gamma/2a$ and $v/\Gamma/2a$ are functions of position only. Thus the nondimensional parameter $2aU_v/\Gamma$ measures the convective effect. When the velocity of propagation of the vortex array is large and the strength of the vortices is low, the convective effect, that is, the first term on the right in Equation (80), predominates. The effect of this parameter on the fluctuating pressure time history is depicted in Figure 33, for the position $y = 0$. The change in harmonic content as $2aU_v/\Gamma$ varies from 10.0 to 40.0 is significant as evidenced in the time histories. Figure 34 depicts the pressure time history for several transverse locations in the upper half of the wake for the case $2aU_v/\Gamma = 10$, where the wake is symmetrical. Because of computer scaling requirements, the time histories were plotted to different

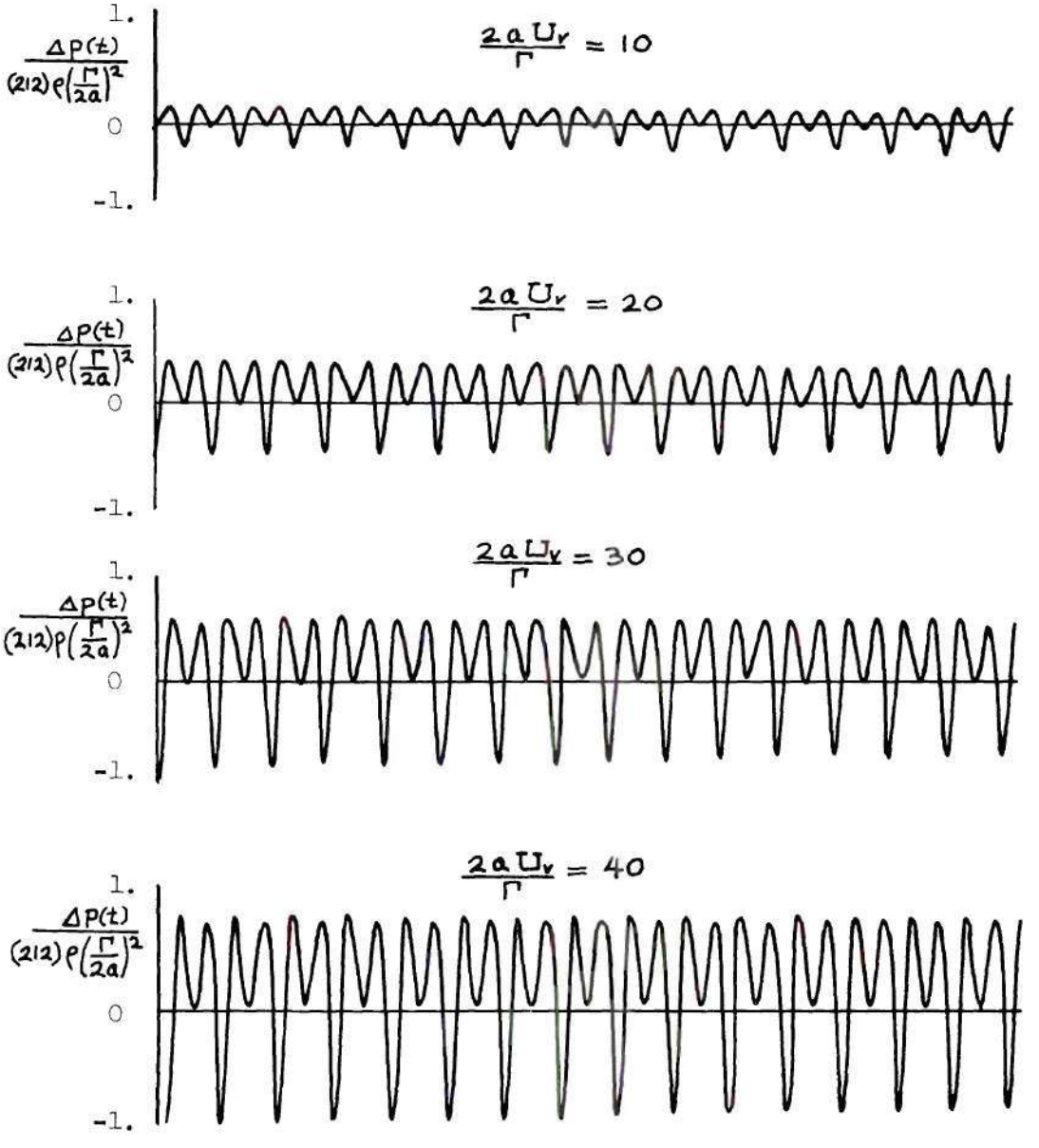

Figure 33. Effect of Convective Parameter on Pressure Time History for Vortex Array, $b/a = .30$, $\eta = 0$

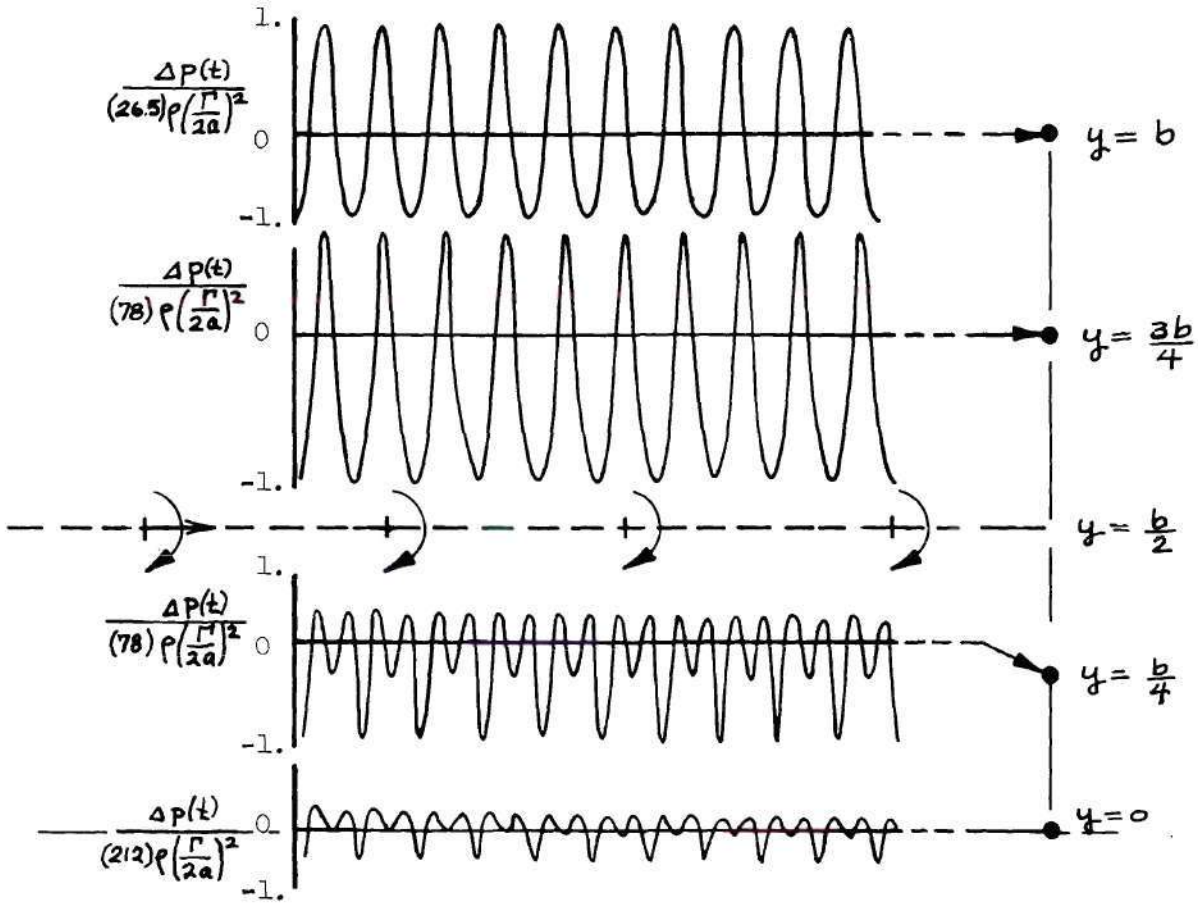

Figure 34. Pressure Time History Due to Vortex Array for Various Transverse Wake Positions, $2aU_v/\Gamma = 10$, $b/a = .30$.

scales as shown in the figure, but the change in frequency content with position is clear. Near the wake center, frequency doubling is evident, with positions further from the center containing less of the higher harmonics and approaching sinusoidal shape. For the ideal or potential vortex, the pressure must be unbounded at the positions $y = \pm b/2$. At these positions the vortex centers periodically produce infinite pressure since the velocity at the vortex center is infinite.

Comparison of Vortex Model and Experimental Results

A comparison of Figures 25 through 28 reveals that there is only slight modification of the spectrum due to airfoil motion. The fundamental and first harmonic of pressure are seen to bracket the Strouhal frequency, and there is a modification of spectral shape in that neighborhood, with a spike appearing at the Strouhal frequency. For frequencies of airfoil oscillation not near the Strouhal frequency, it can be seen from a comparison of Figures 27 and 28 that there is less change in the overall spectral shape with the spectral content of wake oscillation being contained in a very narrow frequency band centered at the frequency of airfoil motion and integral multiples of that frequency. For example, a calculation of the area contained in the spike regions to the area added over the remainder of the frequency range in passing from the static condition in Figure 27 to the oscillatory condition in Figure 28 (a measure of contribution to mean square pressure) indicates that about 98% of the area addition lies in the spike regions. This suggests a delta-function approximation for the dynamic spectrum.

An approximation of this type was suggested by Liepmann [26] for the velocity spectrum in the wake of a cylinder shedding vortices

periodically. Thus, in the present case of a pressure spectrum the relation is of the form

$$\Phi_p(\omega) = \Phi_{p_o}(\omega) + \sum_{i=1}^{n} \frac{A_i^2}{2} \delta(\omega - i\omega_1) \qquad (81)$$

where $\Phi_{p_o}(\omega)$ is the power spectrum for the static airfoil condition. A_i is the amplitude of the i^{th} harmonic, ω_1 is the frequency of the fundamental or airfoil drive frequency. The upper limit, n, on the number of harmonics will generally be small, in the present case for the three chordlength data not exceeding $n = 2$. The area under the i^{th} spike in the measured spectrum may be taken approximately equal to $A_i^2/2$. It is noted that the use of Liepmann's delta function approximation in the present investigation implies the existence of a vortex wake.

Concerning the static spectrum, $\Phi_{p_o}(\omega)$, it is noted from the test spectra that in general the spectrum decreases linearly with frequency for the higher frequencies and in particular for frequencies greater than the natural Strouhal frequency. Further, comparison of static spectra for the number two and number four transducers shows a marked difference in the roll-off rate for the two.

Figure 35 presents a comparison of spectra for the two wake locations for a typical case, $\alpha_o = 17.5°$, $U_\infty = 80$ fps. It is seen that for frequencies greater than about 350 rad./sec. the slope of both spectra is constant on the semi-log graph, with transducer number two having a more negative slope. An inspection of computer print-out of

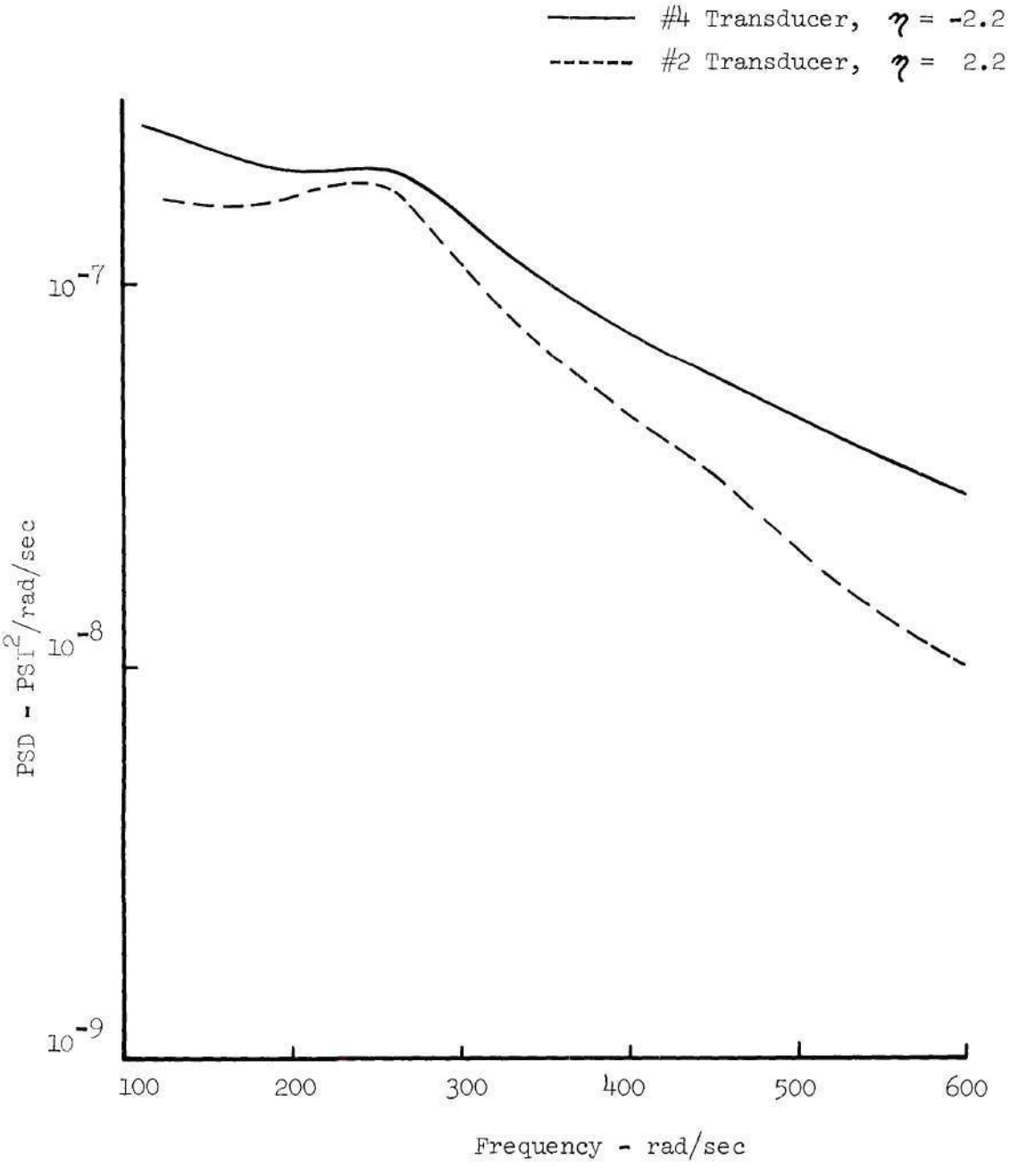

Figure 35. Comparison of Wake Pressure Spectra at η = 2.2 and η = -2.2, α_o = 17.5°, U_∞ = 80 fps, f = 0 cps

raw spectral data for the number three transducer, lying between numbers two and four, indicated that in every case the slope of the spectrum was less negative, that is, the spectrum was flatter than for either the upper or lower transducer. There appears to be no obvious answer for the observed high frequency behavior of the spectra. This is a subject which would require separate study on a statistical basis. The intent here is merely to note the observed trends of the data. In view of the approximation suggested by Equation (81) for the pressure spectrum, a procedure is suggested for determining the presence of a discrete vortex pattern by evaluating the delta-function coefficients in Equation (81) and comparing these results with those computed for a vortex array as presented in Figure 33. For this purpose it is convenient to use the root mean square pressure coefficient data as discussed and presented in the following.

Figures 36 through 51 present the measured root mean square pressure coefficients versus transverse wake position for all the test conditions. The transverse wake position is normalized by the vertical projection of the semi-chord, that is, $c/2 \sin\alpha_0$. and the resulting non-dimensional coordinate is defined as η. This coordinate measures the wake position relative to the horizontal projection of the leading and trailing edges, this assumption of wake boundary having been used in the definition of Strouhal number given in Equation (71). The coordinate η is measured positive upward with the origin centered at the airfoil mid-chord. All data are for the three chordlength wake position, and the number three transducer lies at $\eta = 0$. In nearly all cases the effect of increasing airfoil pitch frequency is to increase

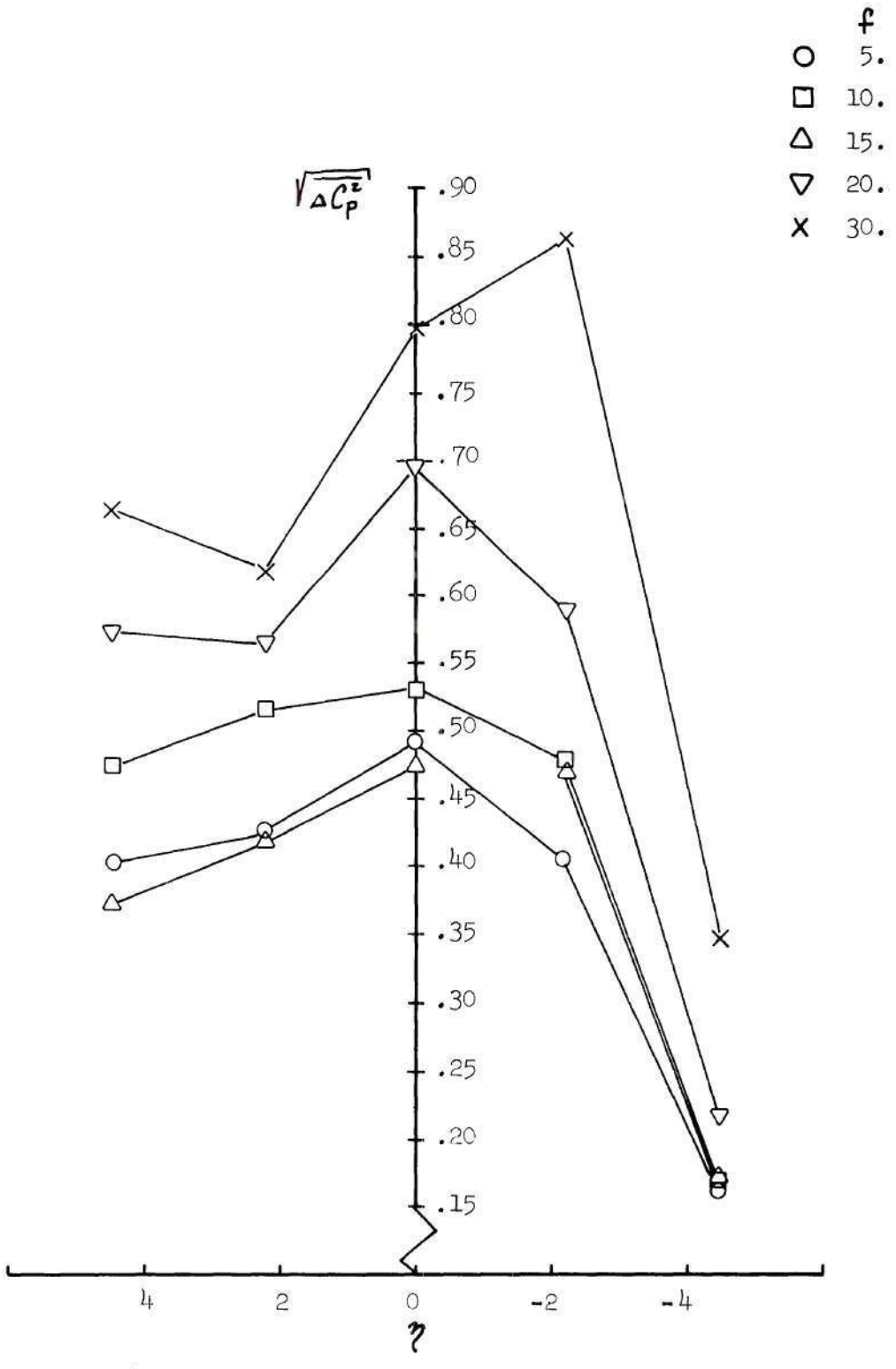

Figure 36. Root Mean Square Pressure Coefficient Versus η, $\alpha_o = 15.°$, $U_\infty = 50$ fps

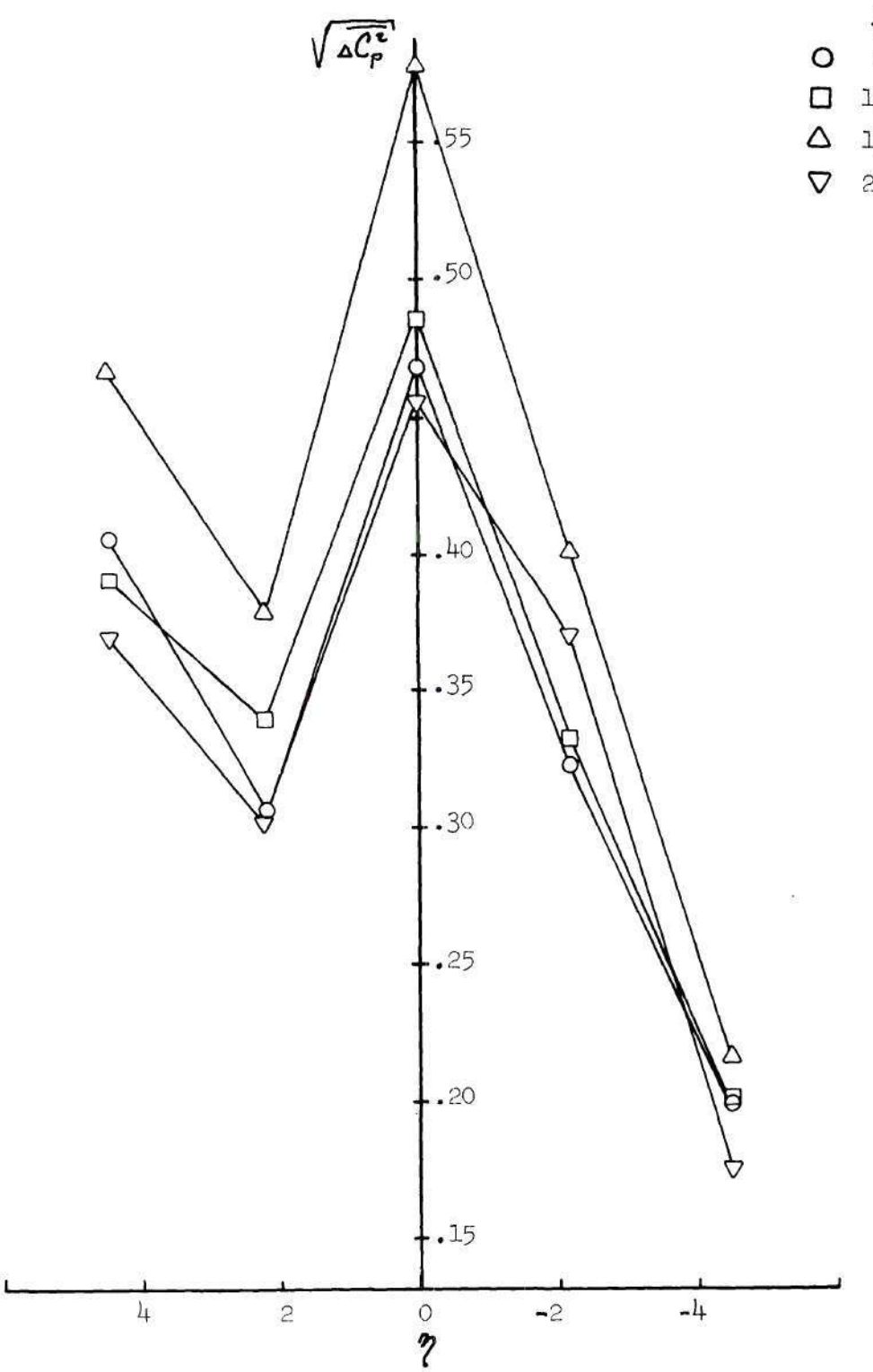

Figure 37. Root Mean Square Pressure Coefficient Versus η, $\alpha_o = 15.°$, $U_\infty = 60$ fps

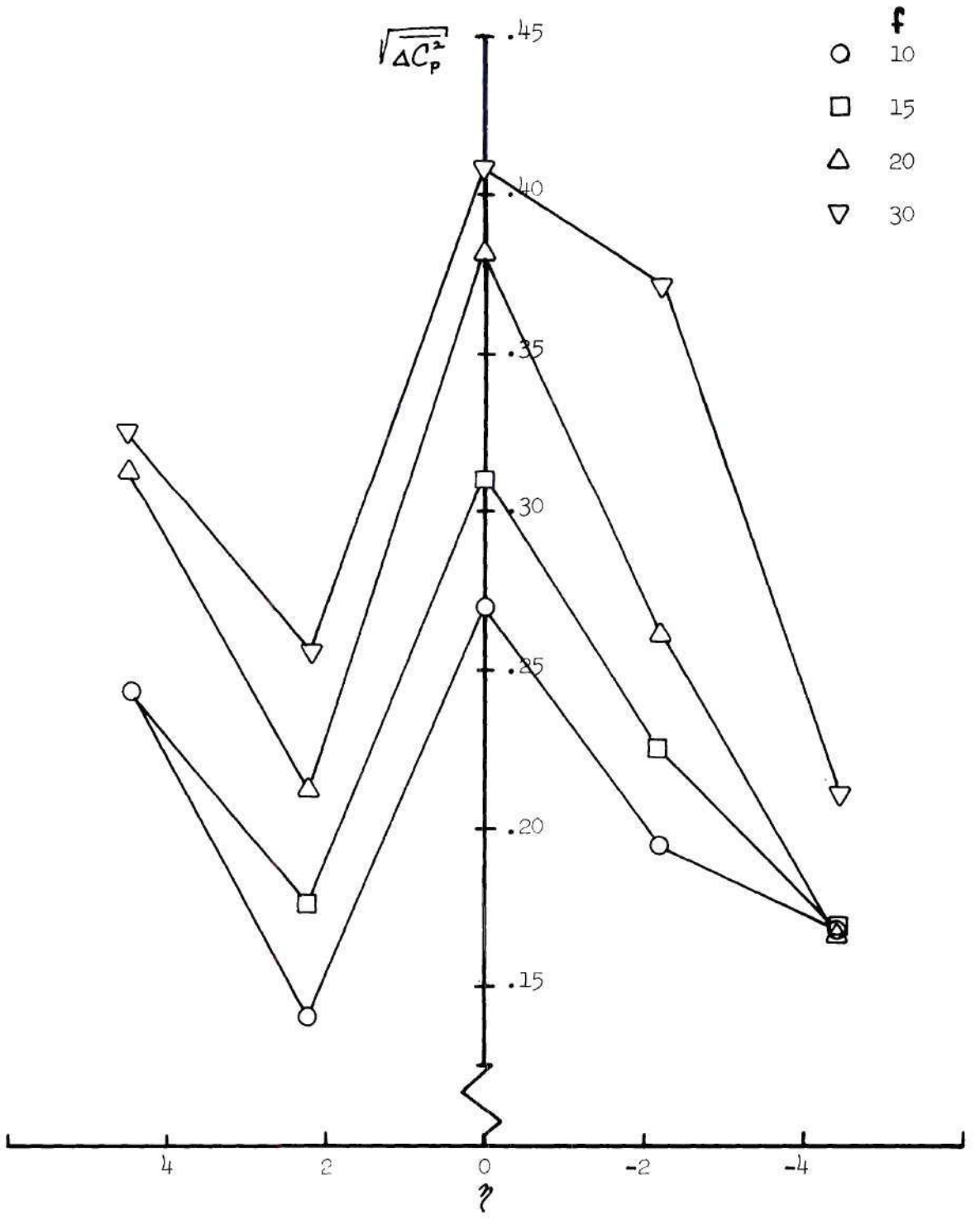

Figure 38. Root Mean Square Pressure Coefficient Versus η, $\alpha_o = 15.^\circ$, $U_\infty = 80$ fps

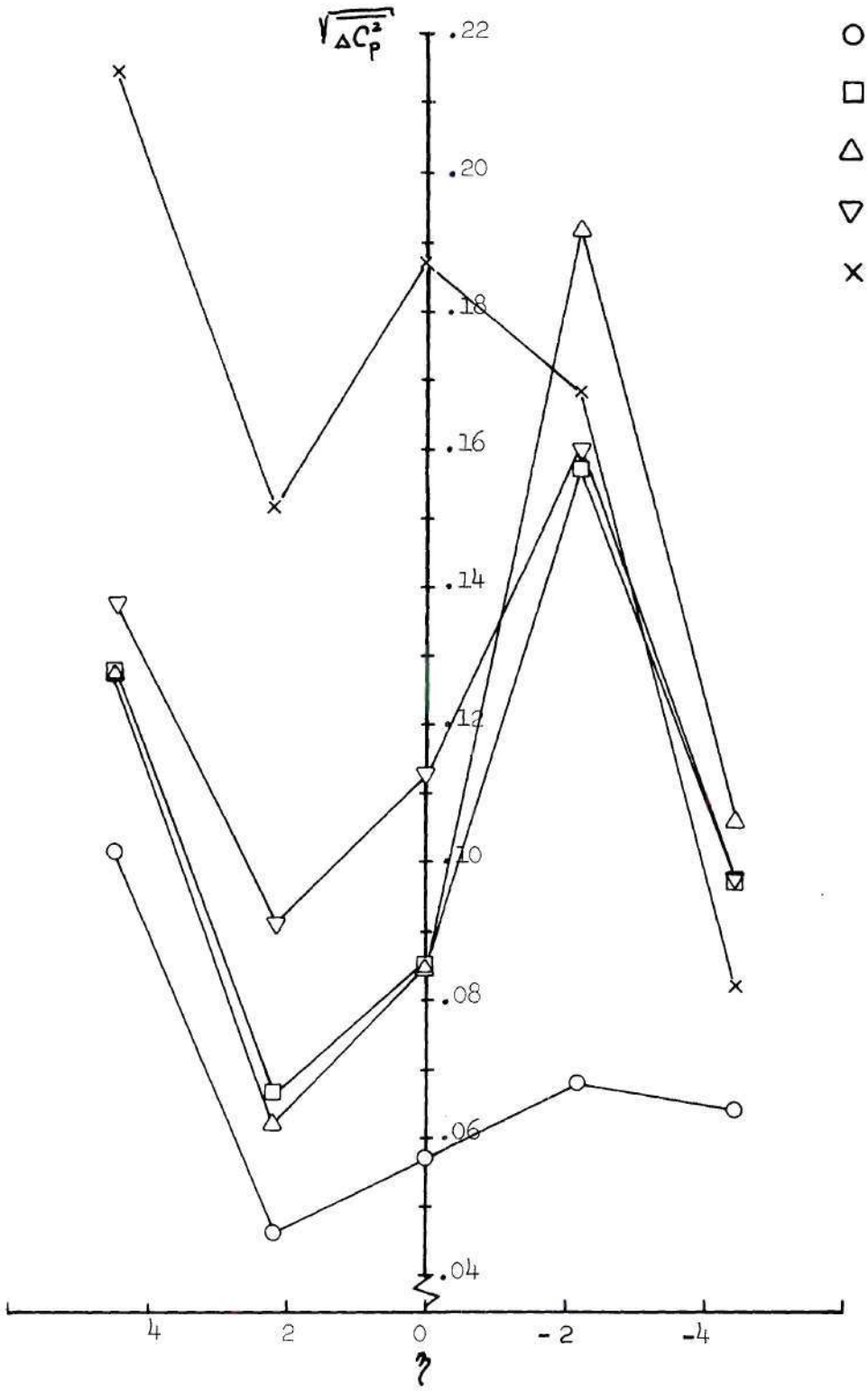

Figure 39. Root Mean Square Pressure Coefficient Versus η, $\alpha_o = 15.^\circ$, $U_\infty = 100$ fps

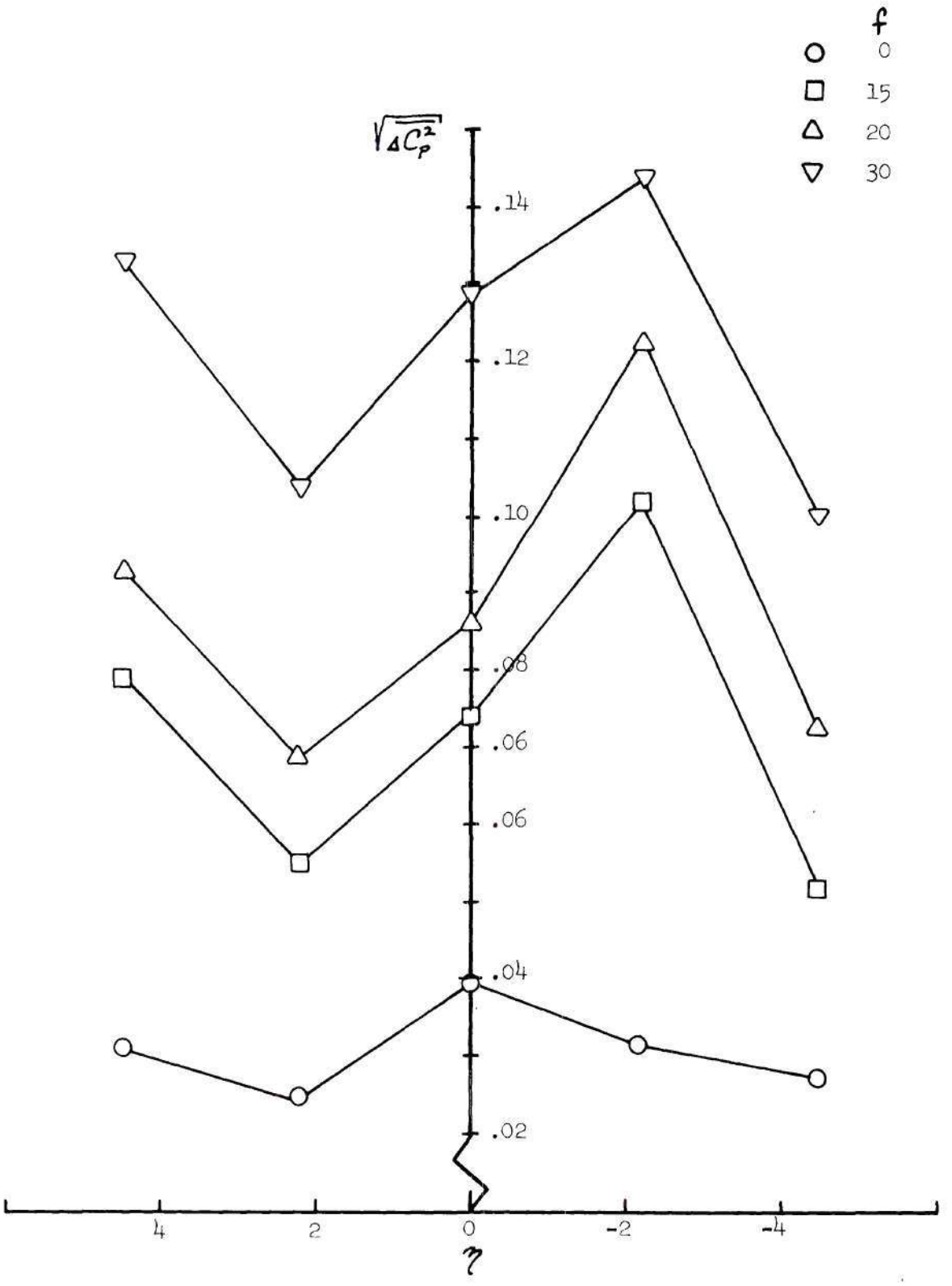

Figure 40. Root Mean Square Pressure Coefficient Versus η, $\alpha_o = 15.^\circ$, $U_\infty = 140$ fps

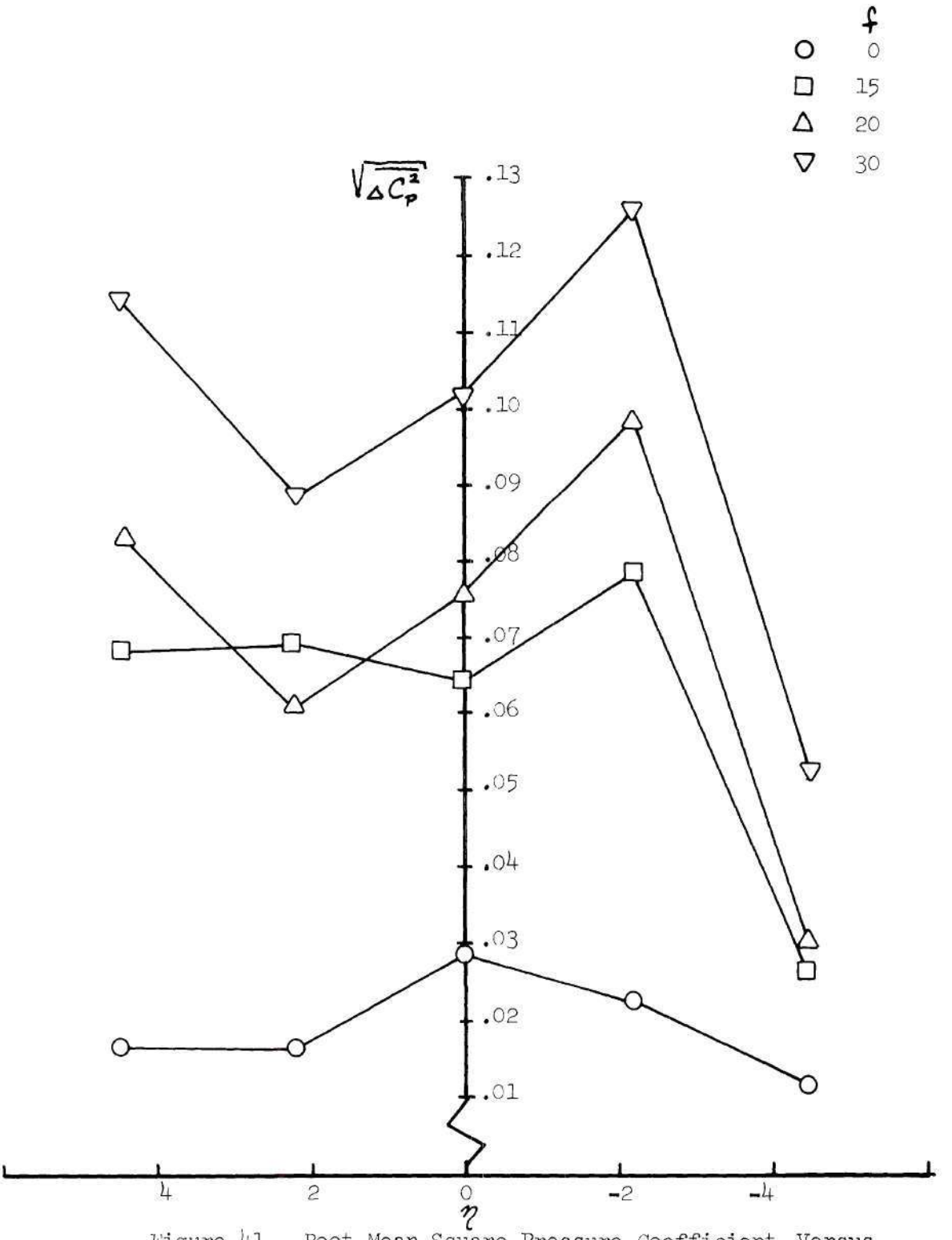

Figure 41. Root Mean Square Pressure Coefficient Versus η, $\alpha_o = 15.^\circ$, $U_\infty = 180$ fps

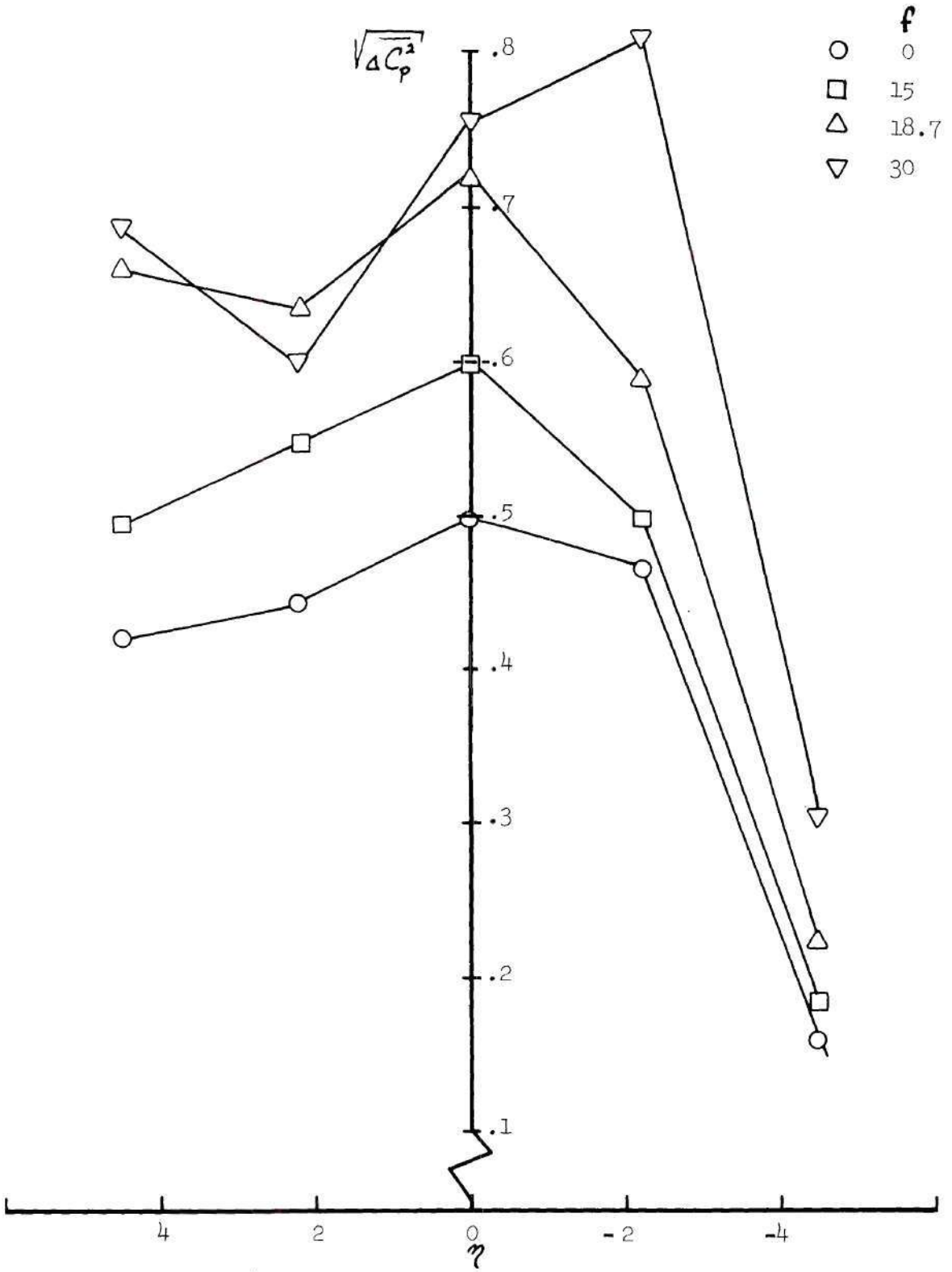

Figure 42. Root Mean Square Pressure Coefficient Versus η, $\alpha_o = 17.5°$, $U_\infty = 50$ fps

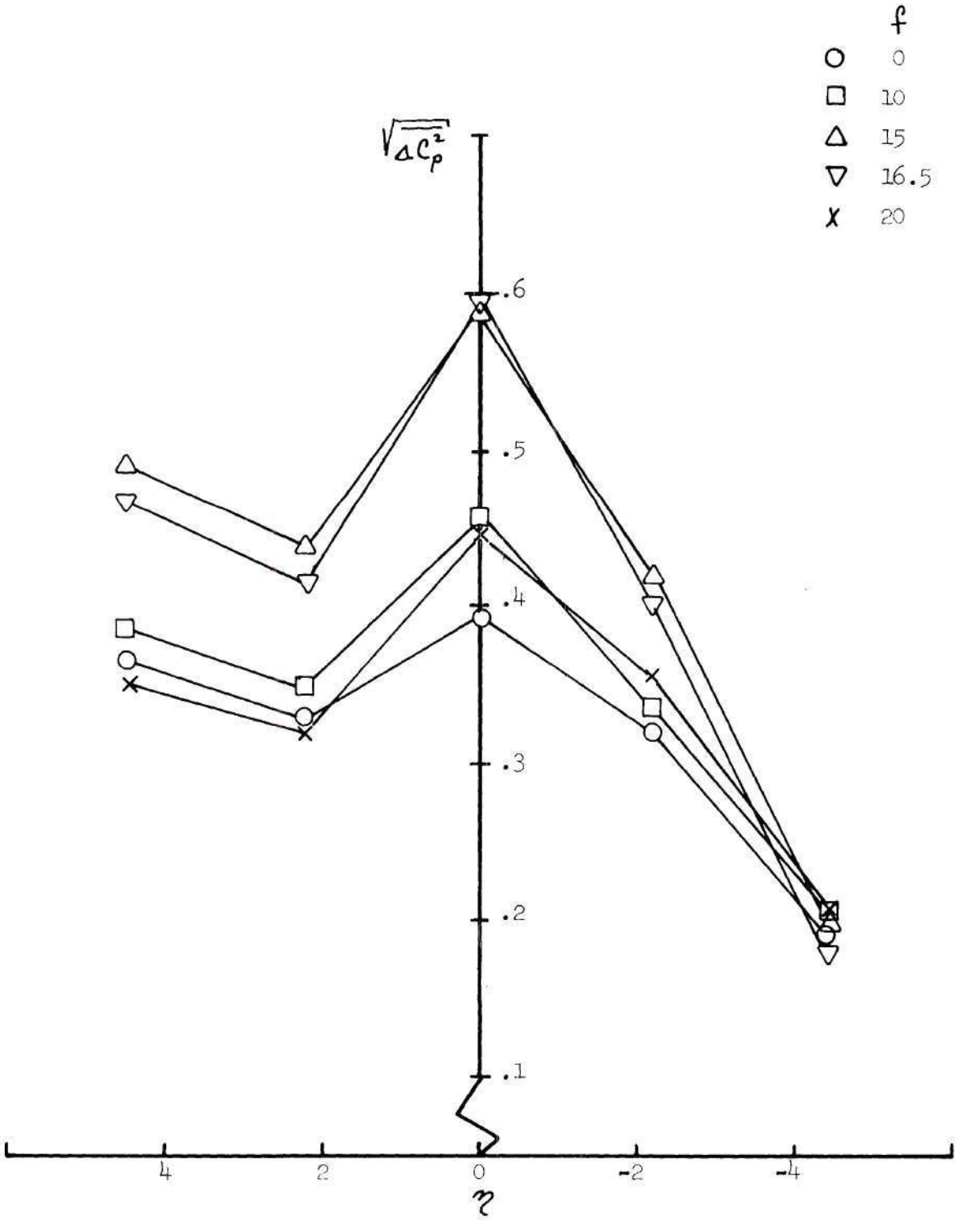

Figure 43. Root Mean Square Pressure Coefficient Versus η, $\alpha_o = 17.5°$, $U_\infty = 60$ fps

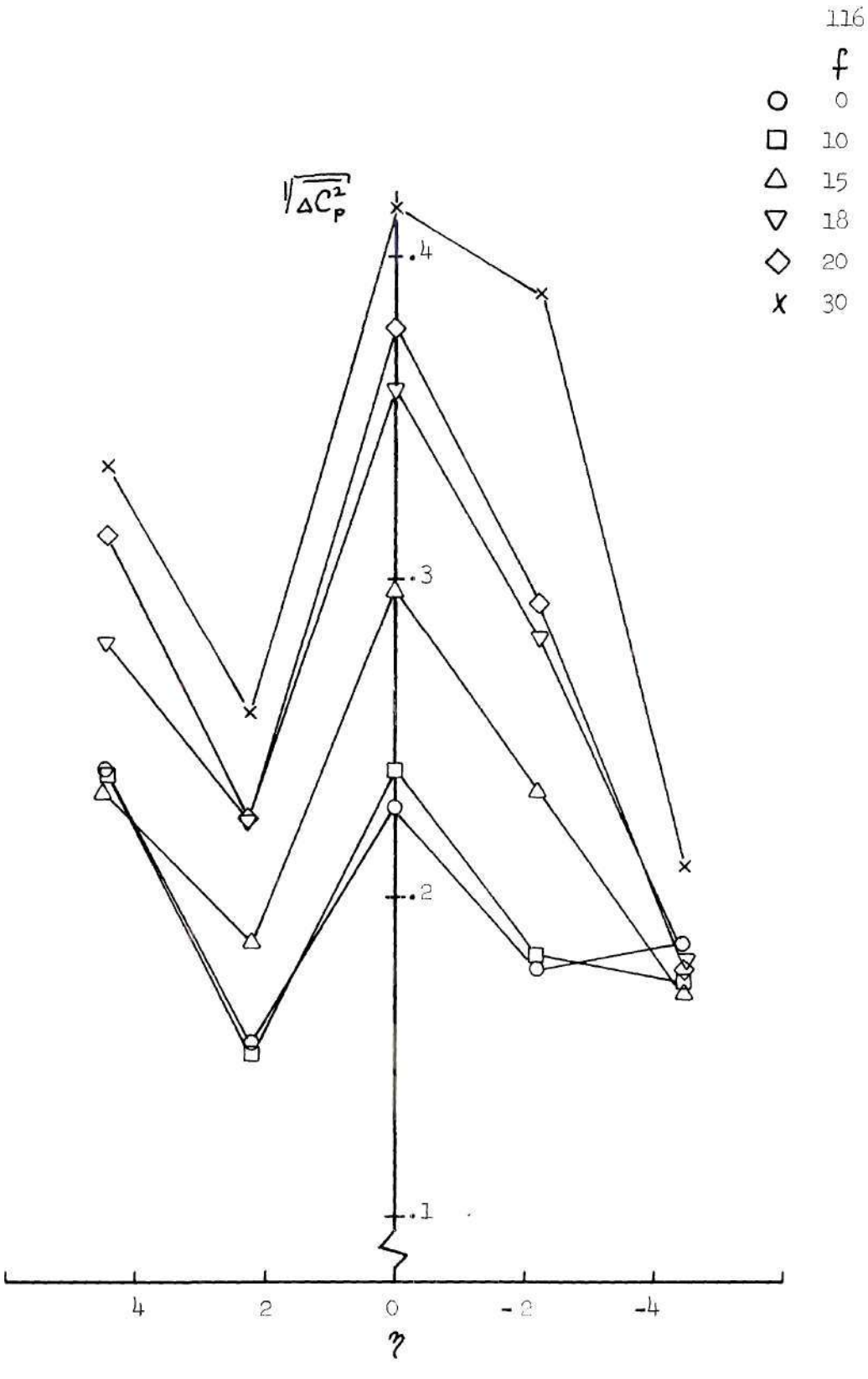

Figure 44. Root Mean Square Pressure Coefficient Versus η, $\alpha_o = 17.5°$, $U_\infty = 80$ fps

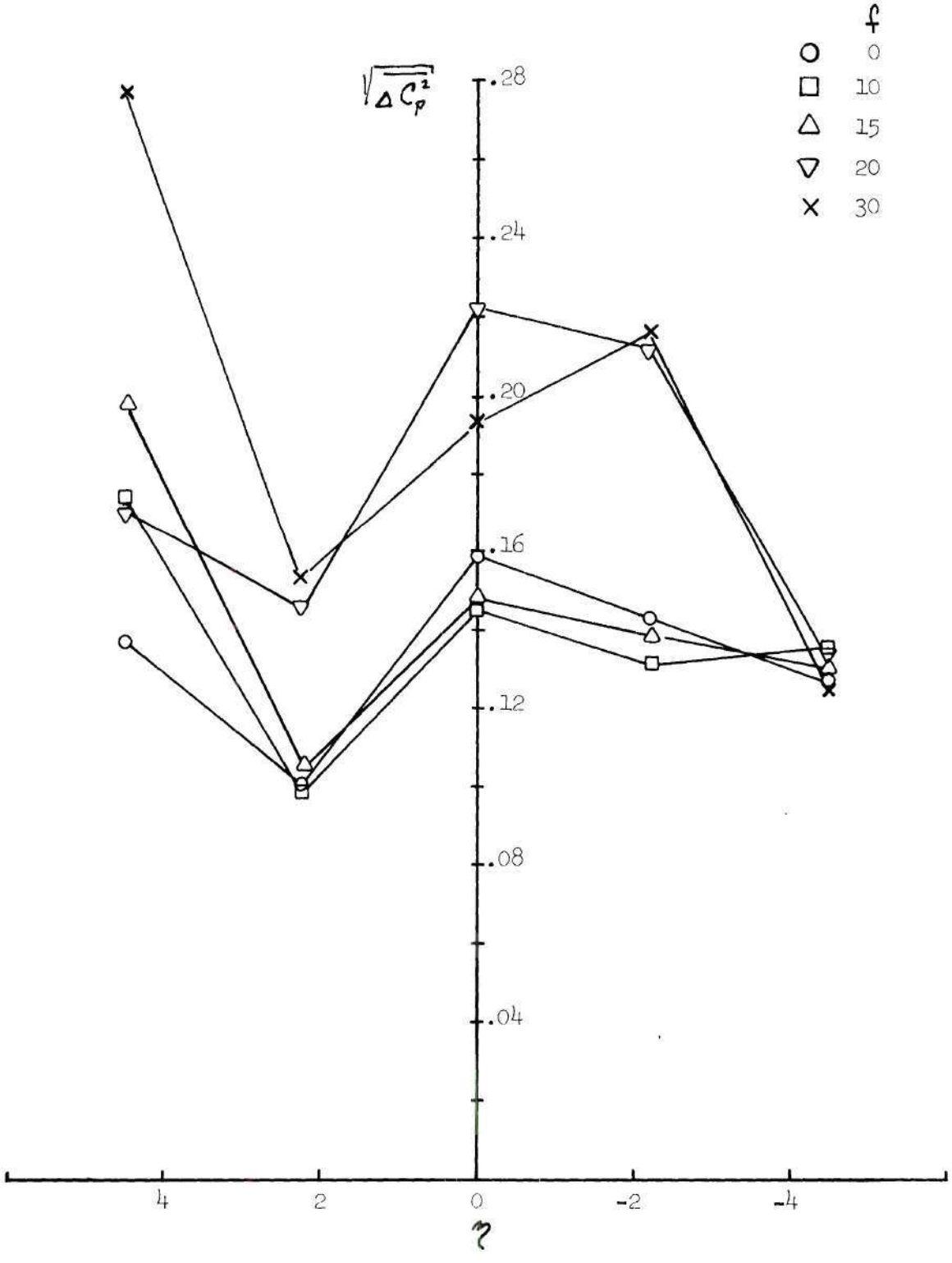

Figure 45. Root Mean Square Pressure Coefficient Versus η, $\alpha_o = 17.5°$, $U_\infty = 100$ fps

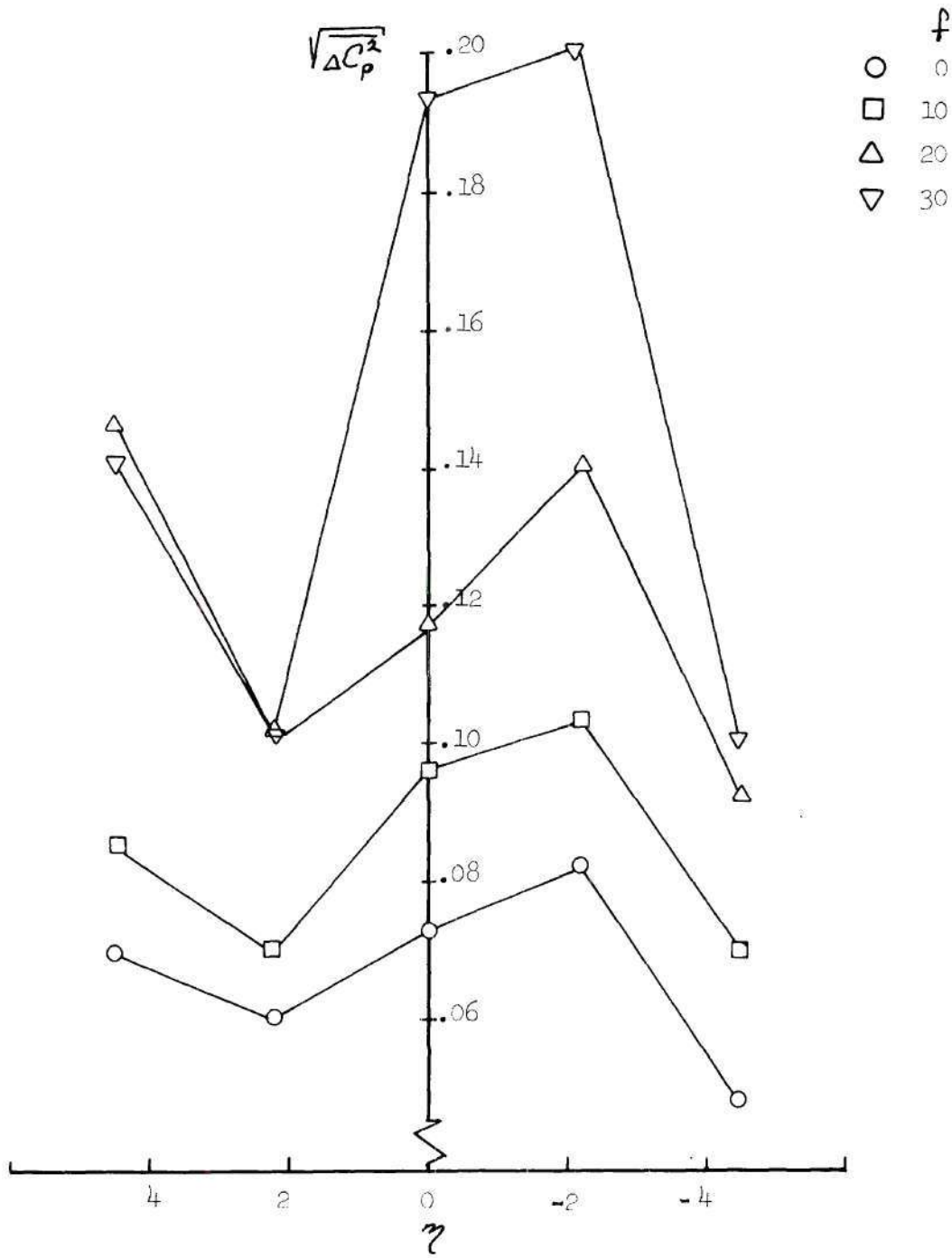

Figure 46. Root Mean Square Pressure Coefficient Versus η, $\alpha_o = 17.5°$, U_∞ = 140 fps

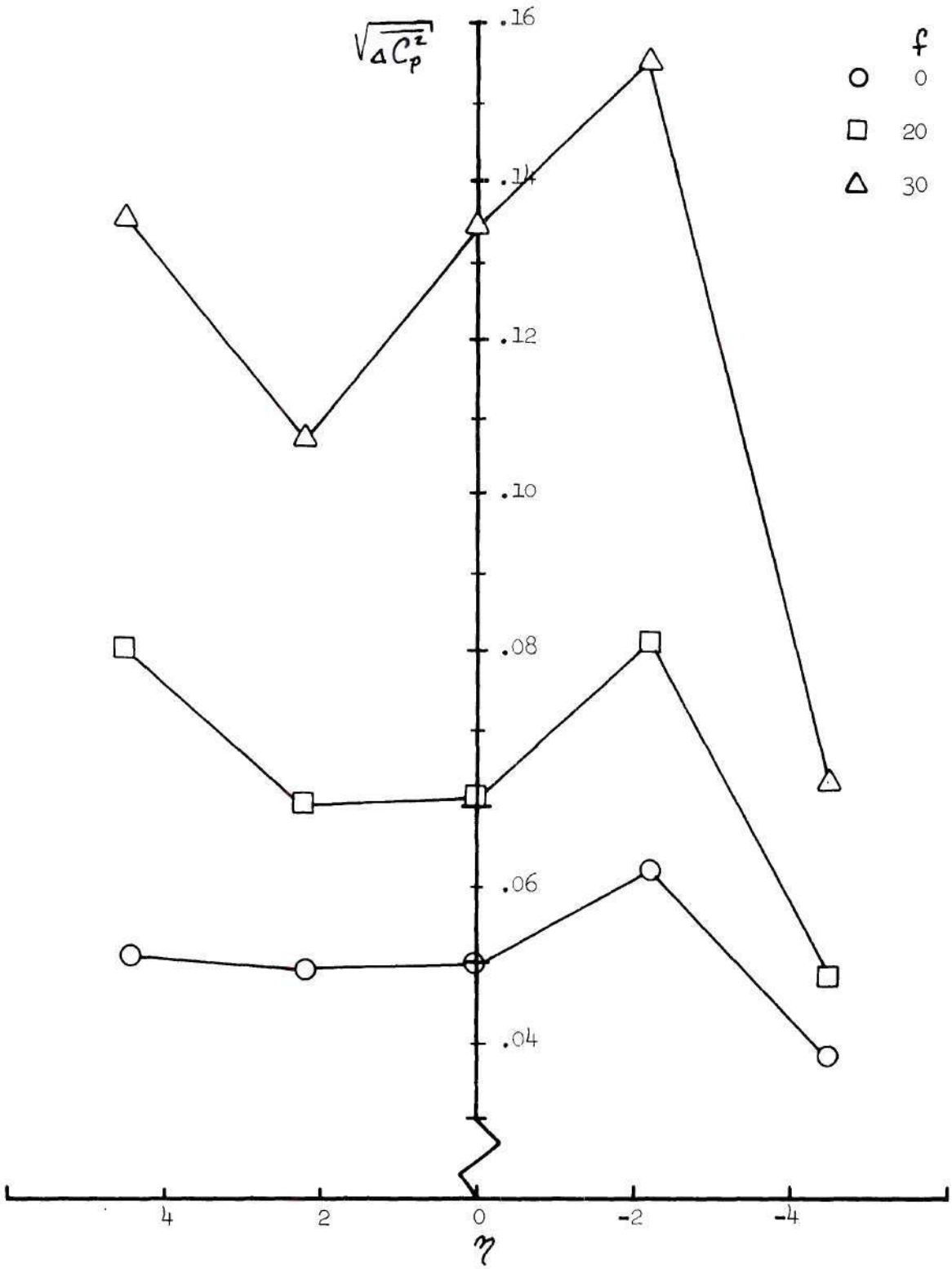

Figure 47. Root Mean Square Pressure Coefficient Versus η, $\alpha_o = 20.°$, $U_\infty = 60$ fps

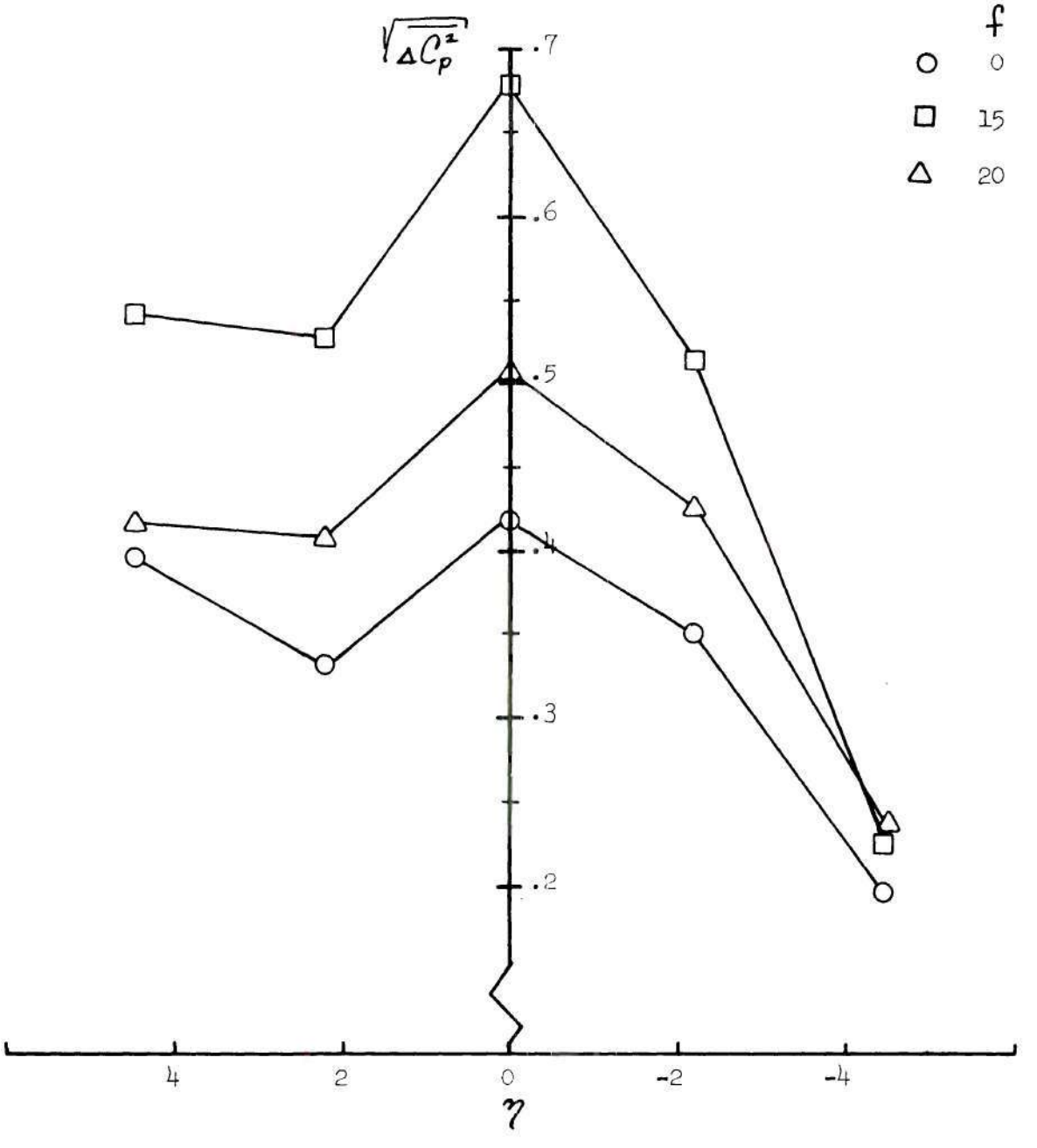

Figure 48. Root Mean Square Pressure Coefficient Versus η, $\alpha_o = 20.^\circ$, $U_\infty = 60$ fps

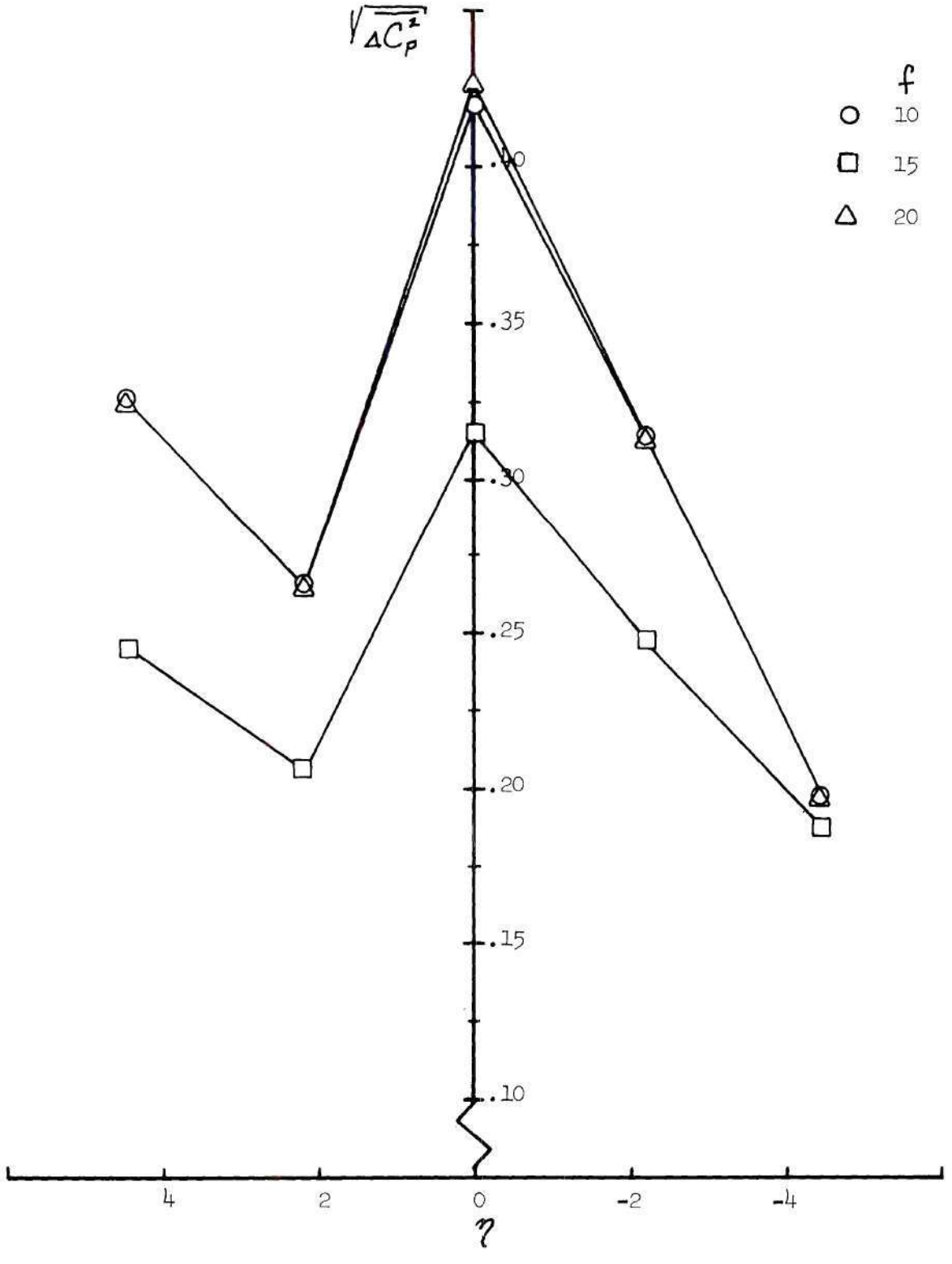

Figure 49. Root Mean Square Pressure Coefficient Versus η, $\alpha_o = 20.°$, $U_\infty = 80$ fps

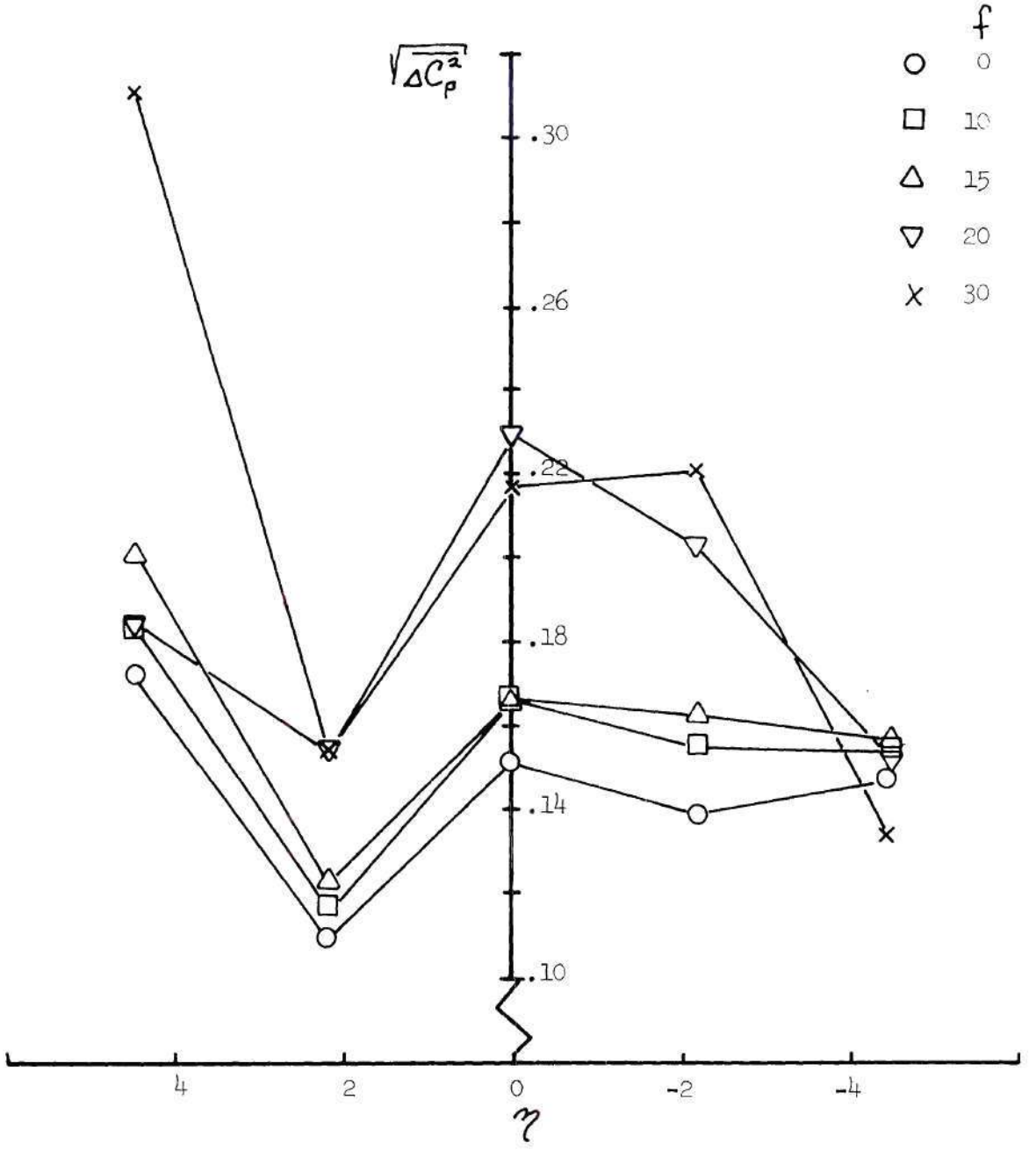

Figure 50. Root Mean Square Pressure Coefficient Versus η, $\alpha_o = 20.^\circ$, $U_\infty = 100$ fps

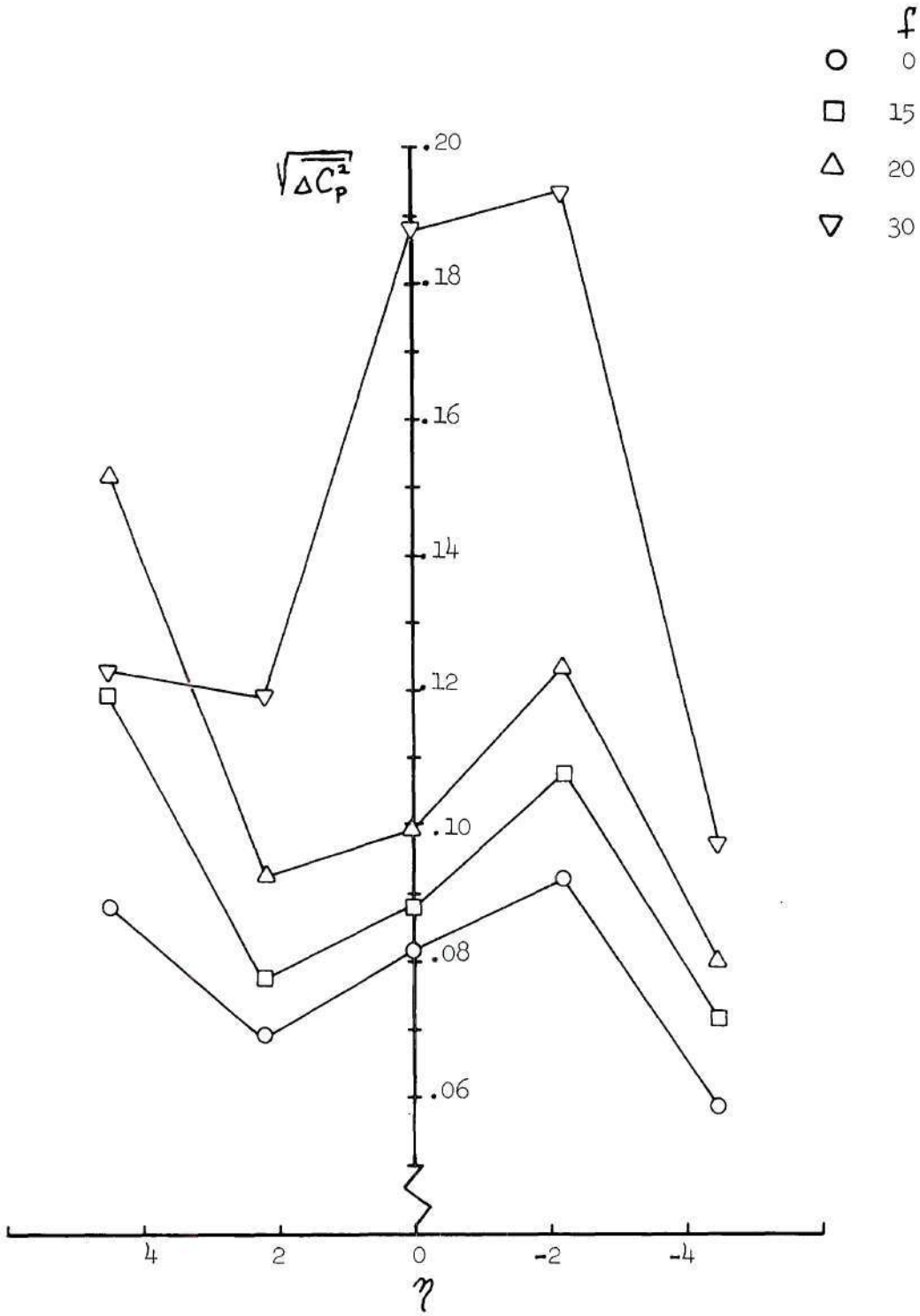

Figure 51. Root Mean Square Pressure Coefficient Versus η, $\alpha_o = 20.^\circ$, $U_\infty = 140$ fps

the overall magnitudes of the profiles. In some instances, however, it is seen that the lower frequencies, particularly f = 10 cps, tend to attenuate the overall wake response relative to the static condition. This observation was noted earlier relative to the discussion of the response at the number one transducer. A comparison of all the profiles make it clear that very significant alterations in profile shape occur as angle of attack, speed, and frequency are varied. In general, however, a characteristic common to all the profiles is the high intensity at or slightly below the projected mid-chord location in the wake, and at the extreme upper side of the wake. The number five transducer (on the lower side of the wake) measurements are in all cases relatively insensitive to airfoil frequency, and the magnitude of fluctuating pressure is consistently lower than at higher positions. Thus it appears that the lower boundary of the wake is above this position. However, for the upper side of the wake it is clear that the number one transducer does not define the extent of the wake. Here, it was found in nearly all cases that pressure increases in moving upward from number two to the number one position.

It is of interest to note the wake structure for the conditions of relative intensification of pressure coefficient (with variation in forced Strouhal number) as shown by Figures 29, 30, and 31. In particular, the condition U_∞ = 50 fps, α_o = 17.5°, shown in Figure 30, indicates a large increase in fluctuating pressure for values of forced Strouhal number well into the range of natural shedding. Referring to the two points at S_f = .11 and S_f = .18, the frequencies are respectively f = 18.7 cps and f = 30 cps, and the wake profiles for these

conditions are shown in Figure 42. By comparison with other test conditions it is apparent that these profiles are of the same general shape as those of the same frequency range but different speed and angle-of-attack conditions. Thus the wake structure, at least in terms of rms pressure, shows similarities for conditions both near and far removed from Strouhal resonance. However it is evident that if a well-defined vortex array is to exist for any of the test conditions, it will most likely exist for the condition nearest the natural Strouhal frequency. Therefore the condition f = 18.7 cps, shown in Figure 42, is chosen for comparison with the analog computer results for a convected vortex array.

In view of the coherency of the wake disturbance due to the airfoil motion it will be assumed that formation of a well-defined array of vortices in the wake exists due to the imposed motion. Then the resulting root mean square pressure follows from equation (81 by taking the difference in the values of the spectra for the static and oscillating airfoil conditions. This procedure appears reasonable for the particular case in question, since there is very little modification of the overall spectrum due to airfoil motion, and the added power is confined to a very narrow frequency band. Referring to Figure 42, for the position ζ = 0, which is assumed to be near the center of the wake, the value of $\sqrt{\Delta C_p^2}$ is .72, from which the mean square pressure is found to be

$$\sqrt{\overline{\Delta p^2}} = .0046 \text{ psi} \tag{82}$$

and the corresponding average peak-to-peak pressure is,

$$\Delta p = 2\sqrt{2}\sqrt{\overline{\Delta p^2}} = .013 \text{ psi} \tag{83}$$

To obtain pressure magnitude from the theoretical results represented in Figure 33, it is necessary to assume a value of $2\pi U_v/\Gamma$ and a value of either πU_v or $\Gamma/2\pi$. One further parameter is the spacing ratio of the vortex array, b/a. This value has been taken equal to .30, which is nominally measured for stable vortex streets downstream of a cylinder, as discussed previously. Similarly, a reasonable estimate of convective velocity will be taken as $.8U_\infty$.

Table 2 presents computations of several wake parameters for a range of values of $2\pi U_v/\Gamma$ as taken from Figure 33. The quantity is peak-to-peak pressure, and it is seen that $2\pi U_v/\Gamma = 20$ gives the best approximation to the experimental value of $\Delta p = .013$ psi. To compute the value of Γ it is first necessary to determine the vortex spacing, a. If the vortex array is assumed stable and is steadily convected at three chordlengths downstream, the distance between successive vortices on one side of the wake is

$$a = \frac{U_v}{f} \tag{84}$$

where f is the frequency of airfoil oscillation. For the present example this expression gives the value $a = 2.14$ ft. Using $b/a = .30$ gives $b = .642$ ft. In terms of the wake width parameter η, the increment between vortex rows is $\Delta\eta = 4.3$. Referring to Figure 42,

Table 2. Effect of Vortex Convective Parameter on Computed Wake Characteristics

	$2aU_v/\Gamma$			
	10	20	30	40
$\Gamma/2a$	4.00	2.00	1.33	1.00
$\frac{\Delta P}{\rho(\Gamma/2a)^2}$	84.8	191.0	296.0	403.0
ΔP	.0230	.0130	.0087	.0067
Γ	17.2	8.6	5.7	4.3
ΔC_l	.68	.34	.23	.17

Note: U_v = 40 fps

this value is seen to be reasonable if it is assumed that the two rows of vortices lie respectively between $\eta = 2$ and $\eta = 4$ and between $\eta = -2$, $\eta = 0$. The quantity ΔC_l is found using the Kutta-Joukowski relation which in terms of lift coefficient is (for chordlength of unity)

$$\Delta C_l = \frac{2\Gamma}{U_\infty} \tag{85}$$

and ΔC_l may be interpreted as the depth of the hysteresis loop in the C_l versus α curve, and Γ the corresponding circulation given up or gained by the airfoil. If it is assumed that this circulation is carried into the vortex wake as the strength of the alternating vortices in a stable wake, with no cancellation of vorticity occurring, as seen from Table 2 for the case $2\alpha U_v/\Gamma = 20$, the value $\Gamma = 8.6$ ft/^{2}/sec. implies an airfoil ΔC_l of .34. This value is generally less than experimental values obtained by Liiva and Davenport for comparable frequency and mean angle of attack, but considerably greater speed (see Figure 1 and [5]). A major difference in the present experiments and those of Liiva, Davenport, et al. is that the oscillatory angle is much different, being 1.5° half amplitude in the present case and about 5° half amplitude for the tests in Reference (5). If it is assumed that the vortex strength is proportional to airfoil oscillatory amplitude, then the value .34 for ΔC_l at ± 1.5° corresponds to a value of 1.13 at ± 5°, which from Figure 1 is seen to be a better approximation to the

depth of the hysteresis loop.

The representation of the unsteady downstream wake used here is idealized as a double row of vortices extending to infinity both upstream and downstream. This means that the behavior of the wake development between the airfoil and a position far downstream where the stable vortex structure is presumed to exist has not been accounted for. The number of parameters occurring in the example just discussed emphasizes the lack of comprehensive experimental study of the dynamic wake as well as the magnitude of the analytical difficulties in describing the phenomenon.

From the experimental results obtained here, it is evident that significant wake amplification due to airfoil oscillation occurs in most cases rather than for a few cases as would be consistent with the assumption of Strouhal harmonic or subharmonic resonance. In view of the analytical findings of this study, it would appear reasonable to assume that strong, discrete vortices are generated by the airfoil for most dynamic fully stalled conditions, and the implication of the present limited experimental results is that these vortices persist well downstream of the generating airfoil. It is noted that the test condition chosen for comparison with the results of Table 2 provided the most reasonable comparison from among all conditions tested. This appears to result from using the von Karman stability argument as a basis for comparison which, because of Equation (84), leads to unreasonable estimates of wake geometry when applied to many other test conditions. The question of the development of the wake structure as a function of downstream position, as well as the prediction of wake

vortex strength, remains unanswered.

The von Karman vortex street should be regarded merely as the least unstable configuration of vortices formed in two rows [34]. The configuration is stable under first order disturbances of a particular type, in which one vortex in the array is slightly displaced along the trajectory of its row [15]. Goldstein [34] alludes to the nature of the breakdown of such a vortex array whenever the spacing is not stable. Thus if the spacing ratio b/a is not equal to .281, the array will be exponentially unstable in time, with the arry either closing up or opening out, as sketched in Figure 52. This is an interesting point that might bear further theoretical study, inasmuch as the present experimental results indicate that discrete vortices may be forced into the wake at spacing ratios not near the stable value. This has not been a point of interest in the past since the study of vortex wakes has been confined primarily to the condition of natural shedding, that is, when the body producing the vortices is static. Perhaps the most important point to be considered is the mechanism whereby the body motion induces the formation of strong discrete vortices. As discussed previously, the method of Ericsson [6, 7] can be used to account for dynamic stall delay and thus account for roughly the upper half of the lift hysteresis loop. However this argument is not valid for conditions of full stall, where it is possible to obtain hysteresis amplitudes of the same order. It is necessary ultimately to consider the boundary layer in order to predict the magnitude of shed circulation. As pointed out by Moore [12], unsteady boundary layer effects alone do not account for observed behavior. The phenomenological model presented in the

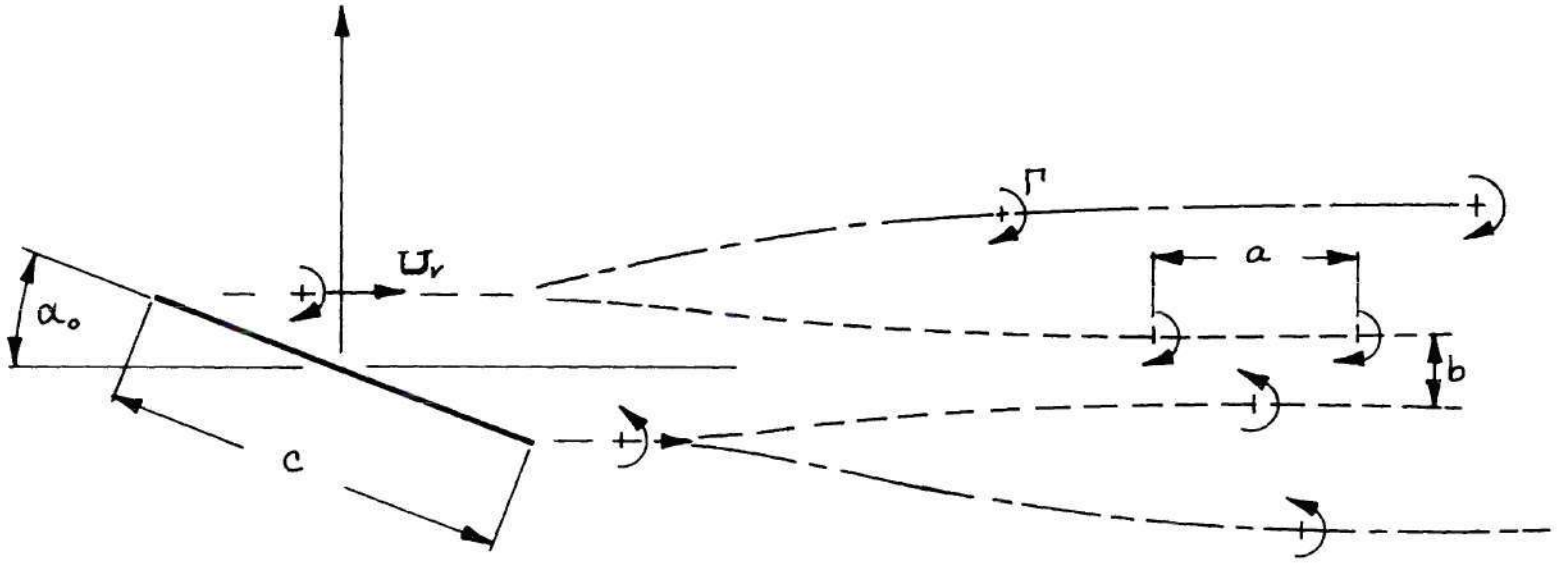

Figure 52. Possible Wake Vortex Trajectories

present study describes the overall airfoil response reasonably well but requires empirical inputs from experimental data. Because of the simple analytical form, however, it may offer promise for an analytical model to be coupled with boundary layer analysis, say of the form given by Moore, which could ultimately lead to a deterministic treatment of airfoil stall aerodynamics.

CHAPTER IV

CONCLUSIONS AND RECOMMENDATIONS

Conclusions resulting from the research presented here, and recommendations for future extension of both the theoretical and experimental results are as follows.

Conclusions

1. An analytical model for the stall dynamics of an airfoil based on the conservation of circulation has been developed. An equivalent potential flow concept was used to systematically account for loss of lift in steady stall. The model demonstrates the experimentally observed sudden loss of leading edge suction and the development of multiple-loop pitching moment versus angle-of-attack trajectories that can accompany dynamic stall.

2. The analytical model predicts that decreasing vortex propagation velocity in the neighborhood of the airfoil chord tends to be destabilizing in pitch. In addition, vortex shedding phase is a controlling factor in establishing positive or negative pitch damping. The differential pressure distribution predicted by the analytical model agrees with observed behavior, and the apparent recovery of trailing edge pressure is due to the presence of wake vorticity.

3. Measurements of unsteady pressure in the wake of a stalled airfoil, at positions three chordlengths downstream from the airfoil

trailing edge, indicated that a natural vortex shedding frequency was present for most test conditions, although not well defined in the Reynolds number range of the tests. The Strouhal number computed from the power spectra of wake pressure was found to vary from .10 to .14. Oscillatory airfoil motion of $\pm$ 1.5° about the mean angle was found in nearly all cases to cause amplification of unsteady pressure in the wake. Increases in root mean square pressure of as much as 80% were observed. These increases were found to occur in a very narrow frequency band around the frequency of airfoil motion, and at the first harmonic of that frequency. The vertical distribution of pressure in the wake was found to exhibit similarity under most dynamic conditions.

4. One test condition was examined for Strouhal resonance effects, in which the drive frequency was near the frequency of natural vortex shedding. A large increase in unsteady wake pressure coefficient was noted, with the frequency distribution of mean square pressure behaving essentially the same as for other test conditions. The presence of a vortex wake was consistent with theoretical pressure for a double row of vortices.

Recommendations

1. The analytical model developed here contains the mathematical framework on which to build a more complete model for stall. This can be done by allowing mutual interaction between wake vortices and bound vorticity, so that the vortex trajectory assumption can be removed, as well as the assumed vortex velocity. The question of

shedding phase and vortex strength can only be resolved by considering the mechanism of vorticity production in the boundary layer.

2. It may be possible to couple a time dependent description of the outer potential flow with a time dependent boundary layer analysis such as given by Moore [12]. An analysis of this type is necessary in order to understand how the boundary layer, body motion, and outer flow field combine to produce the observed wake coherency.

3. The experimental investigation of dynamic wakes should be extended to higher Reynolds numbers and higher airfoil frequencies, with pressure measurements being made at several downstream locations. The limited data available in the present study indicated significant changes in wake structure between positions at one and three chordlengths downstream. Detailed measurements are needed at several locations to define the rate of growth of wake width, the rate of decay of intensity, and the convective velocity of vortices within the wake.

APPENDIX A

BACKGROUND ON SINGULAR INTEGRAL EQUATIONS WITH A CAUCHY KERNEL

The material presented here is for convenience in understanding the treatment of the particular problem occurring in the analytical section of the text, and therefore is limited to a discussion of open contour boundary value problems possessing integrable singularities in the density at the end-points of the contour. Further physical consideration leads to the conclusion that all disturbances tend to zero sufficiently far awy, in any direction, from the contour in question.

The plane boundary value problems of potential theory are amenable to analysis by the methods of complex function theory. In particular, singular integrals of the Cauchy type occurring in integral equation formulations are considered in the following developments.

The Holder condition [29] is assumed valid for the problem in question, and this condition states that a function $\varphi(t)$ defined on a smooth contour L satisfies the condition if for two arbitrary points of the curve,

$$|\varphi(t_2) - \varphi(t_1)| < A(t_2 - t_1)^{\lambda} \tag{86}$$

where $0 < \lambda \leq 1$. This condition ensures the integrability of integrals of the Cauchy type,

$$\Phi(z) = \frac{1}{2\pi i}\int_{L} \frac{\varphi(\tau)}{\tau - z}\, d\tau \qquad (87)$$

where $\varphi(\tau)$ on the countour L satisfies the Holder condition, except at the endpoints of the contour, where it has singularities of the integrable type. The value of such integrals is determined in the sense of Cauchy principal value. Equation (87) defines an analytic function, $\Phi(z)$, $z \notin L$, in terms of the integral of a density function $\varphi(\tau)$ along some contour. The question arises in boundary value problems as to what the limiting values of $\Phi(z)$ are upon approaching the contour L from either side. One side of the contour L is denoted by + and the other side by - . To determine the sides uniquely, consider the contour L extended into a closed contour. The + side of L is then taken on the left when traversing the contour in the counterclockwise direction. Consider the function $\Phi(z)$, defined by the singular integral in equation (87) and let z approach the point t, $t \in L$, (not including the ends points) from the + and - sides along arbitrary paths. Denote the limiting values of $\Phi(z)$ by $\Phi^{+}(t)$ and $\Phi^{-}(t)$ respectively. Then the following results govern the limiting behavior of $\Phi(z)$ on the contour in terms of the integral and its density,

$$\Phi^{+}(t) - \Phi^{-}(t) = \varphi(t) \qquad (88)$$

$$\Phi^{+}(t) + \Phi^{-}(t) = \frac{1}{\pi i}\int_{L} \frac{\varphi(\tau)}{\tau - t}\, d\tau \qquad (89)$$

where t is not an endpoint of L.

These relations are known as the Plemelj formulae [29], and are basic to the study of a large class of boundary value problems. The analytic function $\Phi(z)$ has a jump across L as just described, and is therefore called sectionally analytic. According to a theorem given in [29], (pg. 53) the function $\Phi(z)$ will possess the same type of singular behavior in the neighborhood of an endpoint c of the contour L as does the density function. Since it is required that $\varphi(t)$ possess integrable singularities at both ends of the contour, $\Phi(z)$ must also exhibit this behavior; an integrable singularity being defined by

$$\lim_{z \to c} \Phi(z) \sim \frac{B}{(z-c)^{\mu}}\,, \quad 0 < Re\,\mu < 1 \qquad (90)$$

where B is an arbitrary constant.

Consider the following Riemann boundary value problem for a sectionally analytic function $\Phi(z)$,

$$\Phi^{+}(t) - \Phi^{-}(t) = \varphi(t)\,, \quad t \in L\,, \; t \neq c \qquad (91)$$

The Plemelj formulae suggest the solution

$$\Phi_c(z) = \frac{1}{2\pi i}\int_L \frac{\varphi(t)}{t-z}\,dt \tag{92}$$

To establish the uniqueness of this solution, consider the difference,

$$\Phi_1(z) = \Phi(z) - \Phi_c(z) \tag{93}$$

where $\Phi_1(z)$ is sectionally analytic. Then the boundary value for this function is

$$\Phi_1^+(t) - \Phi_1^-(t) = 0\,, \quad t \in L\,, \quad t \neq c \tag{94}$$

hence by analytic continuation $\Phi_1(z)$ is regular everywhere except possibly at infinity and at the endpoints of L. But the endpoint singularities are weak and removable, therefore $\Phi_1(z)$ is regular everywhere except possibly at infinity. Consider the two possibilities for the asymptotic behavior of $\Phi(z)$ as $|z| \to \infty$:

i) $\Phi(z) \to 0$ as $|z| \to \infty$, ii) $\Phi(z) \sim O(|z|^m)$ as $|z| \to \infty$, and $m \geq 0$. In the first case it follows that $\Phi_1(z) \equiv 0$ from Liouville's theorem since $\Phi_1(z)$ is analytic in the finite part of the plane and zero at infinity. Thus the only solution is $\Phi(z) = \Phi_c(z)$. In the second case it follows again from Liouville's theorem that

$$\Phi_1(z) = P_m(z) \tag{95}$$

where $P_m(z)$ is an m^{th} order polynomial in z. Hence in this case the general solution of Equation (91) is

$$\Phi(z) = \frac{1}{2\pi i}\int_L \frac{\phi(t)}{t-z}\,dt + P_m(z) \tag{96}$$

Consider the singular integral equation,

$$\frac{1}{\pi i}\int_L \frac{\varphi(t)}{t-z}\,dt = f(z), \quad z \in L \tag{97}$$

where $f(z)$ is a given continuous function and $\varphi(t)$ is unknown, having all the properties stated earlier. Form the sectionally analytic function

$$\Phi(z) = \frac{1}{2\pi i}\int_L \frac{\varphi(t)}{t-z}\,dt \tag{98}$$

possessing integrable singularities at the endpoints C. Then according to the Plemelj formulae, the solution is expressible in the form,

$$\varphi(t) = \Phi^+(t) - \Phi^-(t) \tag{99}$$

where

$$\Phi^+(t) + \Phi^-(t) = f(t) \tag{100}$$

To obtain the solution of Equation (100), we will first obtain a particular solution, $F(z)$, of the corresponding homogeneous equation. We therefore require to solve

$$F^{+}(t) - (-1)\, F^{-}(t) = 0 \tag{101}$$

which enables us to write,

$$(-1) = \frac{F^{+}(t)}{F^{-}(t)} \tag{102}$$

The original problem is then factorized as follows

$$\Phi^{+}(t) - \frac{F^{+}(t)}{F^{-}(t)}\,\Phi^{-}(t) = f(t) \tag{103}$$

or

$$\frac{\Phi^{+}(t)}{F^{+}(t)} - \frac{\Phi^{-}(t)}{F^{-}(t)} = \frac{f(t)}{F^{+}(t)} \tag{104}$$

Consider Equation (104) as a new boundary value problem. Then the solution $\Phi(z)/F(z)$ is, according to our previous development,

$$\frac{\Phi(z)}{F(z)} = \frac{1}{2\pi i}\int_{L} \frac{\frac{f(t)}{F^{+}(t)}}{t-z}\,dt + P_{m}(z) \tag{105}$$

To find the solution of Equation (101), take the logarithm of Equation (102), giving

$$\ln F^{+}(t) - \ln F^{-}(t) = \ln(-1) \tag{106}$$

From the Plemelj formulae, this implies

$$\ln F(z) = \frac{1}{2\pi i} \int_{L} \frac{\ln(-1)}{t - z}\, dt \tag{107}$$

or, since $\ln(-1) = \pi i$

$$\ln F(z) = \frac{1}{2} \int_{L} \frac{dt}{t - z} \tag{108}$$

Let the contour L be as sketched below, where z_1 and z_2 are the end-points.

Then

$$F(z) = \sqrt{\frac{z - z_1}{z - z_2}} \tag{109}$$

therefore

$$\frac{f(t)}{F^{+}(t)} = \sqrt{\frac{t - z_1}{t - z_2}}\, f(t) \tag{110}$$

and Equation (106) now reads,

$$\Phi(z) = \frac{1}{2\pi i}\sqrt{\frac{z-z_2}{z-z_1}}\int_L \sqrt{\frac{t-z_1}{t-z_2}}\,\frac{f(t)}{t-z}\,dt + \sqrt{\frac{z-z_2}{z-z_1}}\,P_m(z) \qquad (111)$$

But, from Equation (98), $\Phi(z)$ is required to possess integrable singularities at both ends of the interval, according to a result stated earlier, because the density function $\varphi(t)$ is required to have that behavior. To insure the singularity at z_2, we require to modify $F(z)$ as follows. Let

$$F^*(z) = \frac{1}{z-z_2}\,F(z) \qquad (112)$$

then $F^*(z)$ still satisfies the homogeneous boundary value problem, i.e.,

$$F^{*+}(t) + F^{*-}(t) = 0 \qquad (113)$$

This solution will be used for the condition of integrable singularities at both ends of the open contour. Then

$$\frac{f(t)}{F^{*+}(t)} = \sqrt{(t-z_1)(t-z_2)}\,f(t) \qquad (114)$$

Returning to Equation (105) and replacing $F(z)$ by $F^*(z)$, the following form results for singularities admissible at both ends of L,

$$\frac{\Phi(z)}{F^*(z)} = \frac{1}{2\pi i}\int_{z_1}^{z_2} \frac{f(t)}{F^{*+}(t)}\frac{dt}{t-z} + P_m(z) \qquad (115)$$

Let the contour L be the real line between $X=-1$ and $X=1$, then the solution is,

$$\Phi(z) = \frac{1}{2\pi i\sqrt{(z-1)(z+1)}}\int_{-1}^{+1} \frac{f(x)\sqrt{(x-1)(x+1)}}{x-z}\,dx + \frac{P_m(z)}{\sqrt{(z-1)(z+1)}} \qquad (116)$$

As stated earlier, the function $P_m(z)$ is a polynomial of degree m.

Now consider the integral equation stated in the text, Equation (29). The general form of this equation may be taken as,

$$\phi(x) = \frac{1}{\pi i}\int_{-1}^{+1} \frac{\gamma_a(\xi)}{\xi - x}\,d\xi \qquad (117)$$

Then following Carleman define a function $\Phi(z)$ by

$$\Phi(z) = \frac{1}{2\pi i}\int_{-1}^{+1} \frac{\gamma_a(\xi)}{\xi - z}\,d\xi \qquad (118)$$

which is analytic for all z not contained in the interval $(-1, +1)$. Then according to the Plemelj Formulae,

$$\gamma_a(x) = \Phi^+(x) - \Phi^-(x) \qquad (119)$$

and $\Phi(z)$ has the form given in Equation (116). The polynomial $P_m(z)$ in Equation (116) is reduced to a constant for the flow problem in question because it is assumed that a finite number of vortices exist in the wake, and the motion is assumed to have persisted for a sufficient length of time to allow flow transients to subside. Then $\Phi(z)$ is given by

$$\Phi(z) = \frac{1}{2\pi i \sqrt{(z-1)(z+1)}} \int_{-1}^{+1} \frac{\sqrt{(x-1)(x+1)}\, f(x)}{x-z}\, dx + \frac{A}{\sqrt{(z-1)(z+1)}} \qquad (120)$$

where A is an arbitrary constant. It is noted that from the standpoint of the mathematical theory involved, the physical problem is reduced to that of a configuration existing at a fixed time, which is consistent with the assumption of quasi-steady flow. Thus the mathematical solution consists of determining the boundary value consistent with the given disturbances at a particular instant, or for a particular configuration.

The function $f(x^*)$ is, from Equation (29),

$$f(x^*) = \frac{2}{i}\left\{ -b x^* \dot{\alpha} - U \sin\alpha, \right. \qquad (121)$$

$$\left. + \frac{\Gamma}{2\pi b}\left[\sum_{i=1}^{I} \frac{(x^* - x_i^*)}{(x^* - x_i^*)^2 + y_i^{*2}} - \sum_{j=1}^{J} \frac{(x^* - x_j^*)}{(x^* - x_j^*)^2 + y_j^{*2}} \right] \right\}$$

It remains to perform the integration indicated in Equation (120). The most convenient way to accomplish this is to use a representation in the

complex plane, [30, p.445]. Since the difficulty in integrating the expression in Equation (121) occurs due to the wake vortex terms, the expression

$$f_1(\tilde{x}) = \frac{2}{i}\frac{\tilde{x}-\hat{x}}{(\tilde{x}-\hat{x})^2+\hat{y}^2} \tag{122}$$

will be used for illustration in the following development. The change in symbols is used for convenience, thus the point $(\hat{x}, \hat{y})$ now is the fixed position and $\tilde{x}$ varies over $(-1, +1)$. The integral to be evaluated is

$$I(z) = \frac{2}{i}\int_{-1}^{1} \frac{\sqrt{(\tilde{x}-1)(\tilde{x}+1)}\,(\tilde{x}-\hat{x})}{[(\tilde{x}-\hat{x})^2+\hat{y}^2](\tilde{x}-z)}\,d\tilde{x} \tag{123}$$

Now form

$$\Omega(z) = \frac{1}{2\pi i}\int_{\Lambda} \frac{\sqrt{(\zeta-1)(\zeta+1)}\,(\zeta-\hat{x})}{[(\zeta-\hat{x})^2+\hat{y}^2](\zeta-z)}\,d\zeta \tag{124}$$

where the complex ζ-plane and the path Λ are as sketched below

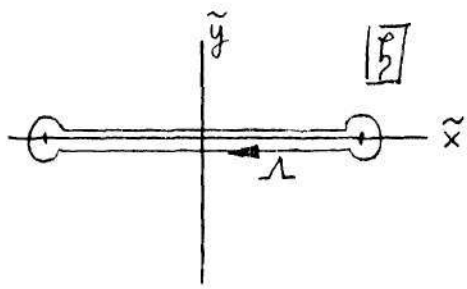

Equation (124) can be written as

$$\Omega(z) = \frac{1}{2\pi i}\int_{L} \frac{\sqrt{(\zeta+1)(\zeta-1)}\,(\hat{\zeta}-\hat{\chi})}{(\zeta-\hat{\zeta})(\zeta+\bar{\hat{\zeta}})(\zeta-z)}\,d\zeta \tag{125}$$

where $\hat{\zeta} = \hat{x} + i\hat{y}$ and $\bar{\hat{\zeta}}$ is the corresponding complex conjugate. In Reference [30] it is shown how integrals of the Cauchy type, singular at ∞, can be evaluated in terms of principal parts. An extension of the method can be made utilizing the following theorem from complex variable theory [38]:

> Let $f(z)$ be regular in S^- and continuous in $S^- + L$, except at the points $a_1, \cdots, a_n$, and at $z = \infty$, where it may have poles with principal parts $G_1(z)$, $G_2(z), \cdots, G_n(z), G_\infty(z)$.
> Then,
>
> $$\frac{1}{2\pi i}\int_{L} \frac{f(t)}{t-z}\,dt = -f(z) + G_1(z) + \cdots + G_n(z) + G_\infty(z), \quad z \in S^- \tag{126}$$

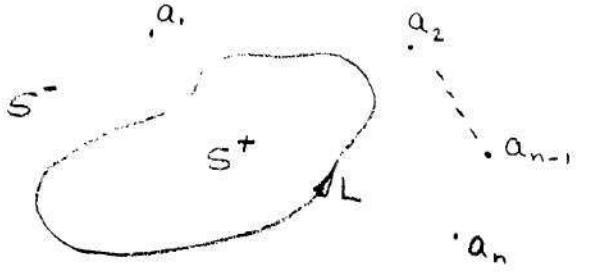

For the present application the signs on the right in the above theorem are changed since Λ is traversed so that S^- is on the left. The part of Equation (125) corresponding to $f(t)$ in the preceding theorem has singularities at $\zeta = \hat{\xi}$ and $\zeta = \bar{\hat{\xi}}$, but not at ∞. Therefore Equation (30) becomes

$$\Omega(z) = -\frac{\sqrt{(z-1)(z+1)}\,(z-\hat{x})}{(z-\hat{\xi})(z-\bar{\hat{\xi}})} - G_{\hat{\xi}}(z) - G_{\bar{\hat{\xi}}}(z) - G_{\infty}(z) \qquad (127)$$

Expanding $f(z)$ about the singular points, the principal parts are found to be

$$G_{\hat{\xi}}(z) = \sqrt{(\hat{\xi}-1)(\hat{\xi}+1)}\left[\frac{(\hat{\xi}-\hat{x})}{(\hat{\xi}-\bar{\hat{\xi}})}\frac{1}{(z-\hat{\xi})}\right] \qquad (128)$$

$$G_{\bar{\hat{\xi}}}(z) = \sqrt{(\bar{\hat{\xi}}-1)(\bar{\hat{\xi}}+1)}\left[\frac{(\bar{\hat{\xi}}-\hat{x})}{(\bar{\hat{\xi}}-\hat{\xi})}\frac{1}{(z-\bar{\hat{\xi}})}\right] \qquad (129)$$

and (note there is not a singularity at infinity, but there is a principal part, from the definition),

$$G_{\infty}(z) = \lim_{|z|\to\infty} \frac{\sqrt{(z-1)(z+1)}\,(z-\hat{x})}{(z-\hat{\xi})(z-\bar{\hat{\xi}})} = 1 \qquad (130)$$

Thus the integral $I(z)$ becomes,

$$I(z) = 2\pi \left\{ \frac{\sqrt{(z-1)(z+1)}\,(z-\hat{x})}{(z-\hat{\xi})(z-\bar{\xi})} - \frac{\sqrt{(\hat{\xi}+1)(\hat{\xi}-1)}\,(\hat{\xi}-\hat{x})}{(\hat{\xi}-\bar{\xi})(z-\hat{\xi})} \right. \tag{131}$$

$$\left. - \frac{\sqrt{(\bar{\xi}-1)(\bar{\xi}+1)}\,(\bar{\xi}-\hat{x})}{(\bar{\xi}-\hat{\xi})(z-\bar{\xi})} - 1 \right\}$$

and $\Phi(z)$ becomes

$$\Phi(z) = \frac{1}{i\sqrt{(z-1)(z+1)}} \left\{ \frac{\sqrt{(z+1)(z-1)}\,(z-\hat{x})}{(z-\hat{\xi})(z-\bar{\xi})} \right. \tag{132}$$

$$\left. - \frac{\sqrt{(\hat{\xi}+1)(\hat{\xi}-1)}\,(\hat{\xi}-\hat{x})}{(\hat{\xi}-\bar{\xi})(z-\hat{\xi})} - \frac{\sqrt{(\bar{\xi}+1)(\bar{\xi}-1)}\,(\bar{\xi}-\hat{x})}{(\bar{\xi}-\hat{\xi})(z-\bar{\xi})} - 1 \right\}$$

Now to evaluate $\Phi^{+}(x)$ and $\Phi^{-}(x)$, $-1 < x < 1$, a definite branch cut is chosen to evaluate the expression

$$\sqrt{(z-1)(z+1)} = i\sqrt{(1-z)(1+z)} \tag{133}$$

Taking cuts along the x-axis from -1 to $-\infty$ and from $+1$ to $-\infty$, the limiting values are found as follows,

$$\left.\begin{aligned} \lim_{z \to x^{+}} \sqrt{(1-z)(1+z)} &= \sqrt{(1-\tilde{x})(1+\tilde{x})} \\ \lim_{z \to x^{-}} \sqrt{(1-z)(1+z)} &= -\sqrt{(1-\tilde{x})(1+\tilde{x})} \end{aligned}\right\} -1 < \tilde{x} < 1 \tag{134}$$

Thus

$$\Phi^{+}(\tilde{x}) - \Phi^{-}(\tilde{x}) = \frac{2}{\sqrt{1-\tilde{x}^2}} \left\{ \frac{\sqrt{(\hat{\xi}-1)(\hat{\xi}+1)}\,(\hat{\xi}-\hat{x})}{(\hat{\xi}-\bar{\hat{\xi}})(\tilde{x}-\hat{\xi})} \right. \tag{135}$$

$$\left. + \frac{\sqrt{(\bar{\hat{\xi}}+1)(\bar{\hat{\xi}}-1)}\,(\bar{\hat{\xi}}-\hat{x})}{(\bar{\hat{\xi}}-\hat{\xi})(\tilde{x}-\bar{\hat{\xi}})} + 1 \right\}$$

Thus constant will be neglected at this point, since it can be combined with the arbitrary constant A, given in Equation (25). Using the definitions,

$$\hat{\xi} = \hat{x} + i\,\hat{y} \quad , \quad \bar{\hat{\xi}} = \hat{x} - i\,\hat{y} \tag{136}$$

in Equation (135), the result can be expressed in terms of $\hat{x}$ and $\hat{y}$ as follows

$$\Phi^{+}(\tilde{x}) - \Phi^{-}(\tilde{x}) = \frac{2\left[(\hat{x}^2-\hat{y}^2-1)^2 + 4\hat{x}^2\hat{y}^2\right]^{1/4}\left[(\tilde{x}-\hat{x})\cos\frac{\theta}{2} - \hat{y}\sin\frac{\theta}{2}\right]}{\sqrt{1-\tilde{x}^2}\left[(\tilde{x}-\hat{x})^2+\hat{y}^2\right]} \tag{137}$$

where

$$\theta = \tan^{-1}\frac{2\hat{x}\hat{y}}{\hat{x}^2-\hat{y}^2-1} \tag{138}$$

The other terms in Equation (26) are evaluated in a manner similar to

that just demonstrated. Reverting to the original notation, the final solution for bound vorticity is,

$$\gamma_a(x^*) = \frac{(2x^{*2}-1)b\dot{\alpha}}{\sqrt{1-x^{*2}}} + \frac{1}{\sqrt{1-x^{*2}}}\left\{ A - 2U x^* \sin\alpha_0 \right. \tag{139}$$

$$- \frac{2\Gamma}{\pi b} \sum_{i=1}^{I} \frac{\left[(x_i^{*2} - y_i^{*2} - 1)^2 + 4x_i^{*2} y_i^{*2}\right]^{1/4} \left[(x^* - x_i^*)\cos\frac{\theta_i}{2} - y_i^* \sin\frac{\theta_i}{2}\right]}{\left[(x^* - x_i^*)^2 + y_i^{*2}\right]}$$

$$+ \frac{2\Gamma}{\pi b} \sum_{j=1}^{J} \frac{\left[(x_j^{*2} - y_j^{*2} - 1)^2 + 4x_j^{*2} y_j^{*2}\right]^{1/4} \left[(x^* - x_j^*)\cos\frac{\theta_j}{2} - y_j^* \sin\frac{\theta_j}{2}\right]}{\left[(x^* - x_j^*)^2 + y_j^{*2}\right]}$$

where

$$\theta_i = \tan^{-1} \frac{2 x_i^* y_i^*}{x_i^{*2} - y_i^{*2} - 1} \tag{140}$$

and

$$\theta_j = \tan^{-1} \frac{2 x_j^* y_j^*}{x_j^{*2} - y_j^{*2} - 1} \tag{141}$$

To evaluate the arbitrary constant A, in Equation (139), the requirement of conservation of circulation is applied, as stated in Equations (19) and (20). It is thus necessary to integrate the expression $\gamma_a(x^*)$ as given by Equation (139). To accomplish that it is convenient to

employ the notation of the complex plane as used to obtain the solution previously. Thus each of the i and j terms in the equation can be written equivalently as.

$$\frac{1}{\sqrt{1-\tilde{x}^2}}\left[\frac{\sqrt{(\hat{\xi}+1)(\hat{\xi}-1)}\,(\hat{\xi}-\hat{x})}{(\hat{\xi}-\bar{\xi})(\tilde{x}-\hat{\xi})}+\frac{\sqrt{(\bar{\xi}+1)(\bar{\xi}-1)}\,(\bar{\xi}-\hat{x})}{(\bar{\xi}-\hat{\xi})(\tilde{x}-\bar{\xi})}\right] \tag{142}$$

and a straightforward integration by the method used to evaluate Equation (122) gives,

$$\int_{-1}^{1}\left[\frac{\sqrt{(\hat{\xi}+1)(\hat{\xi}-1)}\,(\hat{\xi}-\hat{x})}{(\hat{\xi}-\bar{\xi})(\tilde{x}-\hat{\xi})}+\frac{\sqrt{(\bar{\xi}+1)(\bar{\xi}-1)}\,(\bar{\xi}-\hat{x})}{(\bar{\xi}-\hat{\xi})(\tilde{x}-\bar{\xi})}\right]\frac{d\tilde{x}}{\sqrt{1-\tilde{x}^2}}=-\pi \tag{143}$$

In this way the values of A are established as discussed previously.

APPENDIX B

INSTRUMENTATION CALIBRATION AND DATA CONVERSION

Two types of pressure transducers were used in the experimental program. As indicated in the schematic of Figure 19, two transducers were mounted on the airfoil and five transducers were mounted on a rake in a vertical array to form the wake probe. The airfoil transducers were of the differential type, measuring the difference in pressure between upper and lower surfaces of the airfoil. Due to data recording limitations, the differential transducers at 15% chord was not recorded on tape and thus was not numerically processed to generate power spectra. The transducer at 85% chord was recorded on tape and was numerically processed; however during the tests it was found that the response of this transducer was degraded by faulty wiring and the amplitude information obtained from it was incorrect. As discussed in the text, there did appear to be useful phase information contained in the number six transducer (85% chord). Calibration of the number six transducer was accomplished using hydrostatic pressure and a micromanometer. The transducer was mounted inside a glass test tube with the reference or lower face of the sensor vented to atmospheric pressures. A plastic tube was mounted in the test tube and extended out to the input side of the micromanometer, which was vented on the reference side to atmospheric pressure. The tube was inverted and lowered into a basin of water until a predetermined

setting of pressure on the micromanometer was reached. The bridge was supplied by a six volt battery and the output in millivolts was read on a millivolt meter. This technique permitted applied pressures as closely as could be read in hundredths of an inch of alcohol in the micromanometer. In Figure 53, the line labeled #6 is the calibration curve for this transducer. The sensitivity factor was found to be

$$S_6 = 10.8 \ \frac{mv}{psi} \tag{144}$$

The wake transducers, numbered one through five, were of the total pressure type, .125 inches in diameter and .031 inches thick. These transducers were solid state bridge types and were supplied with 10 volts d.c. from batteries. Calibration was accomplished using a micromanometer and a tube connected to an air supply valve. Each transducer was placed in the plastic tube and the end then clamped. The applied pressure was monitored on the micromanometer and the corresponding millivolt level of output was recorded. The lines labeled #1 through #5 in Figure 53 are the calibration curves as obtained from the average of three trails for each transducer. The shift in voltage level for the various transducers is caused by bridge imbalance inherent in the manufacture of the device. The difference in sign of the slope was caused by inadvertent change in polarity of the input voltage. This was accounted for in obtaining test data. Since only unsteady data were being sought in the tests, the bridge imbalance was not important and only the slope of the data was calculated. Using

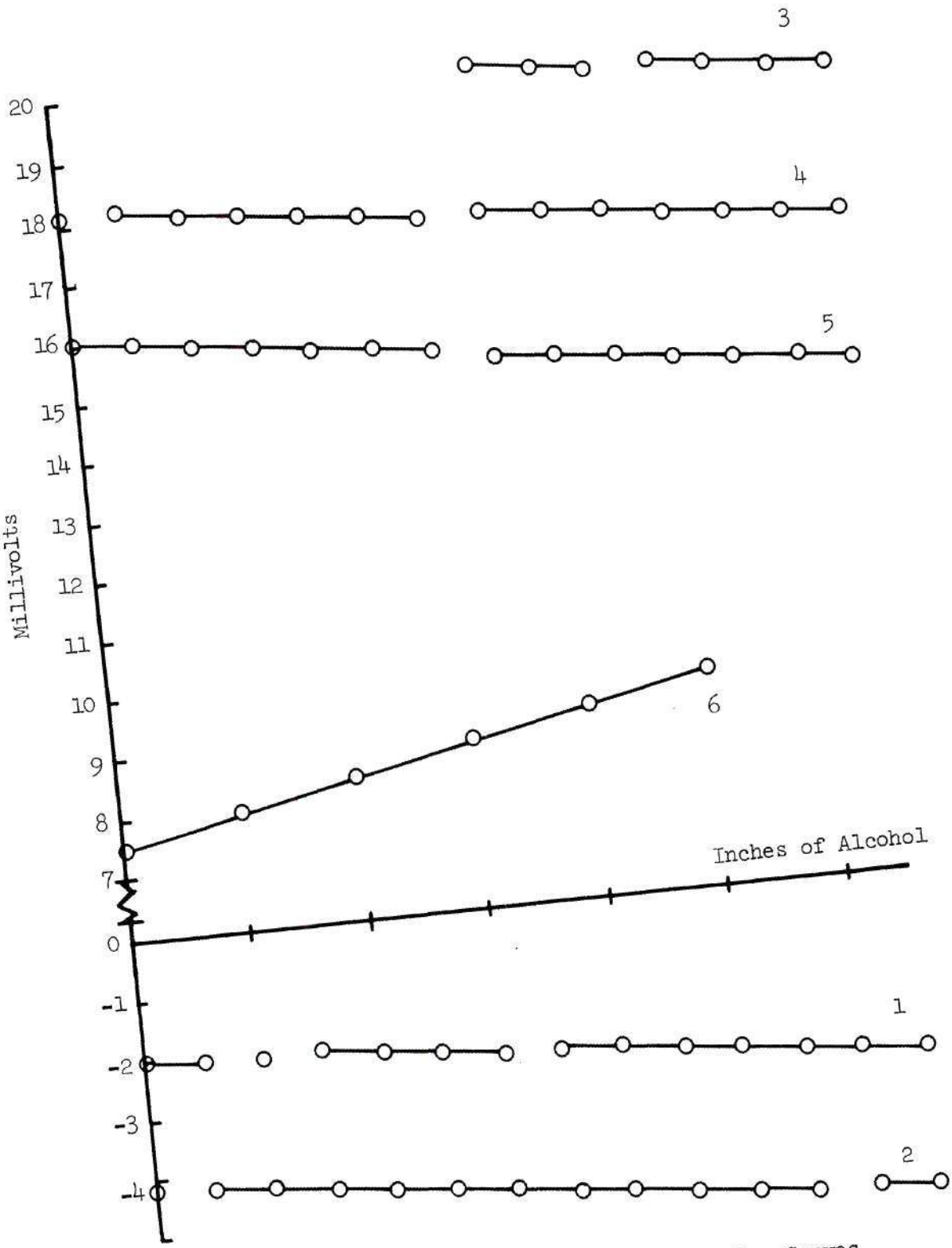

Figure 53. Pressure Transducer Calibration Curves

1 inch alcohol = .0293 psi,

the sensitivity of each of the total pressure transducers was found to be very nearly

$$S_i = 6.82 \ \frac{mv}{psi} \ , \ i = 1, \cdots, 5 \qquad (145)$$

As a check on the accuracy of the calibration, the #1 transducer was recalibrated using the more precise hydrostatic method, and the two values were found to agree.

The amplifiers used to gain the transducer signals were solid state, operational amplifiers with a range of ± 15 volts. The gain requirements were not well defined at the beginning of the tests, so each amplifier was stabilized at an arbitrary gain that was observed to provide a good reproducible signal on the tape recorder when an air hose was used at a distance of six to eight feet away from the transducers in order to excite them. This procedure resulted in a reliable recording capability down to at least 50 fps wind tunnel speed. The various amplifier gains were later evaluated, and found to vary from 1170 to 2000. The data conversion factors for computer processing were then established as follows. Let

S_i = sensitivity of i^{th} transducer, mv/psi, i = 1, --, 6

G_i = gain of amplifier in series with i^{th} transducer

E_i = recorder output voltage for i^{th} transducer (volts)

then

$$\Delta P_i = \frac{E_i}{S_i G_i (10^{-3})} \tag{146}$$

Let the conversion factor be

$$K_i = \frac{1}{S_i G_i (10^{-3})} \tag{147}$$

The conversion factor applied to each channel of data to obtain pressure time history in psi could then be computed as shown in Table 3.

Table 3. Transducer Conversion Factors to Obtain Pressure Time History

Transducer	S_i	G_i	K_i
1	6.82	1330	.1100
2	6.82	1170	.1255
3	6.82	1830	.0800
4	6.82	2000	.0735
5	6.82	1330	.1100
6	10.8	1330	.0700

APPENDIX C

ADDITIONAL TEST SPECTRAL DATA

Presented on the following pages are the raw power spectra of incremental pressure as obtained from the CDC 6400 Hybrid computer and plotted automatically using a Calcomp digital plotter. The spectra were computed for frequency intervals of 4.0 rad./sec. and are plotted between the limits of 2.5 cps and 100 cps. Each plot is identified, as to test condition, at the upper margin in the following format; the first digit indicates mean angle of attack:

1 = 15.0°

2 = 17.5°

3 = 20.0°

The second digit is always three (3), indicating that the spectrum was computed for the three chordlength wake position, i.e., three chordlengths downstream from the airfoil trailing edge. The next three digits indicate wind tunnel test section speed in feet per second. The last three digits indicate the airfoil oscillatory frequency in cycles per second. The third digit indicates cps in tenths. Thus for example:

2	—	3	—	180	—	165
↑		↑		↑		↑
$\alpha_o = 17.5°$		3 chordlengths		$U_\infty = 180$ fps		$f = 16.5$ cps

Also indicated at the top is the root mean square pressure, which results from numerical integration of the power spectrum. The spectra given are for the number two transducer only (see Figure 19 of the text). The sharp fluctuations superimposed on the general shape of the spectra are a result of the problem of resolution. As noted in the text, the time history data were divided into twenty segments of 2.5 seconds duration each. For any finite record lengths, resolution becomes more difficult as record length decreases. The reason for the spikes is shown by Bendat [35] to be due to Fourier transformation of sine waves of finite length that are not zero at the end of the record. The Fourier transform of a single sine wave of finite length is shown to generate relative maxima in the spectrum for frequencies on either side of the frequency of the sine wave. This scattering effect can be minimized by taking the average value of the spectrum at each frequency for a large number of samples. Further details on the numerical aspects of the problem are given in Reference [33].

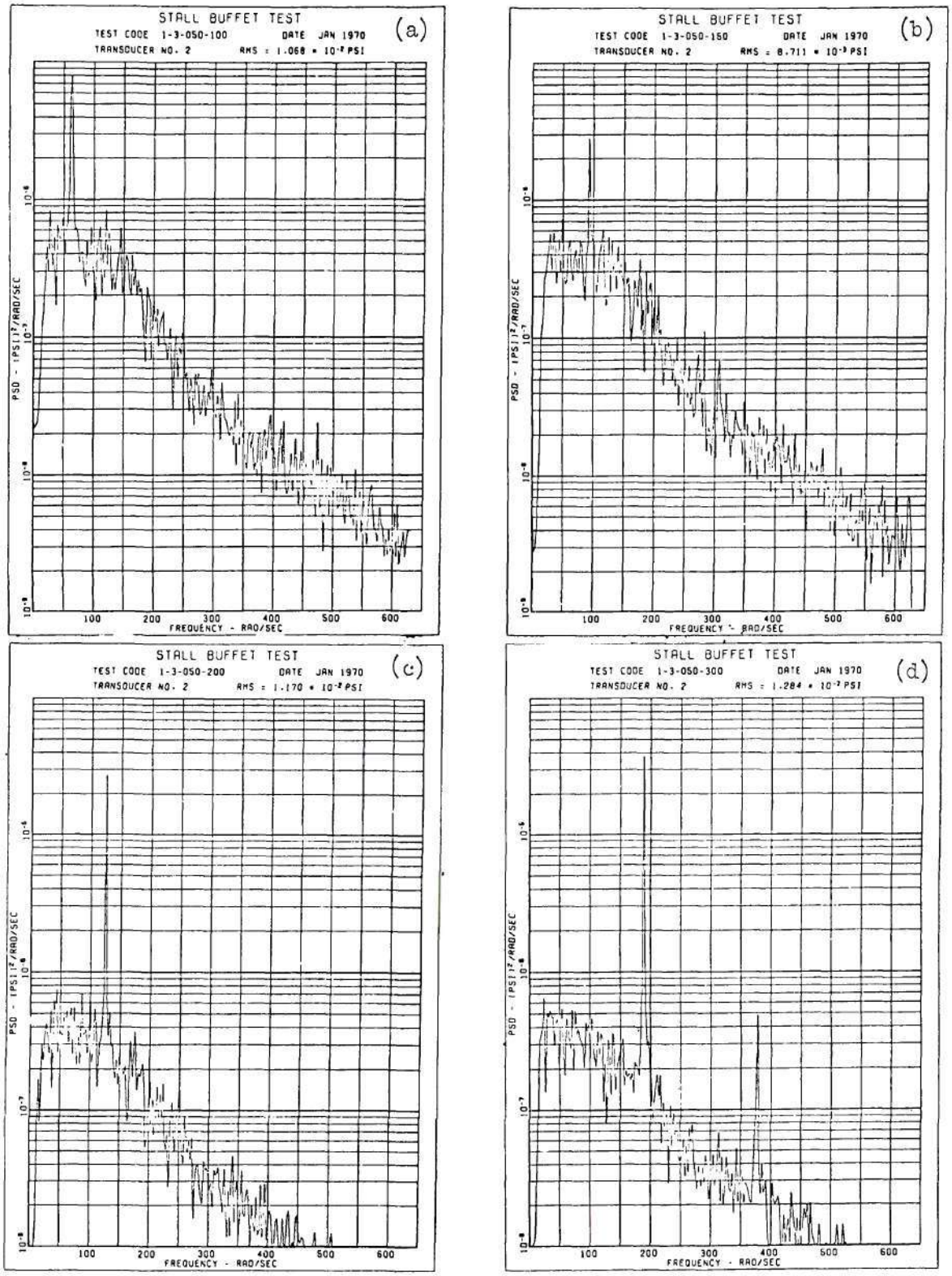

Figure 54. Additional Test Power Spectra,

$\alpha_o = 15.°$, $U_\infty = 50$ fps

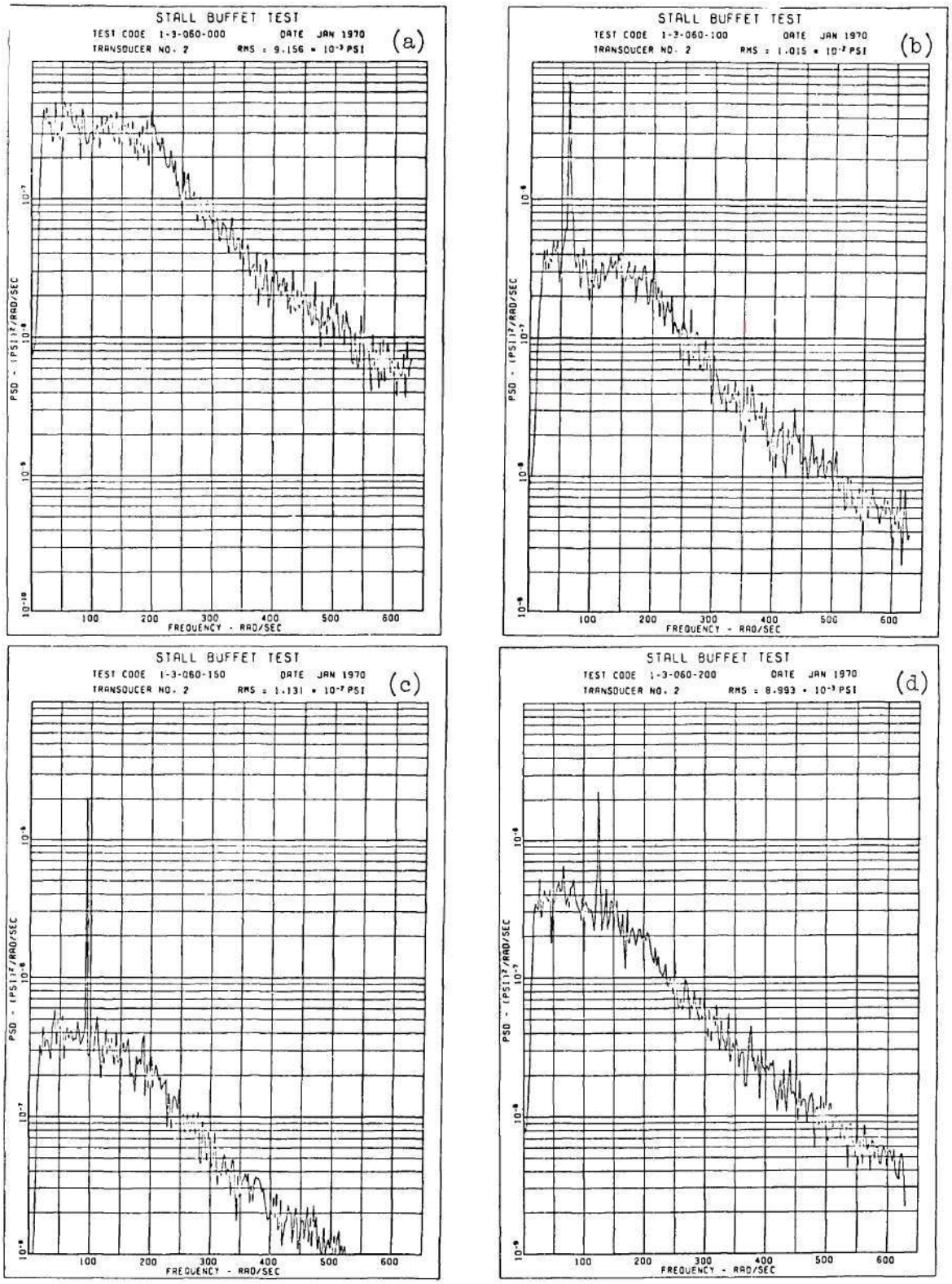

Figure 55. Additional Test Power Spectra,

$\alpha_o = 15.^\circ$, $U_\infty = 60$ fps

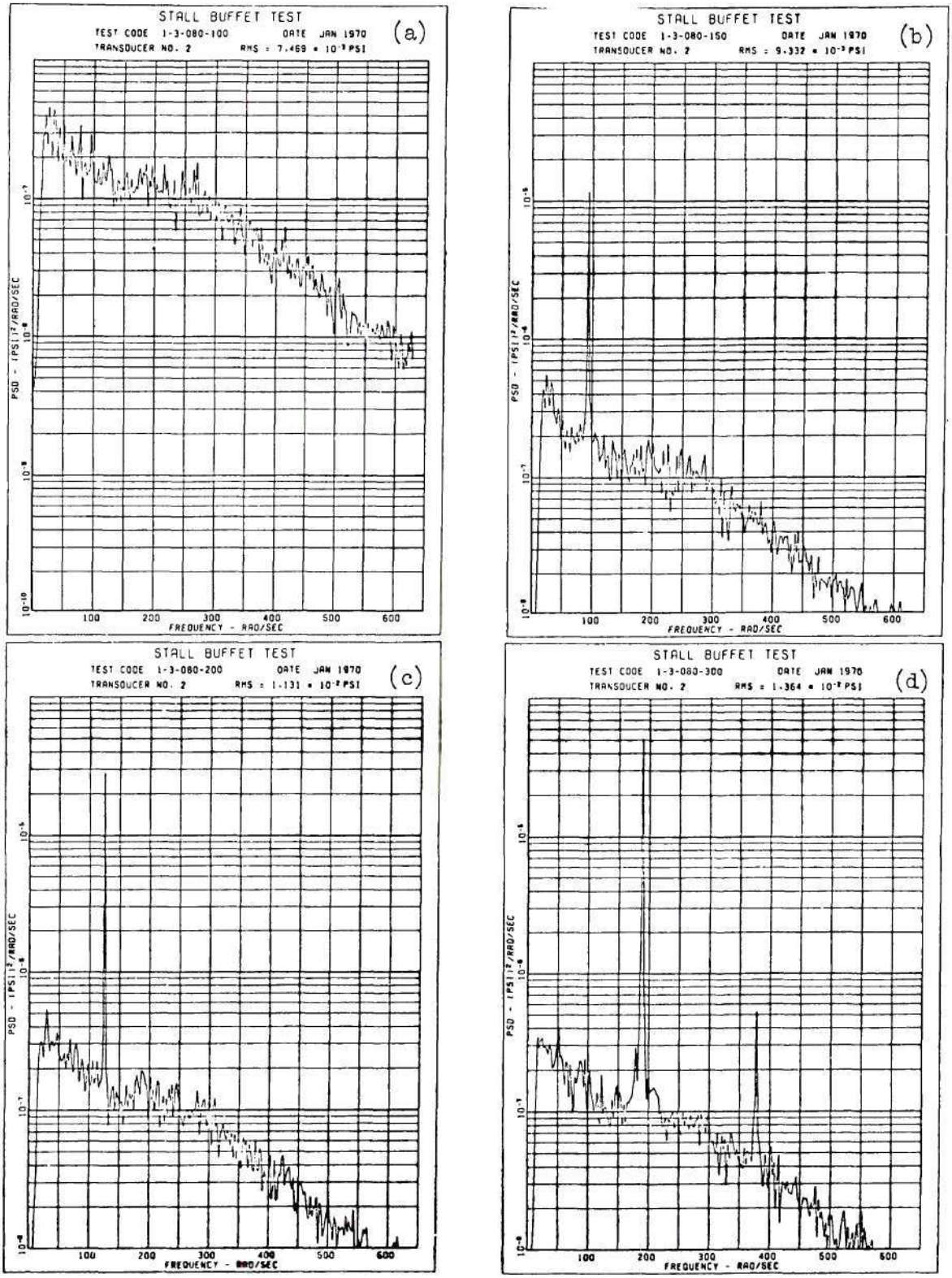

Figure 56. Additional Test Power Spectra,
$\alpha_o = 15.°$, $U_\infty = 80$ fps

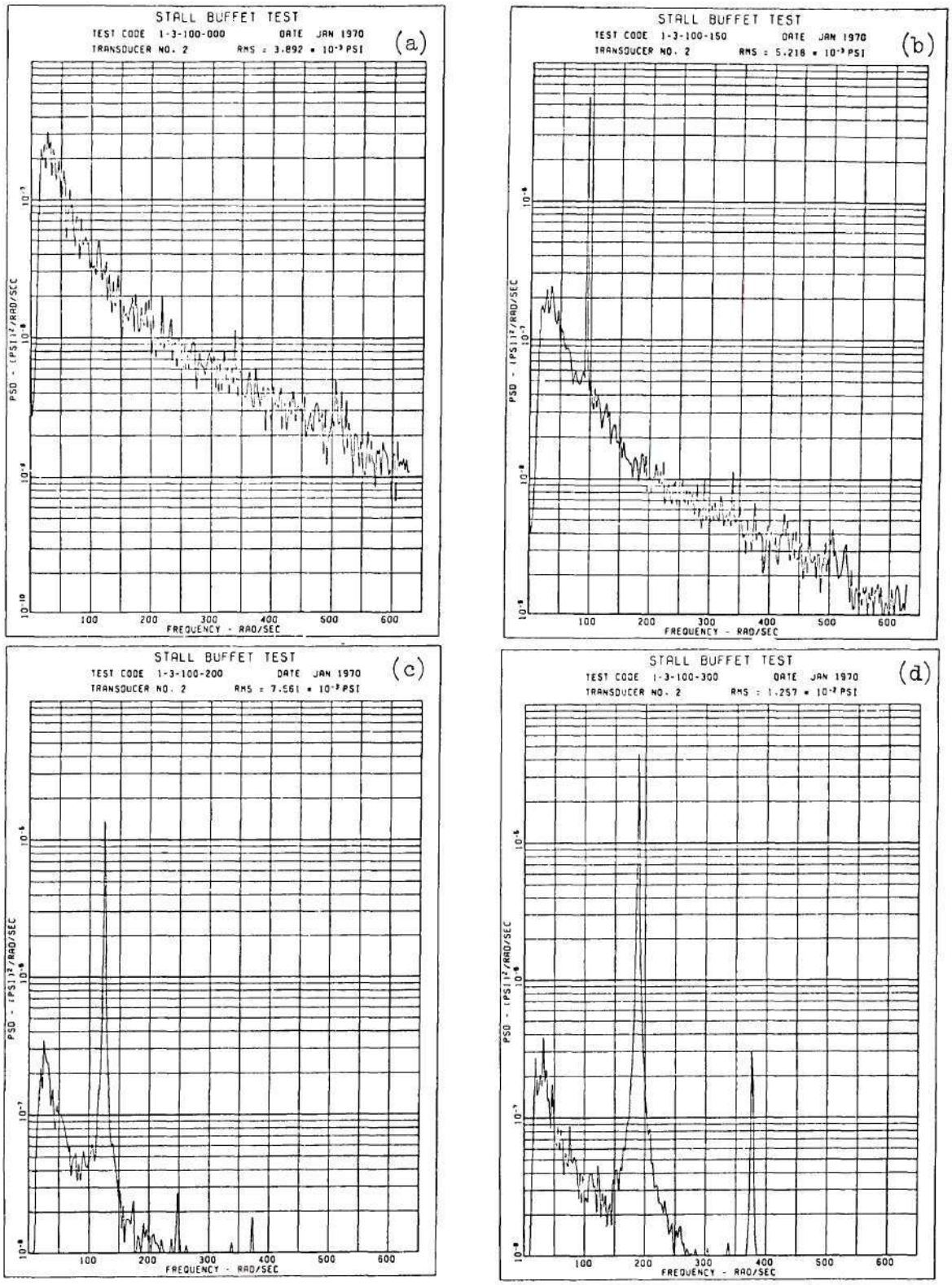

Figure 57. Additional Test Power Spectra,
$\alpha_o = 15.°$, $U_\infty = 100$ fps

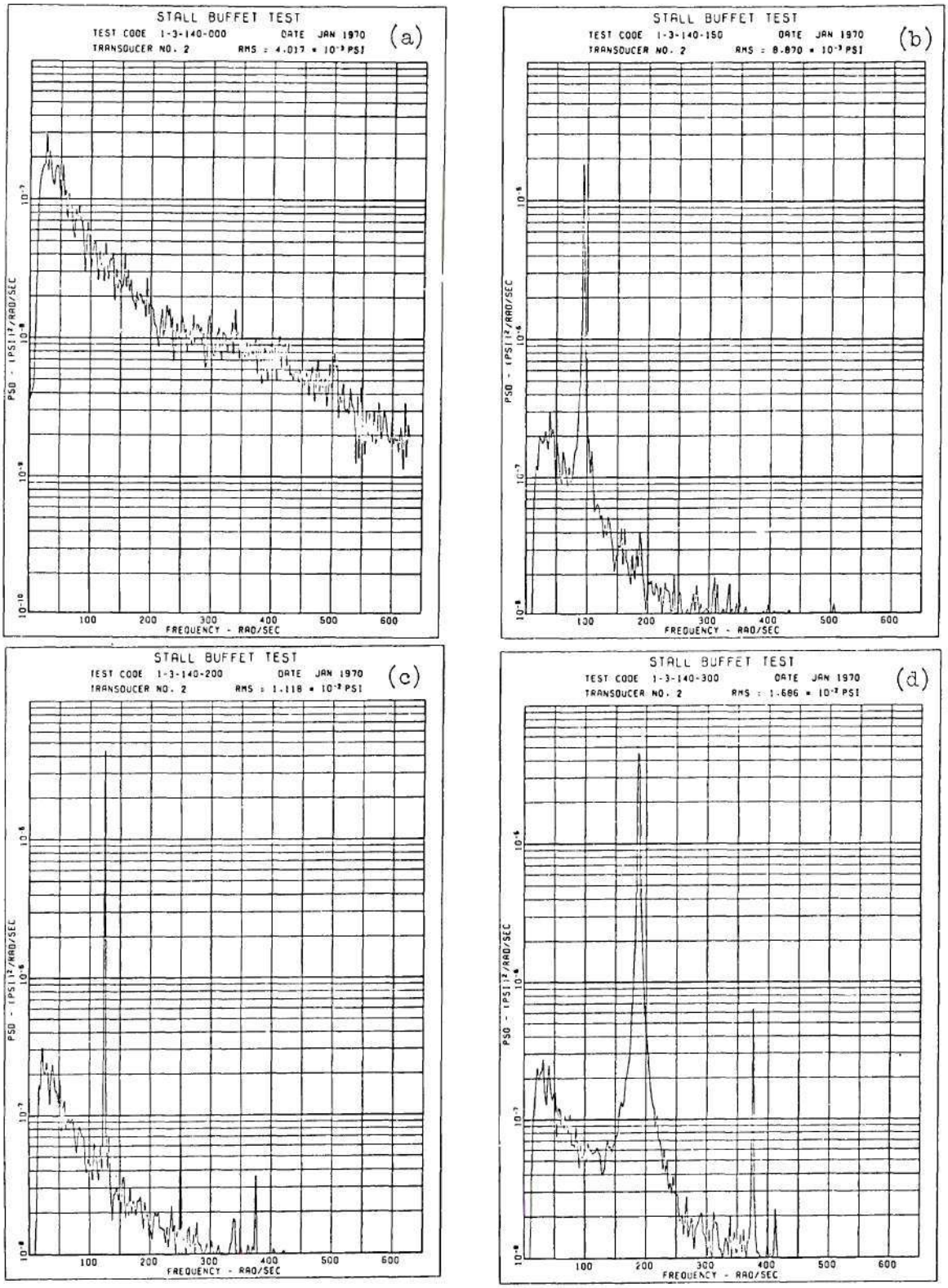

Figure 58. Additional Test Power Spectra,
$\alpha_o = 15.^\circ$, $U_\infty = 140$ fps

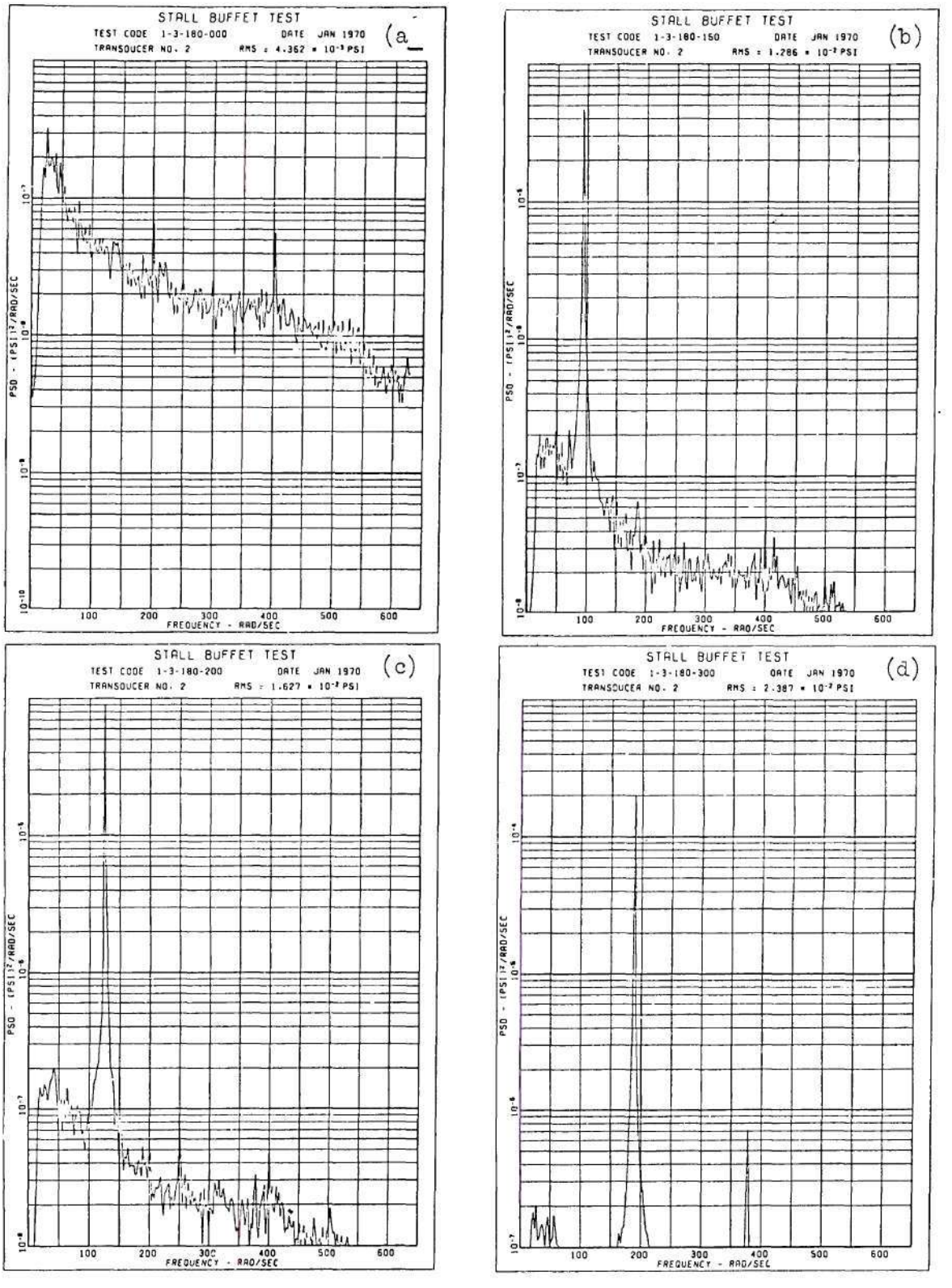

Figure 59. Additional Test Power Spectra,
$\alpha_o = 15.°$, $U_\infty = 180$ fps

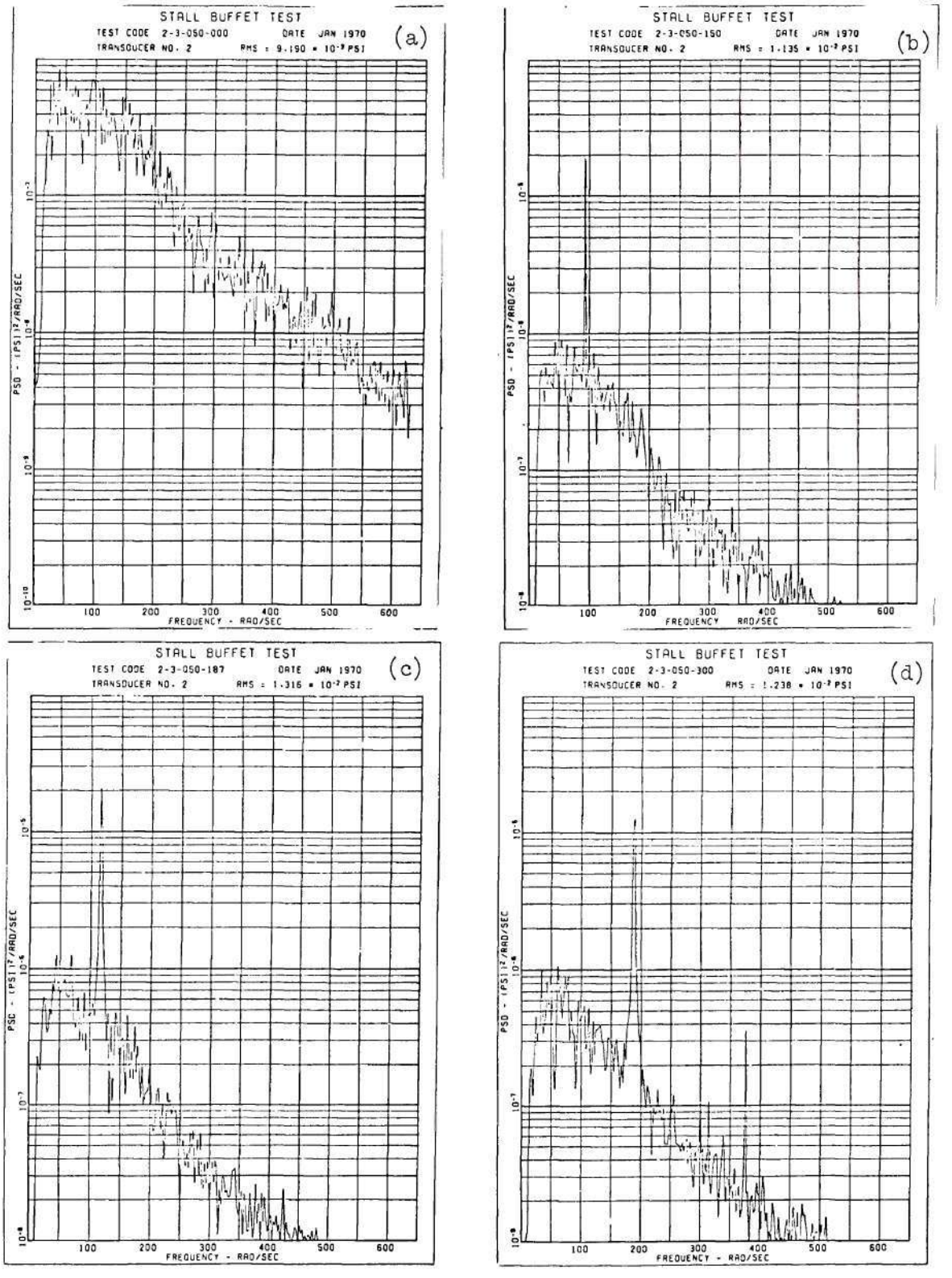

Figure 60. Additional Test Power Spectra,

$\alpha_o = 17.5°$, $U_\infty = 50$ fps

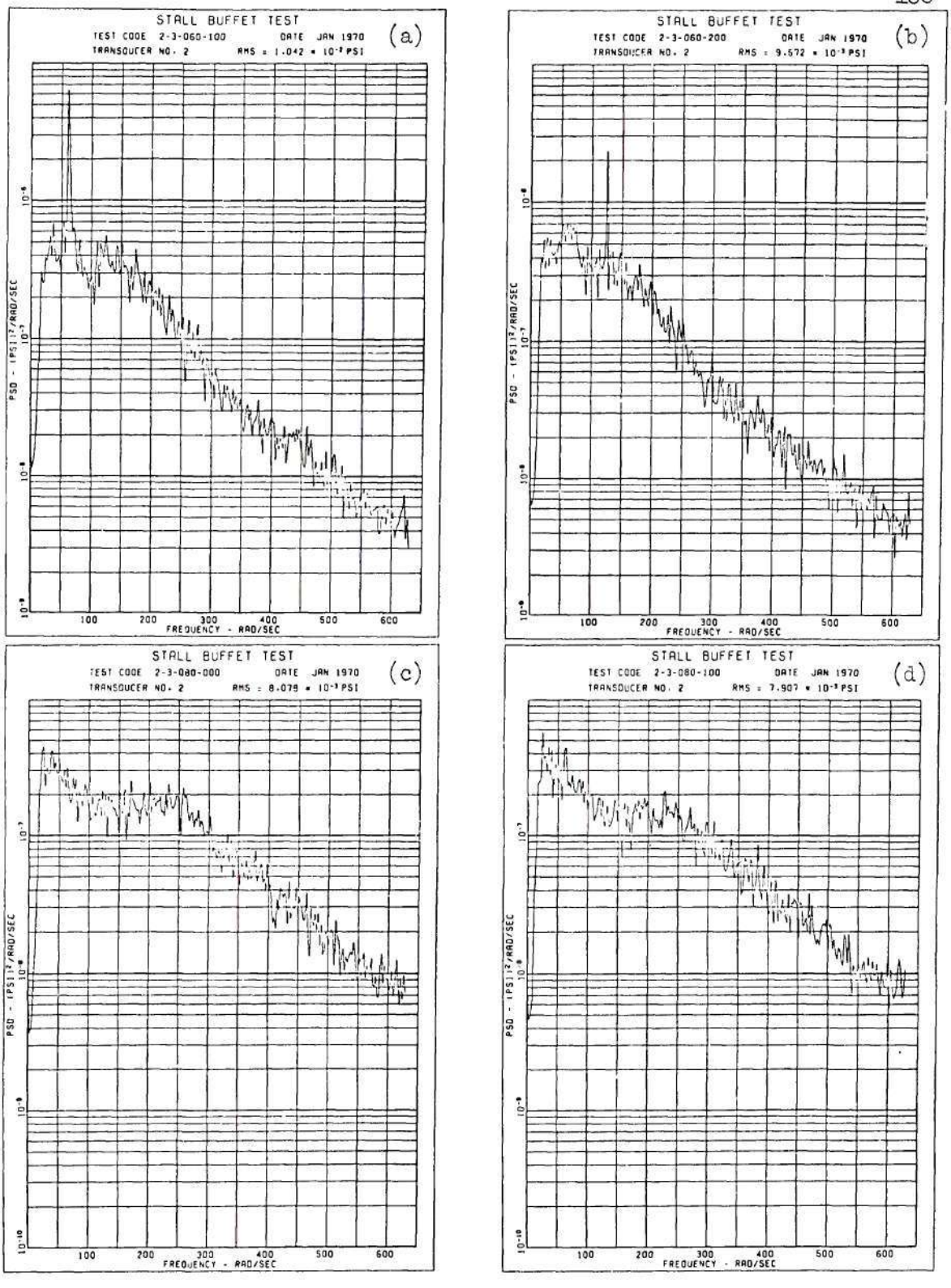

Figure 61. Additional Test Power Spectra,

$\alpha_o = 17.5°$, $U_\infty = 60$ fps, 100 fps

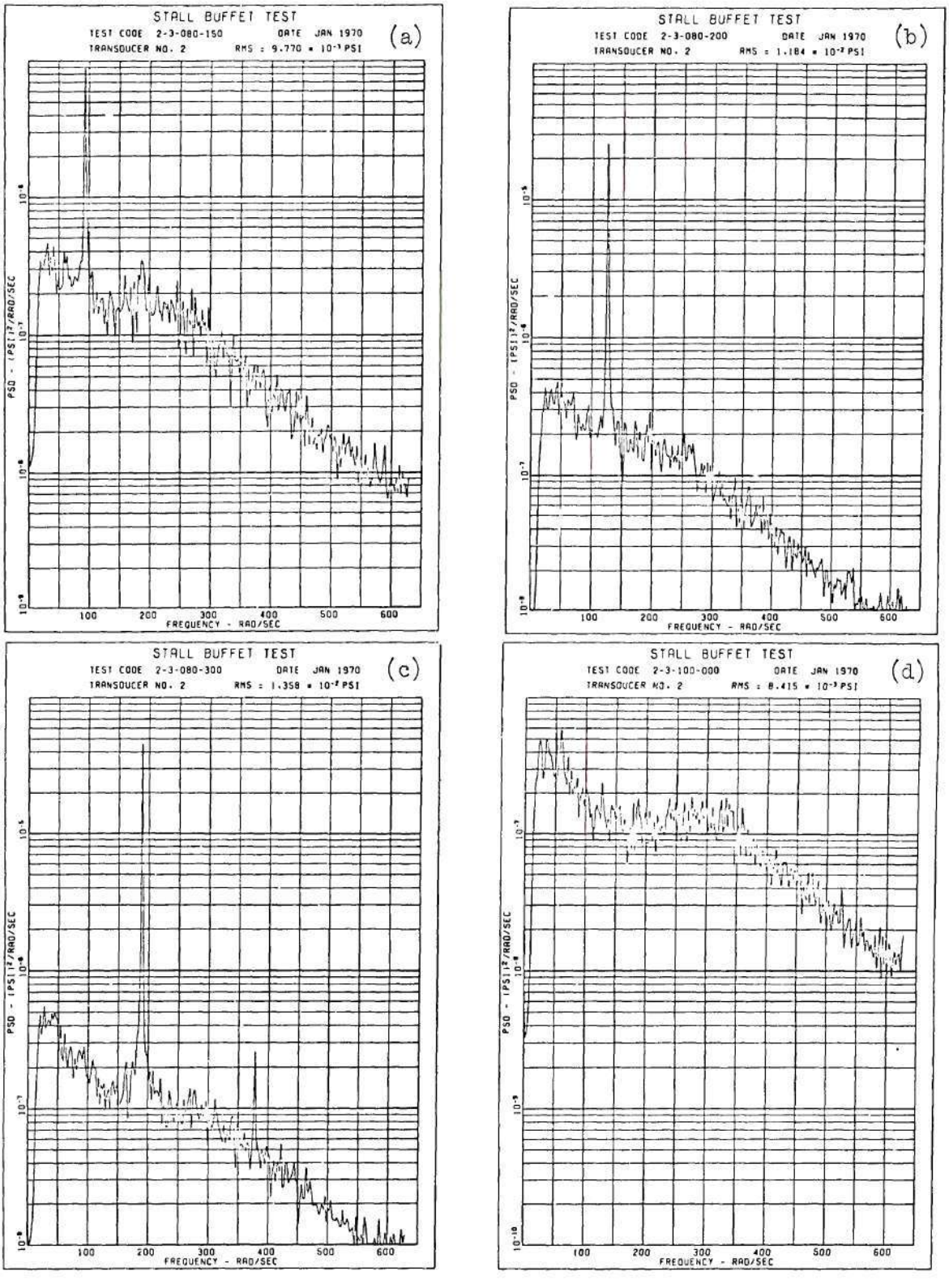

Figure 62. Additional Test Power Spectra,

$\alpha_o = 17.5°$, $U_\infty = 80$ fps, 100 fps

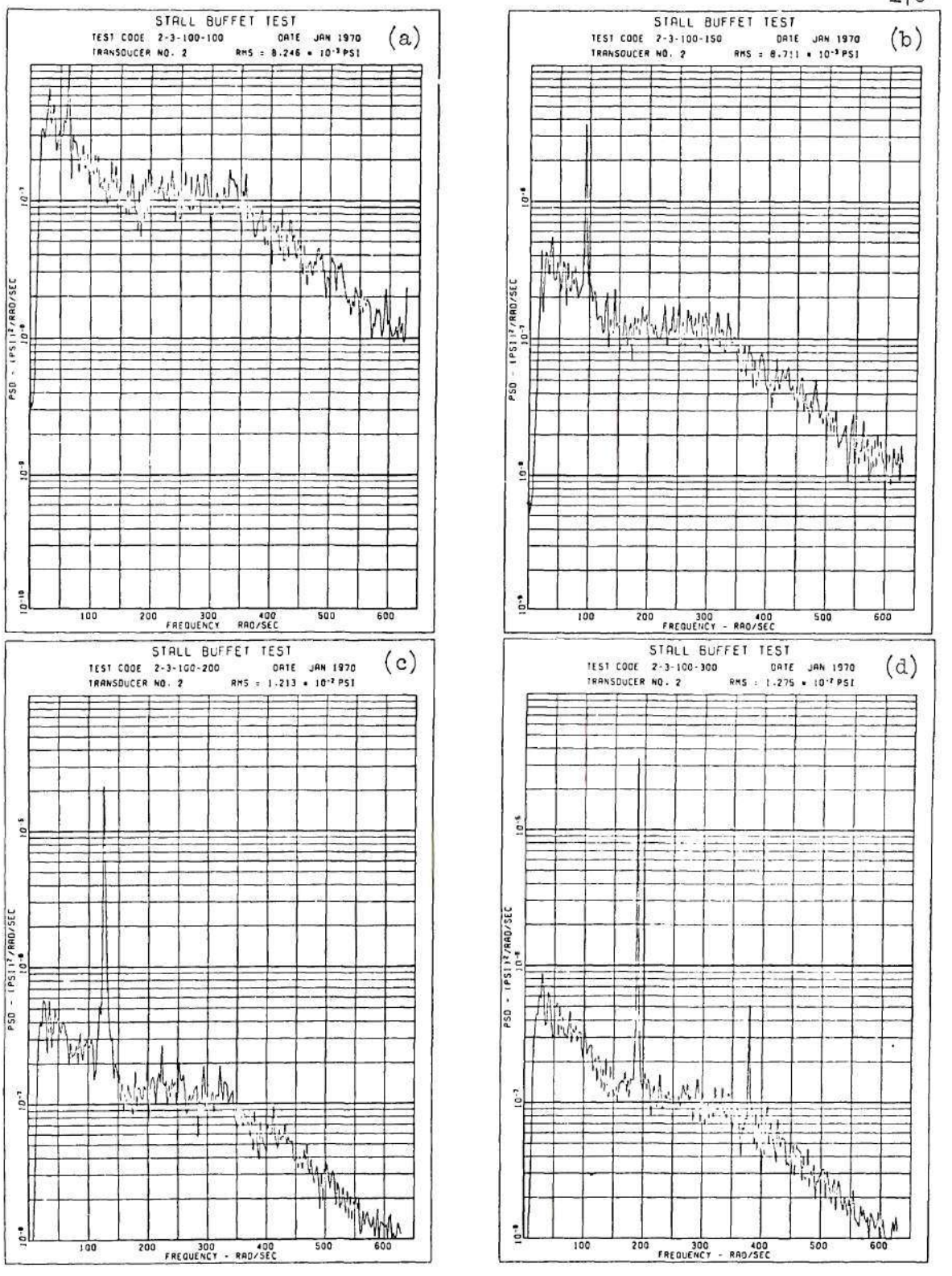

Figure 63. Additional Test Power Spectra,
$\alpha_o = 17.5°$, $U_\infty = 100$ fps

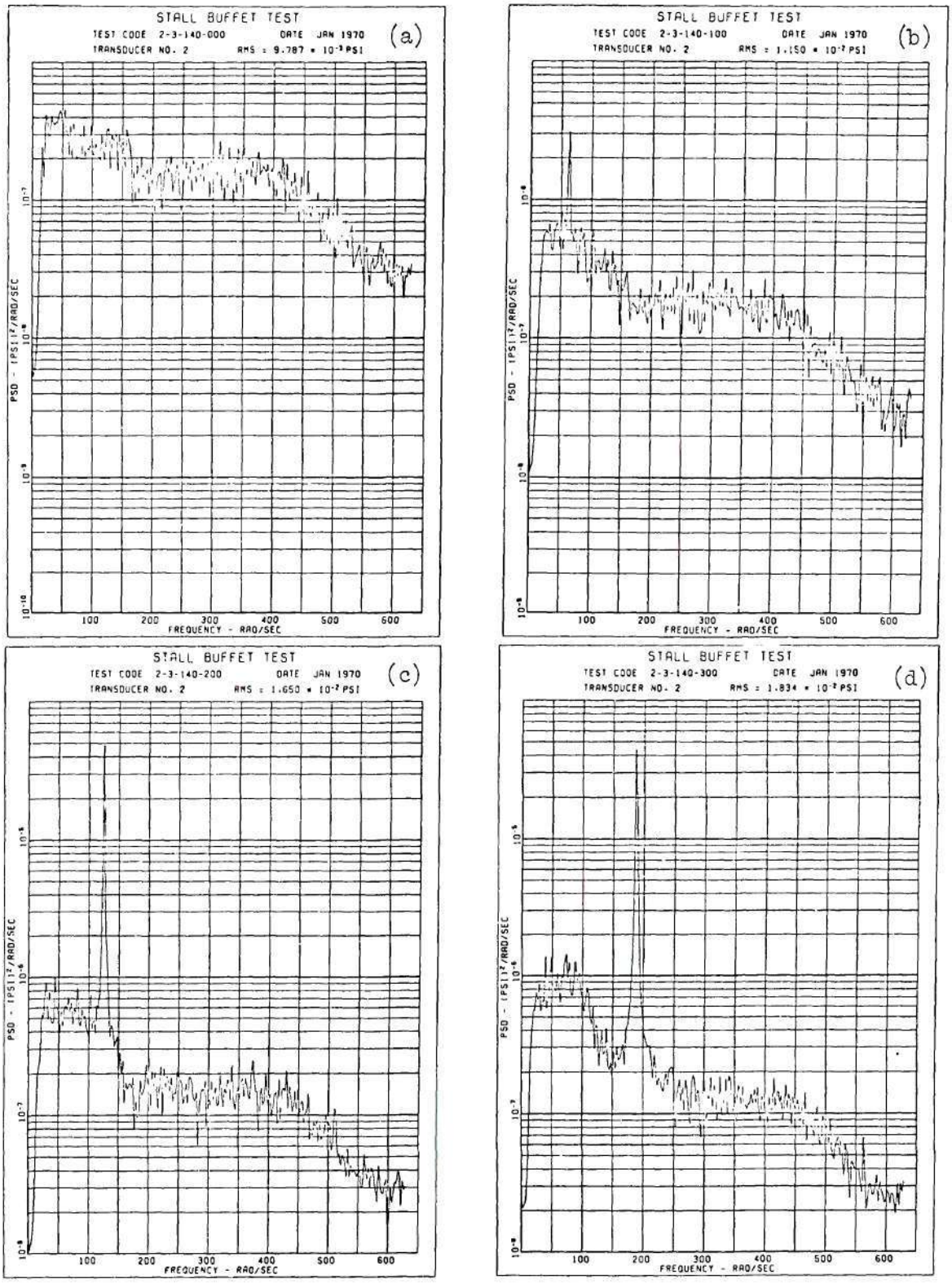

Figure 64. Additional Test Power Spectra,
$\alpha_o = 17.5°$, $U_\infty = 140$ fps

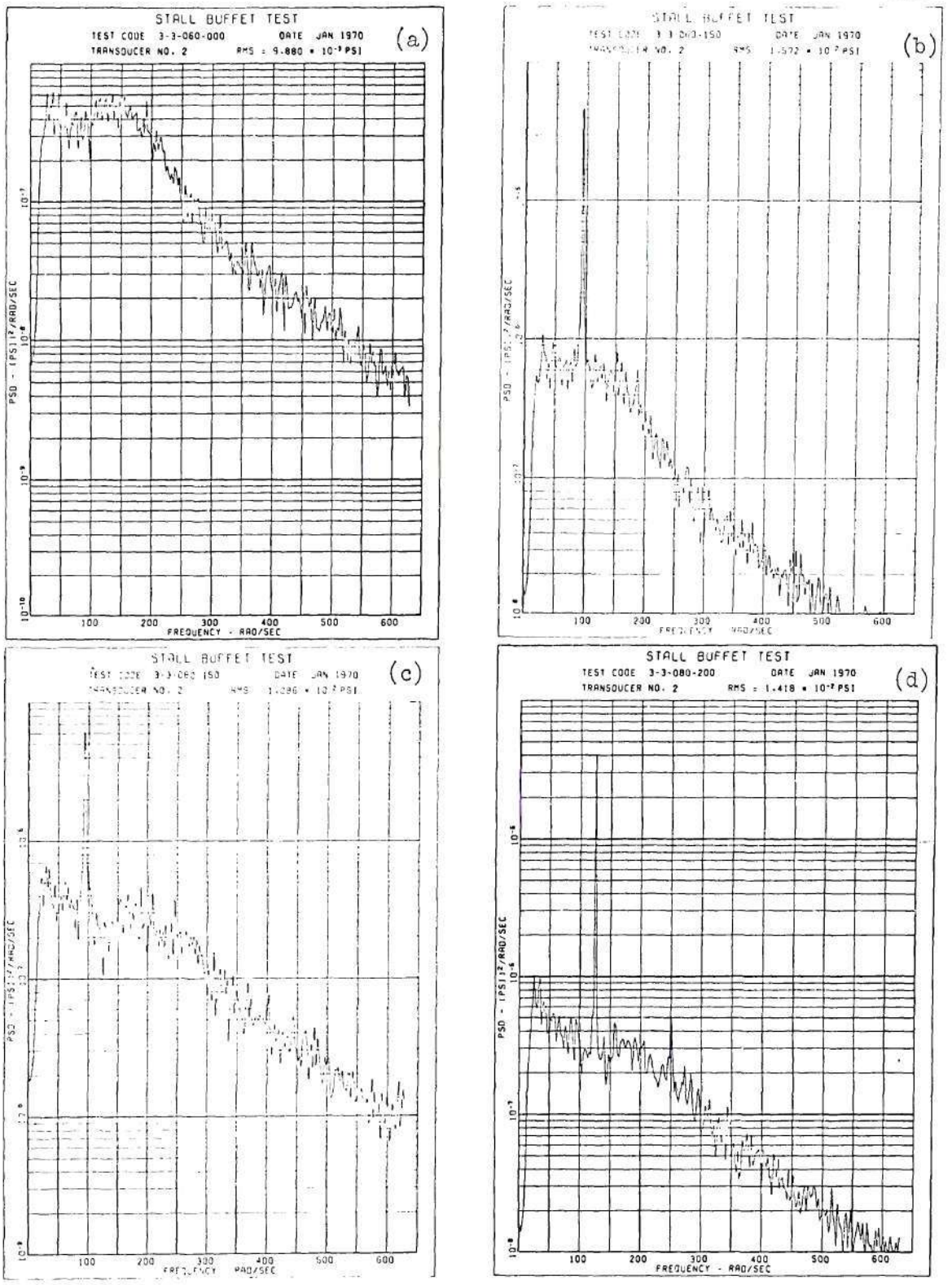

Figure 65. Additional Test Power Spectra,

$\alpha_o = 20.°$, U_∞ = 60 fps, 80 fps

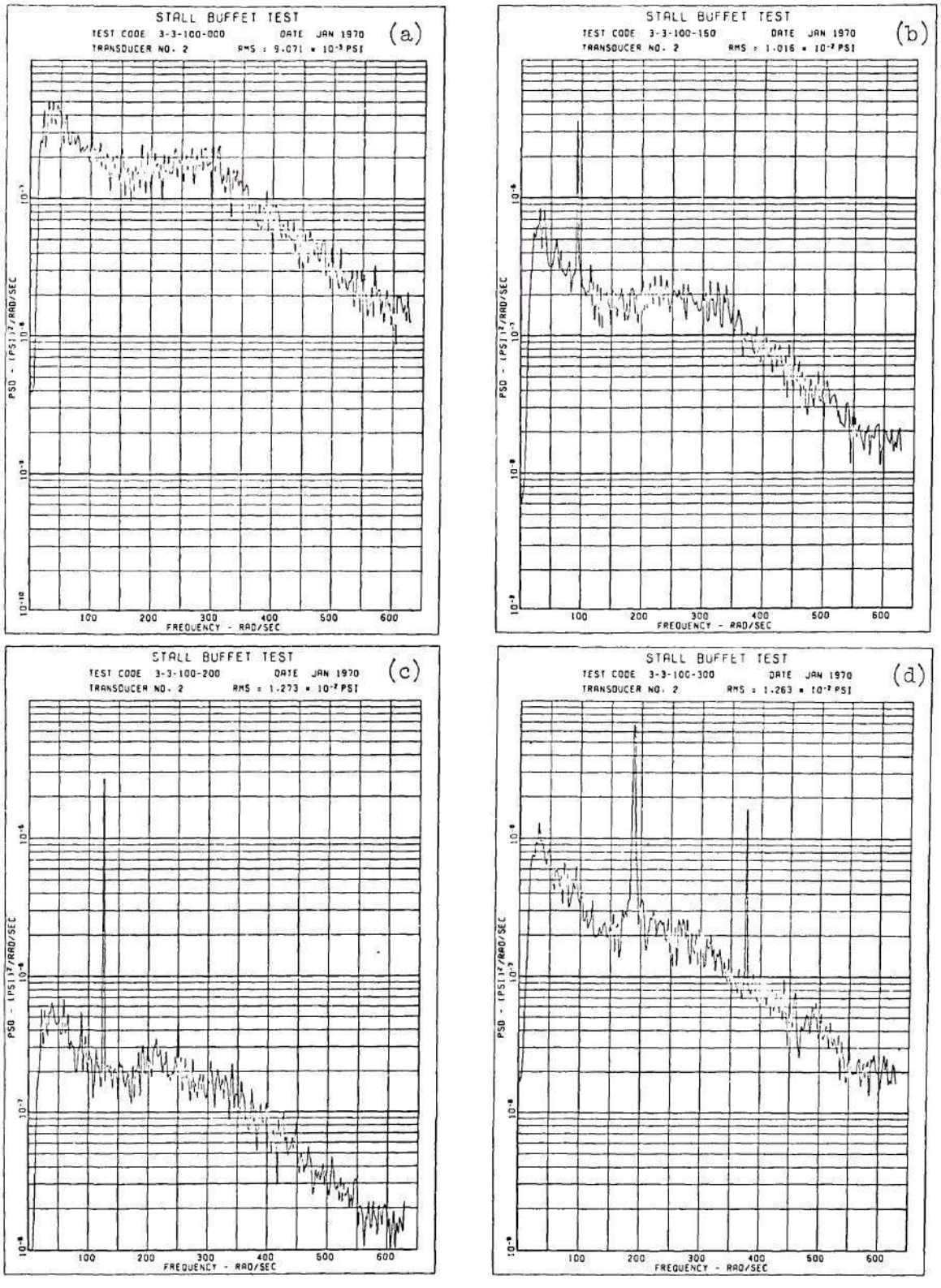

Figure 66. Additional Test Power Spectra,
$\alpha_o = 20.°$, $U_\infty = 140$ fps

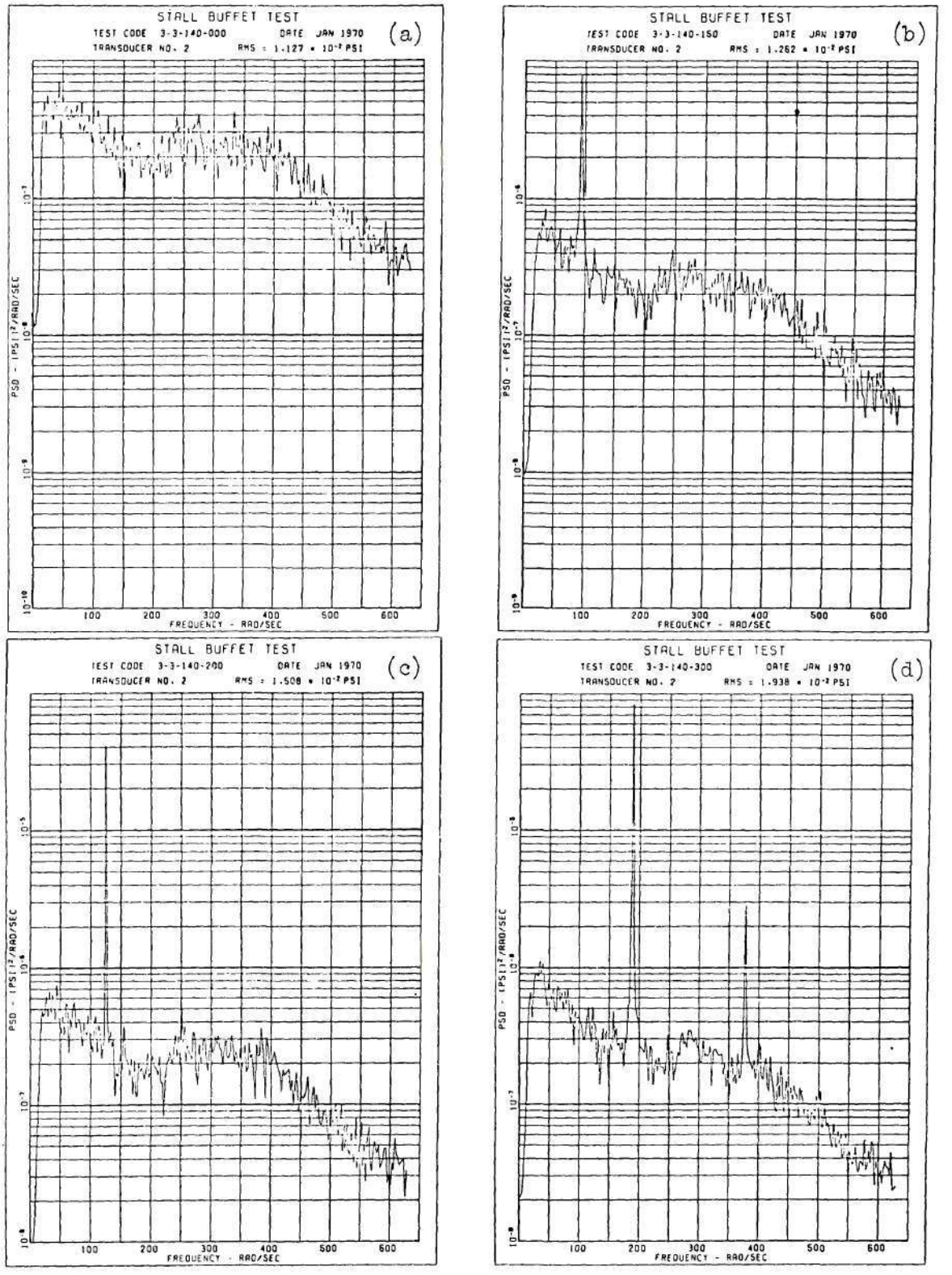

Figure 67. Additional Test Power Spectra,
$\alpha_o = 20.^\circ$, $U_\infty = 140$ fps

APPENDIX D

ANALOG COMPUTER SIMULATION OF A VORTEX WAKE

To simulate the time history of pressure due to the passage of a vortex array, Equation (80) of the text,

$$\frac{\Delta p(t)}{\rho\left(\frac{\Gamma}{2a}\right)^2} = \left(\frac{U_v}{\Gamma/2a}\right)\left(\frac{u}{\Gamma/2a}\right) + \frac{1}{2}\left[\left(\frac{u}{\Gamma/2a}\right)^2 + \left(\frac{v}{\Gamma/2a}\right)^2\right] \qquad (148)$$

was solved using an analog computer. For this purpose an EAI, Model TR-48 computer in the School of Aerospace Engineering was used. The functions $u/\Gamma/2a$ and $v/\Gamma/2a$ are functions of the transverse coordinate y, and time, as shown in Equations (76) and (77). The simulation requires the generation of $\sin\omega t$ and $\cos\omega t$, at some convenient time scale; scaling for each value of y, and the use of several electronic multipliers, to generate the scaled pressure.

The scaling is accomplished as follows. Let

$$\frac{u}{\Gamma/2a} = K_1 \frac{1}{1 + K_3 \cos\omega t} - K_2 \frac{1}{1 - K_4 \cos\omega t} \qquad (149)$$

for $y > \frac{b}{2}$, and

$$\frac{u}{\Gamma/2a} = K_1 \frac{1}{1 + K_3 \cos\omega t} + K_2' \frac{1}{1 - K_4 \cos\omega t} \qquad (150)$$

for $0 \leq y < b/2$, where,

$$\left.\begin{aligned} K_1 &= \tanh \frac{\pi}{a}(2y+b) \;, \quad K_2 = \tanh \frac{\pi}{a}(2y-b) \\ K_2' &= \tanh \frac{\pi}{a}(b-2y) \\ K_3 &= \frac{1}{\cosh \frac{\pi}{a}(2y+b)} \;, \quad K_4 = \frac{1}{\cosh \frac{\pi}{a}(2y-b)} \end{aligned}\right\} \tag{151}$$

and for $y \geq 0$,

$$\frac{v}{\Gamma/2a} = \left[\frac{K_3}{1 + K_3 \cos \omega t} + \frac{K_4}{1 - K_4 \cos \omega t} \right] \sin \omega t \tag{152}$$

Using unit scaling, and noting that all the above constants are less than unity and $K_3 \leq K_4$ for $y \geq 0$, there results

$$\frac{u}{\Gamma/2a} = \frac{K_1}{1-K_3} \frac{\left(\frac{1-K_3}{1+K_3}\right)}{\left(\frac{1}{1+K_3}\right)(1+K_3 \cos \omega t)} - \frac{K_2}{1-K_4} \frac{\left(\frac{1-K_4}{1+K_4}\right)}{\left(\frac{1}{1+K_4}\right)(1-K_4 \cos \omega t)} \tag{153}$$

$$\frac{v}{\Gamma/2a} = \frac{K_3}{1-K_3} \frac{\left(\frac{1-K_3}{1+K_3}\right) \sin \omega t}{\left(\frac{1}{1+K_3}\right)(1+K_3 \cos \omega t)} - \frac{K_4}{1-K_4} \frac{\left(\frac{1-K_4}{1+K_4}\right) \sin \omega t}{\left(\frac{1}{1+K_4}\right)(1-K_4 \cos \omega t)} \tag{154}$$

For $y < b/2$, the expressions are the same except that the leading coefficient in the second term of $u/\Gamma/2a$, $-(K_2/1-K_4)$ is replaced by $(K_2'/1-K_4)$. Completion of scaling depends on the value of $U_v/\Gamma/2a$.

Substituting various values of this parameter into Equation (148), the scaling is completed in each case by dividing through by a constant appropriate to give reasonable pot settings.

Four values of $2a\bar{U}_\infty/\Gamma$ were used, $2a\bar{U}_\infty/\Gamma$ = 10, 20, 30, 40, and computations were made for y = 0, b/4, 3b/4, and b. For all the compuations the spacing ratio b/a = .30 was used. Figure 68 is a mechanization for the problem. Table 4 presents the pot settings used for each condition.

Table 4. Analog Potentiometer Settings for Wake Pressure Time Histories

Pot No.	Formula	0	$b/4$	$3b/4$	b
00	1/	.100	.100	.100	.100
01	1/	.100	.100	.100	.100
02	I.C.	1.0	1.0	1.0	1.0
03	$K_3/1+K_3$	.4036	.3148	.1524	.1034
05	$1-K_4/1+K_4$	.1927	.0535	.0535	.1927
06	$1/1+K_3$	.5963	.6851	.8475	.8965
07	$K_2/1-K_4$	--	--	.486	1.00
08	$K_2/1-K_4$	.500	.488	--	--
15	$K_4/1+K_4$	.4036	.4732	.4732	.4036
17	$1-K_3/1+K_3$	.1927	.3703	.6950	.7931
18	$1/1+K_4$	.5963	.5267	.5267	.5963
20	$K_4/1-K_4$	.455	1.0	1.0	.910
21	$K_3/1-K_3$	.455	.096	.025	.0565
30	1/2k	.050	.500	.500	.100
31	1/2k	.050	.500	.500	.100
35	$K_1/1-K_3$	.500	.186	.226	.486
	(Above settings are fixed. Pot #32 varies with $2aU_v/\Gamma$ as listed below. All Pot settings are x 10.)				
32	$2aU_v/\Gamma$ = 10)	.0217	.1131	.113	.08694
	= 20)	.0435	.2262	.226	.1739
	= 30)	.0652	.3392	.339	.2607
	= 40)	.0870	.4524	.452	.3478

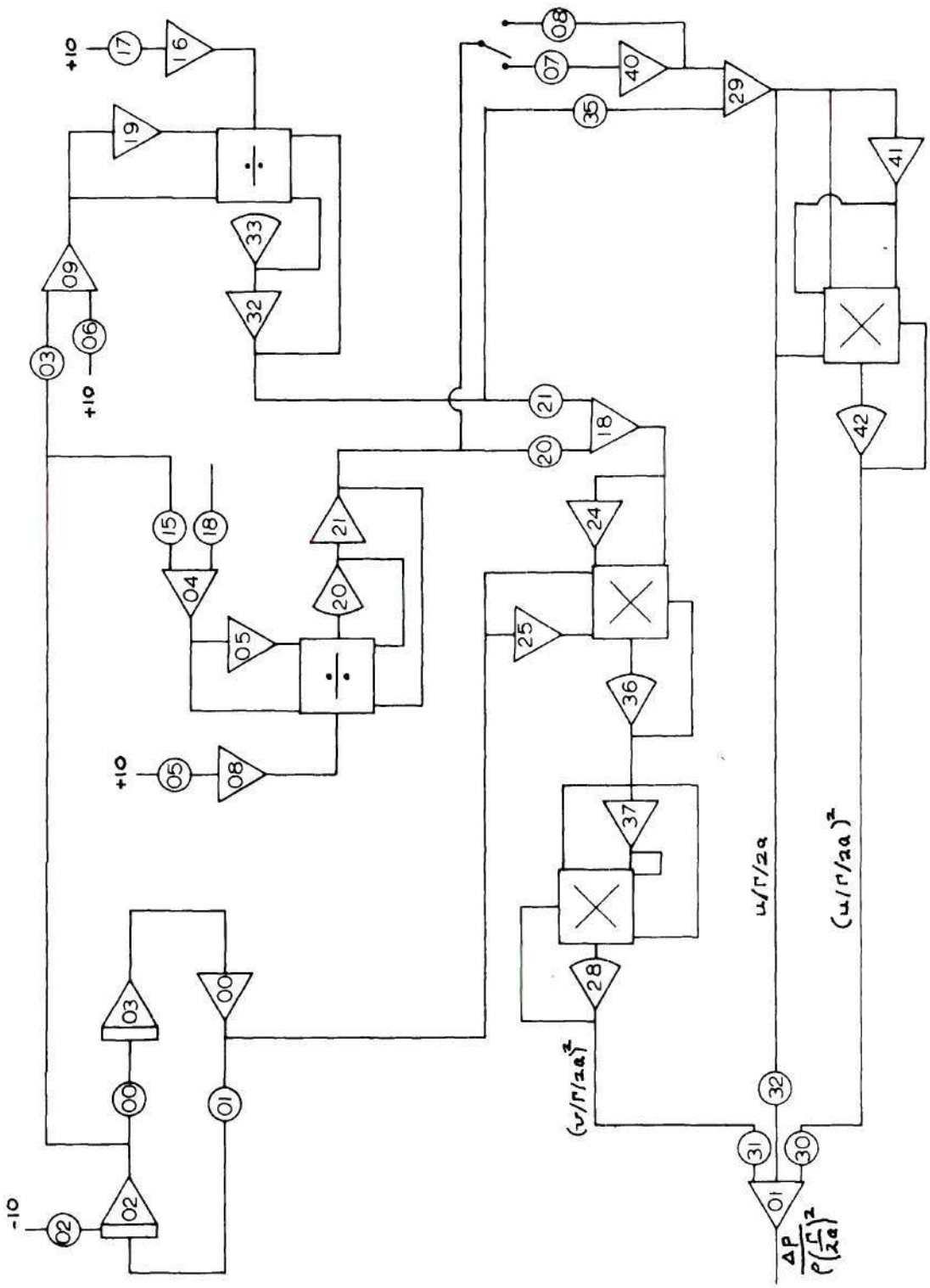

Figure 68. Schematic of Analog Simulation

LITERATURE CITED

1. Fung, Y. C., "The Theory of Aeroelasticity," John Wiley and Sons, Inc., New York, 1955.

2. Wittel, W. T., and Disney, T. E., "Relationship between Aircraft Design and Flight-Measured Loads," Journal of Aircraft, Vol. 5 No. 4, September-October 1967.

3. Halfman, Johnson, and Haley, "Evaluation of High Angle-of-Attack Aerodynamic-Derivative Data and Stall-Flutter Prediction Techniques," NACA TN 2533, November 1951.

4. Carta, Franklin O., Ham, Norman D., "An Analysis of the Stall Flutter Instability of Helicopter Rotor Blades," American Helicopter Society, 23rd Annual National Dorum Proceedings, No. 130, May 1967.

5. Liiva, J., Davenport, F. J., Gray, L., and Walton, I. C., "Two-Dimensional Tests of Airfoils Oscillating near Stall," Vol. 1, USAAVLABS Technical Report 68-13A, April 1968.

6. Ericsson, Lars Eric, "Comment on Airfoil Stall," Journal of Aircraft, Vol. 4, No. 5, September-October 1967.

7. Ericsson, Lars Eric, and Reding, J. P., "Unsteady Airfoil Stall," NASA CR-66787, July 1969.

8. George, M. B. T., "A Theoretical Approach to the Problem of Stall Flutter," Ph.D. Thesis, Cornell University, September 1953.

9. Ham, Norman D., "Aerodynamic Loading on a Helicopter Blade During Pitching Motion in the Presence of Stall," Sc.D. Thesis, Massachusetts Institute of Technology, January 1968.

10. Ujihara, B. H., "An Analytical Study of Separated Flow about a Circular Cylinder," North American Rockwell Corporation, Space Division, Report Number SD 68-332, NASA-4327, January 1966.

11. Sarpkaya, T., "An Analytical Study of Separated Flow about Circular Cylinders," Paper presented at ASME Fluids Engineering Conference, Philadelphia, Pennsylvania, May 6-9, 1968, Paper No. 68-Fe-15.

12. Moore, F. K., "Lift Hysteresis at Stall as an Unsteady Boundary Layer Phenomenon," NACA TN 3571, November 1955.

13. Fage, A., Johansen, F. C., "The Structure of Vortex Sheets," The Philosophical Magazine, Series 7, Volume 5, Number 28, February 1928.

14. Marris, A. W., "A Review on Vortex Streets, Periodic Wakes, and Induced Vibration Phenomena," Transactions of the ASME, Series D, Journal of Basic Engineering, 86, 1964.

15. Milne-Thompson, L. M., Theoretical Hydrodynamics, Second Edition, The Macmillan Company, New York, 1950.

16. Fung, Y. C., "Fluctuating Lift and Drag Acting on a Cylinder in a Flow at Supercritical Reynolds Number," Journal of the Aerospace Sciences, Volume 27, Number 11, November 1960.

17. Roshko, A., "On the Drag and Shedding Frequency of Two-Dimensional Bluff Bodies," NACA Technical Note 3169, July 1954.

18. Roshko, A., "Experiments on the Flow Past a Circular Cylinder at Very High Reynolds Number," Journal of Fluid Mechanics, Volume 10, May 1961.

19. Söhngen, H., Die Lösungen der Integralgleichung und deren Anwedung in der Tragflügeltheorie, Math. Z., Band 45, pp. 245-264, 1939.

20. Fage, A., Johansen, F. C., "On the Flow of Air Behind an Inclined Flat Plate of Infinite Span," Proceedings of the Royal Society of London, Series A, Volume 116, September 1927.

21. Tyler, E., "Vortex Formation Behind Obstacles of Various Sections," The Philosophical Magazine, Series 7, Volume 11, Number 72, April 1931.

22. Krzywoblocki, M. Z., "Investigation of the Wing-Wake Frequency with Application of the Strouhal Number," Journal of the Aeronautical Sciences, Volume 12, January 1945.

23. Jones, G. W., "Unsteady Lift Forces Generated by Vortex Shedding about a Large, Stationary, and Oscillating Cylinder at High Reynolds Numbers," Paper presented at ASME Fluids Engineering Conference, Philadelphia, Pennsylvania, May 6-9, 1968, Paper Number 68-Fe-36.

24. Milligan, R., Smiley, R., "Experimental Investigation of Aerodynamic Phenomena in the Wake of a Rapidly Stalled Wing," Final Report to Naval Air Systems Command under Contract N00019-68-C-0192, by Allied Research Associates, Inc., Concord, Massachusetts.

25. Inversin, A. R., "The Effect of Wing Leading and Trailing Edge Shed Vorticity on Tailplane Loading," S.M. Thesis, Massachusetts Institute of Technology, January 1968.

26. Liepmann, H. W., "On the Application of Statistical Concepts to the Buffeting Problem," Journal of the Aeronautical Sciences, Volume 19, Number 12, December 1952.

27. Hoerner, S. F., Fluid Dynamic Drag, Published by the author, 1965.

28. Cornish, J. J., III, Scruggs, R. M., "A Synthesis of the Lift and Drag Characteristics of a Flat Plate," Lockheed-Georgia Company Engineering Report Number 9419, June 1968.

29. Muskhelishvili, N. I., Singular Integral Equations, P. Noordhoff, N. V., Groningen, Holland, 1953.

30. Muskhelishvili, N. E., Some Basic Problems of the Mathematical Theory of Elasticity, P. Noordhoff, Groningen, Holland, 1953.

31. Cooley, J. W., Tukey, J. W., "An Algorithm for the Machine Calculation of Complex Fourier Series," Mathematical Computation, Volume 19, April 1965.

32. Bergland, G. D., "A Guided Tour of the Fast Fourier Transform," IEEE Spectrum, July 1969.

33. Blackman, R. B., Tukey, J. W., The Measurement of Power Spectra, Dover Publications, New York, 1958.

34. Goldstein, S. (Editor), Modern Developments in Fluid Dynamics, Volume II, Dover Publications, New York, 1965.

35. Bendat, J. S., Principles and Applications of Random Noise Theory, John Wiley & Sons, Inc., New York, 1958.

36. Carleman, T., "Sur la resolution de certaines equations integrales," Arkiv för Matem. och Physik, 16, No. 26, 1922.

37. Toebes, G. H., "Fluidelastic Features of Flow Around Cylinders," Paper No. 37, Proceedings of the International Research Seminar, National Research Council, Ottawa, Canada, Sept. 11-15, 1967, University of Toronto Press.

38. Titchmarsh, E. C., The Theory of Functions, Second Edition, Oxford University Press, London, 1939.

VITA

Roy Mac Scruggs was born April 2, 1936, the son of John Leon and Winifred Scruggs. After attending elementary and secondary school in Brooks County, Georgia, he was graduated from Morven High School in June, 1954. He entered the Georgia Institute of Technology in the Fall of that year and in September, 1958, completed requirements for the degree Bachelor of Aeronautical Engineering.

In October, 1958, he accepted a position with the Lockheed-Georgia Company. In 1964 he completed requirements for the degree Master of Science in Engineering Mechanics at the Georgia Institute of Technology, his thesis received the M. A. Ferst Award of the Society of the Sigma Xi. In 1964 he accepted a supervisory position with the Space Division of the Chrysler Corporation, returning to the Lockheed-Georgia Company in 1965 in a research scientist capacity.